TIAGO LUÍS SERPA

IN SITU AND SATELLITE CHARACTERISATION OF MEDDIES' STRUCTURES IN OPEN OCEAN NE ATLANTIC: NA-VICE CRUISE (2012), AZORES TO ICELAND

Faculdade de Ciência e Tecnologia

2023

TIAGO LUÍS SERPA

IN SITU AND SATELLITE CHARACTERISATION OF MEDDIES' STRUCTURES IN OPEN OCEAN NE ATLANTIC: NA-VICE CRUISE (2012), AZORES TO ICELAND

Master's degree in Marine and Coastal Systems

Dissertation

Work performed under the supervision of:

Prof. Dr. Ana Maria de Pinho Ferreira da Silva Fernandes Martins, DOP-FCT, University of Azores

Prof. Dr. Paulo José Relvas de Almeida, CCMAR, University of Algarve

Faculdade de Ciência e Tecnologia

2023

IN SITU AND SATELLITE CHARACTERISATION OF MEDDIES' STRUCTURES IN OPEN OCEAN NE ATLANTIC: NA-VICE CRUISE (2012), AZORES TO ICELAND

Declaração de autoria de trabalho

Declaro ser o autor deste trabalho, que é original e inédito. Autores e trabalhos consultados estão devidamente citados no texto e constam da listagem de referências incluída.

Declaration of authorship of work

I declare to be the author of this work, which is original and unpublished. Authors and works consulted are duly cited in the text and included in the reference list.

Signature

_____

(Tiago Luís Serpa)

Acknowledgements

I would like to start by thanking my advisors Prof. Dr. Ana Martins and Prof. Dr. Paulo Relvas for their support and wisdom especially throughout this last year and for the opportunities they gave me which helped me integrate into the scientific community.

To Prof. Dr. Paulo Relvas, who is also the Director of the master program in Marine and Coastal Systems, goes my appreciation for his availability and concern for his students. This appreciation is extended to all the teachers of the master's for their time, patience, and availability whenever any doubt arose.

A special thanks to the Oceanography team from the Department of Oceanography and Fisheries (DOP) at the Faculty of Sciences and Technology of the University of Azores, for making me feel welcome and for all their support and guidance throughout this process, specifically Prof. Dr. Ana Martins, Dr. Clara Loureiro, Dr. Catharina Pieper, Master students Marta Gomes and Cassandra Pacheco and the honorary member of this team PhD student Ana Pabon.

To Dr. Frederico Ienna, Prof. Dr. Kay Bidle, Prof. Dr Joaquim Dias, and Prof. Dr. Eric Firing, thank you for your help and availability to correspond with me.

In particular, I would like to thank Dr. Kay Bidle (Rutgers University, USA), principal investigator of the international project: "NA-VICE: Lipid lubrication of oceanic carbon and sulfur biogeochemistry via a host-virus chemical arms race" (Ref: OCE-1061883, funded by the NSF), for allowing me to use oceanographic data (CTD and ADCP) obtained during the R/V Knorr cruise KN207-03 that took place from Azores to Iceland during the summer of 2012.

To informatics engineer Miguel Figueiredo, thank you for your support with the Canopus images used in this research study and for providing a description of the Canopus satellite processing software.

I would also like to thank the financial support provided to me by the MAGAL Constellation - Defining the pillar of a future constellation for monitoring the Ocean and Climate Change project (Ref: ACORES-01-0145-FEDER-000129) through the primary beneficiary entity *Fundação Gaspar Frutuoso* (UAc).

A special thanks also goes to the logistics and staff from both Algarve and Azores Universities.

To all my friends in the Azores, Portugal mainland, and internationally, thank you for being part of my life and for contributing to the person I am today.

To my girlfriend Joana, thank you for believing in me never doubting that I could do this, and for suggesting that I came to DOP to look for this thesis.

To my parents, Paulo and Graça, thank you for your support (financial and emotional), for never letting me lack anything, for all your teachings in life-related subjects, and for allowing me to pursue my academic dreams these last five years. To my sister Tatiana and all my family, thank you for being there and for checking up on me.

Lastly, I thank the jury for taking the time to read and access this thesis, which represents another closing chapter of my life.

Abstract

A meddy was found at 41.3º N 27.1º W during the R/V Knorr cruise KN207-03 that took place from the Azores to Iceland in the summer of 2012 within the framework of the international project NA-VICE. The meddy's main physical properties and characteristics were identified using *in situ* data (CTD and ADCP) and salinity and temperature anomalies of 0.24 and 2.18ºC, respectively, were found as well as azimuthal velocities up to 0.35 m s^{-1}. These values were compared with criteria described by previous authors to ensure that this structure, which was further north than most observations, could be classified as a meddy. Meanwhile, a cyclonic eddy with characteristics from Mediterranean Water (MW) was also found to interact with the meddy, and their relationship was discussed. Afterwards, the meddy's surface expression was analysed using altimetry data combined with an eddy detection algorithm, and it was found that its Sea Level Anomaly (SLA) was 15 cm, and it presented a 100 km radius. This data was used to track the meddy's path, giving a general idea of the generation and dissipation dates and locations, leading to the hypothesis that the locations previously identified by other authors do not encompass all the possible meddy generation sites. A new method was tested using satellite Ocean Colour (OC) images to identify meddies surface expression. Despite the previously known Sea Surface Temperature (SST) surface expression, the results show that other valuable parameters such as Chlorophyll-*a* (Chlor-a), kd_490, Particulate Organic Carbon (POC), and Particulate Inorganic Carbon (PIC) are equally important, emphasising the vital role of the meddies in the mixing and transport of biogeochemical properties in the ocean and how this has been underestimated.

Key words

Meddies, Eddies, Mediterranean Water, Remote Sensing, Altimetry, Ocean Colour

Resumo

Um *meddy* foi encontrado a 41.3º N 27.1º W durante uma campanha abordo do R/V Knorr dos Açores até à Islândia no verão de 2012 no âmbito do projeto internacional NA-VICE. As principais propriedades físicas e características do *meddy* foram identificadas através de dados *in situ* (CTD e ADCP) e anomalias de salinidade e temperatura de 0.24 e 2.18ºC, respetivamente, foram encontradas, bem como velocidades azimutais até 0.35 m s^{-1}. Estes valores foram comparados com critérios descritos por autores anteriores para certificar que esta estrutura, que foi encontrada mais a norte do que a maioria das observações, podia ser classificada como um *meddy*. Entretanto, um *eddy* ciclónico com características da Água do Mediterrâneo (MW) foi encontrado a interagir com o *meddy* e a sua relação foi discutida. Depois, a expressão de superfície do *meddy* foi analisada utilizando dados de altimetria em combinação com um algoritmo de deteção de *eddies* e foi descoberto que a sua anomalia do nível do mar (SLA) foi de 15 cm e tinha um raio de 100 km. Estes dados foram utilizados para acompanhar o percurso do *meddy*, dando uma ideia geral das suas datas e locais de geração e dissipação, o que levou à hipótese de que os locais identificados até à data, por autores anteriores, não englobam todos os possíveis locais de geração de *meddies*. Um novo método foi testado utilizando imagens de satélite de cor do oceano (OC) para a identificar a expressão de superfície de *meddies*. Apesar da já conhecida expressão de superfície da temperatura de superfície do mar (SST), os resultados mostram que outros parâmetros uteis como a Clorofila-*a* (Chlor-a), kd_490, Carbono Orgânico Particulado (POC) e Carbono Inorgânico Particulado (PIC) são igualmente importantes, enfatizando o papel fundamental dos *meddies* na mistura e transporte de propriedades biogeoquímicas no oceano e como este tem sido subestimado.

Palavras-chave

Meddies, *Eddies*, Água do Mediterrâneo, Deteção Remota, Altimetria, Cor do Oceano

Table of contents

Figure Index

Table Index

Equation Index

Appendix Index

List of Acronyms and Abbreviations

ADCP	Acoustic Doppler Current Profiler
AzC	Azores Current
BB	BroadBand
CDOM	Coloured Dissolved Organic Matter
Chlor-a	Chlorophy-*a* (C*lorofila-a*)
CODAS	Common Ocean Data Access System
CT	Conservative Temperature
CTD	Conductivity Temperature Depth
DO	Dissolved Oxygen
DSOW	Denmark Strait Overflow Water
ENACW	Eastern North Atlantic Central Water
EOS-80	Equation of State of Seawater – 1980
GSW	Gibbs-SeaWater
IOC	International Oceanographic Commission
IR	Infrared
ISOW	Iceland-Scotland Overflow Water
Kd-490	Attenuation Coefficient at 490 nm
lNADW	Lower North Atlantic Deep Water
LSW	Labrador Sea Water
MAR	Mid-Atlantic Ridge
MOW	Mediterranean Outflow
MW	Mediterranean Water (*Água do Mediterrâneo*)
NASA	National Aeronautics and Space Administration

NA-VICE	North Atlantic Virus Infection of Coccolithophores Expedition
NB	NarrowBand
NE	Northeast
NEABW	Northeast Atlantic Bottom Water
OC	Ocean Colour (*Cor do Oceano*)
ODV	Ocean Data View
OS-75	Ocean Surveyor – 75 kHz
PAR	Photosynthetically Active Radiation
PIC	Particulate Inorganic Carbon (*Carbono Inorgânico Particulado*)
POC	Particulate Organic Carbon (*Carbono Orgânico Particulado*)
SA	Absolute Salinity
SAIW	Subarctic Intermediate Water
SLA	Sea Level Anomaly (*Anomalia do Nível do Mar*)
SP	Practical Salinity
SSH	Sea Surface Height
SST	Sea Surface Temperature (*Temperatura da Superfície do Mar*)
SWT	Source Water Type
TEOS-10	Thermodynamic Equation of Seawater – 2010
UHDAS	University of Hawaii Data Acquisition System
uNADW	Upper North Atlantic Deep Water
WH-300	Workhorse – 300kHz
WM	Water Mass
WNACW	Western North Atlantic Central Water

1. Introduction

1.2. Motivation for the topic

As climatic variability becomes a more significant topic, it is essential to emphasise that it is not exclusive to the atmosphere and upper ocean. In the subsurface layers, some features promote changes in ocean properties and their distribution and abundance changes with time (Klemas & Yan, 2014; Frazão *et al*., 2021). This could consequentially impact processes regulating the ocean, i.e., large-scale processes such as thermohaline circulation. There is already evidence of an increasing warming trend of temperature below 700 m depth, while the trend in the upper 300 m has entered a hiatus (Balmaseda *et al*., 2013).

One example of a unique feature of the North Atlantic's intermediate depths is the Mediterranean salt tongue (Käse & Zenk, 1987). This warm and saline water, neutrally buoyant at about 1000 m depth, plays an important climatic role in transporting heat and salt into the Northeast Atlantic (Armi & Zenk, 1984; Armi *et al*., 1989; Richardson *et al*., 1989). A large fraction of this transfer is attributed to the decay and destruction of Mediterranean Water Eddies (Armi *et al*., 1989; Richardson *et al*., 2000), whose contribution may be responsible for over 50% of the Mediterranean Water's (MW) salt flux (Arhan *et al*., 1994).

The study of meddies (Mediterranean Water Eddies) has been going on since the 70's, with increasingly growing interest. While initially discovered through hydrographic surveys, several breakthroughs from using floats and mooring stations to using satellite products (mostly altimetry and Sea Surface Temperature (SST)) have contributed to the characterization of these features' physicochemical properties. Its most frequent formation sites and trajectories have been documented, and the continuous development of new tracking methods has provided a better input of the abundance of meddies in the North Atlantic (an important value for computing the actual contribution of the Mediterranean Outflow (MOW)). However, these new methods also bring to light new data about meddies' spatial distribution and characteristics that have not been duly explored, and still little is known about the biogeochemical characteristics of meddies and their impact on the environment.

During the summer of 2012, the North Atlantic Virus Infection of Coccolithophores Expedition (cruise KN207-03 from Azores to Iceland) took place aboard the R/V Knorr under the framework of the international project NA-VICE: Lipid lubrication of oceanic carbon and sulphur biogeochemistry via a host-virus chemical arms race" (Ref. OCE-1061883, funded by the NSF). Although the main purpose of the cruise was to locate a chemical host-virus in the

North Atlantic, the data collected presented the opportunity to describe a meddy detected at 41.3º N 27.1º W coupled with a deep cyclonic eddy of positive salinity and temperature anomalies found at 42.9º N 27.2º W.

1.3. Objectives

The main goal of this study is to describe the physico-chemical characteristics of a meddy found north of the Azores Archipelago during the NA-VICE cruise. Its surface signature will be analysed using altimetry and SST and tracked according to previous methodology. Afterwards, the meddy will be observed using remote sensing Ocean Colour (OC) data to perceive whether this signature presents biogeochemical characteristics. Some questions posed are: Are meddies exclusively formed in the Iberian shelf? Is it possible to observe their surface signature through OC?

2. State of the Art

2.1. General characterization of the NE Atlantic

2.1.1. Geographic features

The North Atlantic is divided into two halves (eastern and western) by the Mid-Atlantic Ridge (MAR), a bathymetric feature that separates the North American plate from the Eurasian and Nubia plates. In the location where these three plates meet lies the Azores Archipelago and is called the Azores Triple Junction (Marques *et al*., 2013). Besides the MAR, the Northeast Atlantic is defined by several features such as islands, capes, seamounts, and canyons, and its eastern boundary is defined by the coastline of several European and non-European countries (Figure 2.1). The North African coast is separated from the Iberian Peninsula by the Gibraltar Strait, which connects the Mediterranean to the Atlantic. These two coasts form the Gulf of Cadiz. West-southwest of the Gulf of Cadiz there is a high density of seamounts (Horseshoe seamounts) located in the plate boundary between the Eurasian and Nubian plates (Wienberg *et al*., 2013). Along the Iberian Peninsula coast, there are various capes and canyons (i.e.: Cape São Vincente, Cape Sines, Cape Espichel, Estremadura Promontory, Cape Carvoeiro, Cape Finisterre, Cape Ortegal) that pose as obstacles for boundary currents. North of the Iberian Peninsula is the Bay of Biscay, surrounded by Spain's northern coast and France's southwestern coast. Some features associated with the Bay of Biscay are the Charcot and Biscay seamounts

(Paillet et al., 1999), located on its open side, and the Goban Spur (De Graciansky & Poag, 1985), located to the north of these, in the continental slope.

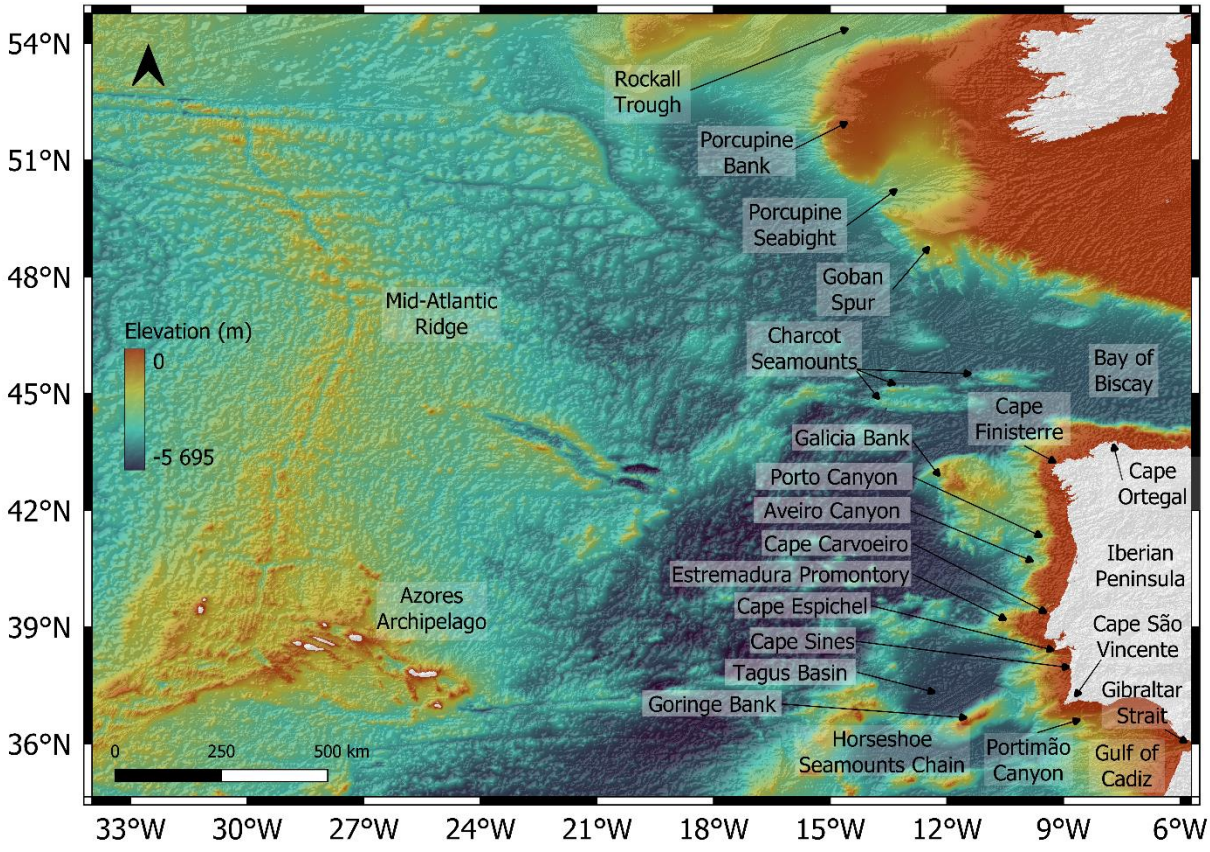

Figure 2.1 – Bathymetry map of the NE Atlantic, showing the main geographic features of the study area. Data was obtained from the IGPP Global Earth Relief, with a resolution of 30 arc second (Tozer *et al*., 2019).

2.1.2. Water Masses and Source Water Types

According to the definitions established by Tomczak (1999), a Water Mass (WM) is a body of water with a common formation history, which originated in a particular part of the ocean and like air masses, they are physical entities that occupy a finite volume in the ocean which can be quantified. A WM's properties measured in *n*-dimensional parameter space (mathematical construct of a combination of parameters i.e.: temperature, salinity, oxygen, nutrients) define its water type (Tomczak, 1999). A water type that corresponds closely to the properties of a WM in its source region is called a Source Water Type (SWT) (Tomczak, 1999).

In terms of vertical distribution, the Atlantic Ocean can be divided into four isopycnal layers separated by surfaces of neutral density (γ) (Liu & Tanhua, 2021). The WMs that can be found in the North Atlantic are described in Table 2.1, grouped in their respective layers. The upper layer has the lowest neutral density and is located below the thermocline, in the upper 500 – 1000 m depth with $\gamma < 27.10$ kg m^{-3}. The intermediate layer is located between 1000 – 2000 m depth, approximately, with $27.10 < \gamma < 27.90$ kg m^{-3}. The deep and overflow layer is located between approximately 2000 – 4000 m depth with $27.90 < \gamma < 28.10$ kg m^{-3}. Lastly, the bottom layer is located below 4000 m depth approximately with $\gamma > 28.10$ kg m^{-3}.

Table 2.1.: Summary of the SWT located in the North Atlantic Basin distributed in four layers, with their location defined by latitude, longitude, and depth. Adapted from Liu & Tanhua (2021). Meaning of abbreviations: ENACW – East North Atlantic Central Water; WNACW – West North Atlantic Central Water; MW – Mediterranean Water; SAIW – Sub-Artic Intermediate Water; uNADW – upper North Atlantic Deep Water; lNADW – lower North Atlantic Deep Water; LSW – Labrador Sea Water; ISOW – Iceland-Scotland Overflow Water; DSOW – Denmark Strait Overflow Water; NEABW – Northeast Atlantic Bottom Water.

Layer	SWT	Longitude (º W)	Latitude (º N)	Pressure (dbar)
Upper	ENACW	20 – 35	39 – 48	100 – 500
	WNACW	50 – 70	24 – 37	100 – 500
Intermediate	MW	6 – 24	33 – 48	>300
	SAIW	35 – 55	50 – 60	100 – 500
Deep and overflow	uNADW	32 – 50	40 – 50	1200 – 2000
	lNADW	32 – 50	40 – 50	2000 – 3000
	LSW	24 – 60	48 – 66	500 – 2000
	ISOW	0 – 45	50 – 66	1500 – 3000
	DSOW	19 – 46	55 – 66	>1500
Bottom	NEABW	10 – 45	0 – 30	>4000

This division of the water column in layers is related to the large-scale overturning circulation, also known as the thermohaline circulation (Pickard & Emery, 1982). In recent years, a new definition arose to refer to this circulation, namely Meridional Overturning Circulation, to account for the zonally integrated volume flux (Lozier *et al*., 2022). The Atlantic Meridional Overturning Circulation carries warm and salty water poleward in the upper layers, where due

to the interaction with atmospheric heat fluxes and freshwater inputs, it transforms into colder, fresher, and denser waters that sink to deeper layers and travels equatorward (Lozier et al., 2022). The term “Overflow Water” is attributed to these dense Nordic Sea waters that flow equatorward into the North Atlantic, along several pathways (not restricted to boundary currents) (Lozier et al., 2022).

2.1.3. Upper Ocean and Atmospheric Circulation

In the ocean-atmosphere interface, the North Atlantic is composed of four main currents that result in a clockwise gyre, commonly known as North Atlantic Subtropical Gyre (Pires, 2013). This gyre is thought to start with the westward-flowing North Equatorial Current, driven by the northeast trade winds, then it turns northeast along the eastern North American coast as the Gulf Stream. From here, the flow turns east and north as the North Atlantic Drift, contributing to the circulation of the Artic Seas, and afterwards heads south as a slow and diffuse flow, making the connection with the North Equatorial Current and completing the gyre (Pickard & Emery, 1982). Due to its characteristics, it is difficult to distinguish specific currents in this southward flow, but the Canary Current flowing to the south off the North African coast is recognized (Pickard & Emery, 1982).

The synoptic wind regime is dictated by the relative position of the Azores’ anticyclonic high pressure (Azores High) and Iceland's cyclonic low pressure (Icelandic Low). The Azores High relocates from a northern position off the Iberian Peninsula to a southern position in front of Morocco, while the Icelandic Low intensifies allowing the passage of eastward low-pressure systems (Pires, 2013). Wind-induced upwelling-favourable conditions occur during summertime, along the western coasts of Europe. when the Azores High is in its northern position,

2.2. Mediterranean Outflow and Undercurrent

The MW and the NACW connect in the Gibraltar Strait, where the first exits the Mediterranean through the bottom while the latter enters through the surface. This two-way path is due to the difference in density between these WMs, where the MW is much denser due to excess evaporation over precipitation and runoff (Ochoa & Bray, 1991). After exiting through the Gibraltar Strait, the MOW sinks along the slope, while starting to entrain with NACW until a

neutrally buoyant depth at about 1000 m, transforming into MOW (De Pascual-Collar et al., 2019). As it spreads through the Gulf of Cadiz, the MOW reaches an equilibrium and splits into two branches due to the interaction with the bottom topography and mixing, an upper branch located between 500 – 800 m depth and a lower branch between 800 – 1200 m (Gasser et al., 2017). Ambar et al. (2002, 2008), described these branches as cores of maximum temperature and salinity and besides the upper and lower cores at 800 m and 1200 m, respectively, they described a third shallow core at less than 600 m.

After passing Cape São Vincente, the Mediterranean Undercurrent (MUC) turns northward, travelling along the western margin of the Iberian Peninsula, getting trapped and turning anticyclonically at the Tagus Basin (Daniault *et al*., 1994). From here, it assumes two main pathways: poleward along the western European continental slope entering the Bay of Biscay and continuing northward until Porcupine Bank and Rockall Trough at 53º N, and westward towards the central Atlantic (De Pascual-Collar *et al*., 2019). Besides these two main paths, this reservoir of MOW also travels south and southwest being transported by MW lenses (Armi & Zenk, 1984).

Salinity and temperature values for the MOW at the Gulf of Cadiz vary from 37.1 to 37.4 g kg^{-1} (Absolute Salinity (SA)) and 13.7 to 13.6º C between the upper and lower branches, respectively (Gasser et al., 2017). As it mixes with ambient waters, by the time it reaches the Bay of Biscay, its presence is observed in potential temperature with values at 800 m depth being higher than 10º C and between 800 – 1400 m higher than 7º C (Bower *et al*., 2002). This presence is mainly attributed to the MOW lower core (Iorga & Lozier, 1999a, 1999b), with values of potential temperature and salinity ranging from 8º – 12º C and 35.6 – 35.9 (Practical Salinity (SP)), respectively, between 1000 – 1100 m depth (Iorga & Lozier, 1999a, 1999b). For comparison reasons, the relation between SP and SA, taking the North Atlantic as a reference, can be assumed as $SA = SP + 0.16504$ g kg^{-1} (McDougall *et al*., 2012) (refer to chapter 3 for more information).

2.3. Mediterranean Water Eddies

The first two observations of deep lens-shaped structures were published in 1969, one describing a small deep eddy off Cape São Vincente (Swallow, 1969) and another describing large cells of Mediterranean Water in the Madeira-Canaries Region (Piip, 1969). However, it was not until 1978 that McDowell & Rossby attributed for the first time the term “meddy” to

describe a large anticyclonic lens of warm and saline water with characteristics from Mediterranean Water (Mediterranean Water Eddy) off the Bahamas. Since then, several authors have described the physicochemical characteristics of meddies identified during hydrographic surveys (Armi & Stommel, 1983; Armi & Zenk, 1984; Käse & Zenk, 1987; Armi et al., 1989; Arhan et al., 1994) and using floats e.g.: SOFAR; RAFOS (Armi et al., 1989; Richardson et al., 1989; Pingree & Le Cann, 1993b; Prater & Sanford, 1994; Richardson & Tychensky, 1998). There were also attempts to describe their formation and behaviour through numerical models (McWilliams, 1984; Hogg & Stommel, 1990; Jungclaus, 1999; Maas & Zahariev, 1996). Richardson et al. (1991) compiled possible meddy observations based on data from hydrographic stations and reported meddy observations from the literature. The first direct observation of a meddy being formed off Cape São Vincente was not until 1993 under the AMUSE experiment (Bower et al., 1995, 1997).

With the previous methodology, the study of meddies depended on oceanographic campaigns, which are expensive and involve many logistics. At the beginning of the '90s, a new era of meddy studies began when Stammer *et al*. (1991) detected, for the first time, meddies using satellite altimetry, and found that their surface signal was detected as isolated positive anomalies of Sea Surface Height (SSH). Still on the subject of remote sensing, Pingree & Le Cann (1993a) observed a meddy using infrared (IR) satellite images. Meanwhile, Savenkoff *et al*. (1993) thought that if meddies' cores kept their original physicochemical characteristics for over a year, this transport might not be exclusive for salt and heat. These authors described the presence of Mediterranean microbial communities in two meddies.

At the end of the 20th century, a great deal was known about meddies but at the same time, a lot was yet to be discovered. The presence of meddies north of the Iberian Peninsula was first described by Paillet *et al*. (1999), (although it had been observed through hydrographic stations) which gave way to the possibility of new meddy generation sites. At the beginning of the 21st century, new methods and theories emerged like the use of SST to identify meddies' surface signature Oliveira *et al*. (2000) and the concept that deep cyclonic eddies with warm and saline cores could be associated with meddy formation sites (Oliveira *et al*., 2000; Richardson *et al*., 2000; Carton *et al*., 2002; Serra *et al*., 2002; Barbosa Aguiar *et al*., 2013). Other groundbreaking discoveries were the use of seismic reflectance (Biescas *et al*., 2008; Pinheiro *et al*., 2010) and acoustic tomography (Dushaw *et al*., 2017) to observe the thermohaline structures of meddies with increased resolution.

Meddies are characterized as lens-shaped salinity and temperature anomalies (corresponding to MOW), with up to 1 and 4º C respectively, when compared against background values (Richardson *et al*., 2000). Meddies are mostly rotating anticyclonically with azimuthal speeds up to 30 cm s^{-1}, with diameters ranging from 40 – 150 km, and propagating westward with translation speeds of 1 – 3 km day^{-1} (Richardson *et al*., 1991, 2000). Their lifespan is, on average, 1 – 2 years, although they can survive 4 – 5 years, depending on their decay rate and pathway, which dictates whether they will dissolve into the environment or collide against, i.e., seamounts and dissipate (Richardson *et al*., 2000; Ienna *et al*., 2014). The dissipation by collision depends on the capacity of ambient currents to "throw" a meddy against a seamount in a destructive manner (Bashmachnikov *et al*., 2009a).

The only found article describing the biogeochemical characteristics associated with meddies was by Alonso-González *et al*. (2009) reporting high Particulate Organic Carbon (POC) concentrations throughout the whole water column in the presence of a meddy, in the scope of a hydrographic survey. The authors suggested that meddies may significantly contribute to the deep-water transport of organic matter.

Meddies formation mechanism is unknown, but several authors have devised theories to explain it. The leading theory for the separation of meddies from the MUC is their baroclinic instability and relative vorticity generated from friction with the bottom (i.e., the continental slope) that later detaches due to bottom topography which causes rapid changes in direction (Barbosa Aguiar *et al*., 2013; Bashmachnikov *et al*., 2015a).

According to their formation site, meddies are generally divided into two categories: southern meddies, formed at the southern and southwest Iberian Peninsula (Portimão Canyon, Cape São Vincente, Goringe Bank, Estremadura Promontory); and northern meddies, formed at the northwestern Iberian Peninsula (Aveiro/Porto Canyons, Galicia Bank, Cape Finisterre, Cape Ortegal) (Serra & Ambar, 2002; Barbosa Aguiar *et al*., 2013; Bashmachnikov *et al*., 2015a) (Figure 2.1). This division refers to the Estremadura Promontory and the differences are both in probability of generation (three times less to the north) and in terms of physical properties (higher relative vorticity, smaller radius, and stronger frequency buoyancy anomaly to the south) of the meddies (Bashmachnikov *et al*., 2015a).

Meddies can also be categorised according to their pathways in the ocean. There are three zonal pathways: Southern, Central and Northern meddy paths, located between 34 – 36.4º N, 37.5 – 41º N, and 41 – 45º N, respectively, extending until the Azores plateau and the MAR (with the

southern path presumably turning southwest afterwards) and a Coastal path following the northwestern coast of Africa, from Portimão Canyon and Cape São Vincente to the Canary Islands (Bashmachnikov *et al*., 2015a). There is a strong influence of topography and ocean currents, i.e., the Azores Current (AzC), which results in convergence and sometimes transfer of meddies along these paths (Bashmachnikov *et al*., 2015a).

Meddies have also been divided according to their lifetime by Ciani *et al*. (2017). The authors classified meddies into three groups: lifetime exceeding 2 years, lifetime between 1 and 2 years, and lifetime less than 1 year.

The number of meddies forming in the North Atlantic is estimated to be between 15 – 30 per year (Bower *et al*., 1997; Richardson *et al*., 2000). Since most studies focus on the southwest corner of the Iberian Peninsula, their geographical distribution and abundance are most likely underrated. The work of Ienna *et al*. (2022) shows that the abundance of northern meddies may be greater than initially anticipated.

By computing the difference between the peak salinity of a meddy's core and the salinity of its closest point of MOW, Bashmachnikov *et al*. (2015a) could infer whether meddies are locally generated or advected. This also led to the observation that meddy core peak salinity was lower for northern meddies than for southern meddies since this property decreased by entrainment of MOW with fresher ambient water as it traveled north. The authors even discussed the possibility that ambient water penetrated the core itself in northern meddies, as opposed to southern meddies which could maintain their core properties for thousands of kilometres. Another conclusion from this work was that registered peak salinity values higher than 36.3 represented southern meddies, while peak salinity values below 36.2 represented northern meddies. In the case where two meddies merged, their radius and thickness increased while the azimuthal velocity decreased, but the core salinity did not show significant changes (Bashmachnikov *et al*., 2015a). These observations agree with the results from Wang *et al*. (2019) who concluded that during the merging of two anticyclonic eddies, the eddy kinetic energy decreases and the eddy potential energy increases (energy cascade), while mass is conserved.

For the identification of meddies, the criteria proposed by Richardson *et al*. (1991) and used by several authors (i.e., Bashmachnikov *et al*., 2015a; Ienna *et al*., 2022), are a core located between 500 – 1500 m depth, with a salinity anomaly higher than 0.2, and extending over a 200 m layer. In addition to Richardson's criteria, Bashmachnikov *et al*. (2015a) added two new

criteria to their methodology: maximum temperature anomaly at mid-depths exceeding 0.5º C, and negative buoyancy frequency anomaly in the meddy core.

2.4. Cyclonic Mediterranean Water Eddies

There is not much agreement within the scientific community about the definition of meddies. Hence, this chapter describes deep Mediterranean Water eddies that rotate cyclonically. Despite being misunderstood and not consistently recognised by the scientific community, cyclonic meddies contribute to the advection of salt and heat into the North Atlantic, comprising about 30% of the meddy population (Barbosa Aguiar *et al*., 2013).

As mentioned above, the MOW leaves the Strait of Gibraltar separated into two main branches. Most of the anticyclonic meddies are found in the lower layer around 1000 m depth, although some cores can be shallower. Conversely, cyclonic meddies usually have their core at approximately 600 m depth, generally shallower than anticyclonic meddies and travelling north-westward, as opposed to the latter (Barbosa Aguiar *et al*., 2013).

Carton *et al*. (2002) described the interaction between an anticyclonic and a cyclonic meddy as a baroclinic dipole. This interaction influenced both eddies' deformation of the velocity field and motion, and the result of several simulations showed that their generation site had to be near each other.

Richardson *et al*. (2000) tracked and described the interaction between a meddy and a cyclone for six months. Both eddies had approximately 100 km in diameter and their cores were 100 km apart. The authors report that although the cyclone's temperature was colder than the meddy's, both eddies exchanged water around the peripheries.

Going further back into historical records, several authors mention the interaction of cyclones with meddies (Pingree & Le Cann, 1993a; Prater & Sanford, 1994; Serra *et al*., 2002).

2.5. Meddies Sea Surface Expression

The use of satellite altimetry in the study of meddies has been a powerful tool pushing our knowledge much further than anyone could imagine. This tool has been used and improved for the last three decades and is considered a reliable source of information (https://www.aviso.altimetry.fr/en/applications/ocean/mesoscale-circulation.html).

The first attempt at this methodology was by Stammer *et al*. (1991) who used Geosat altimetric height measurements with 6.8 km resolution and obtained promising results. The idea arose from the works of Käse & Zenk (1987) where the authors observed a surface drifter getting trapped above a meddy, implying that they should have surface vorticity signals.

While travelling, a meddy compresses the water column in front of its core (relative to the direction of propagation) inducing anticyclonic rotation, due to the conservation of potential vorticity, and causing isopycnals to lift (Ienna *et al*., 2022). This isopycnal lifting can propagate to the surface increasing the SSH (Bashmachnikov *et al*., 2013; Ienna *et al*., 2022).

The sea surface expression of meddies intensifies northward due to an increase in the ratio between the Coriolis force and the buoyancy frequency (Ienna *et al*., 2022). It is also strongly shaped by the surrounding environment, meaning that the properties of the surface expression can partially decouple from the properties of the meddy itself (Ienna *et al*., 2022). This influence of the surrounding environment is significant to consider, mainly because while meddy core properties decay with distance from its generation site (Richardson *et al*., 2000), its surface expression intensifies westward, accompanied by an increase in radius (Ienna *et al*., 2022).

Thus, the above-described methodology is a feasible tool for tracking meddies throughout their lifetime, enabling a forecast and hindcast of their history (Bashmachnikov *et al*., 2009b; Bashmachnikov *et al*., 2013), while keeping in mind two problematics: the dependency on *in situ* data to distinguish meddies from other mesoscale features (i.e., mesoscale eddies, Rossby waves); and the interference from ambient currents and eddies which affect their surface expressions.

Another characteristic of meddies´ sea surface expressions is their SST anomaly values. In fact, and although observed in previous works, the results described by different authors can be contradictory. Oliveira *et al*. (2000) described their surface expression as a warm core surrounded by colder ambient water or a thermal front showing a circular feature above or shifted from the position of the meddy core. Contrarily, Bashmachnikov *et al*. (2013) described two meddies with negative SST anomalies above their cores surrounded by fronts of warmer ambient waters.

3. Methodology

3.1. NA-VICE Cruise KN207-03

In the context of the NA-VICE cruise KN207-03, the R/V Knorr left the São Miguel harbour, Portugal, heading to Reykjavik, Iceland (Figure 3.1). This project was led by Rutgers University and featured more than 30 international scientists, including two oceanographers from the University of the Azores. During this cruise, several CTD profiles were taken between 37 and 65º N and 21 and 35º W. While most of the profiles had a maximum depth of 150 or 300 m, seven stations reached depths of 1500/2000 m. In total, 196 CTD casts were made from 98 stations (downwards and upwards). The R/V Knorr was also equipped with a hull-mounted ADCP and a rosette for water sampling. For this work, only the CTD and ADCP data were analysed. All the datasets available from this cruise can be found at https://www.rvdata.us/search/cruise/KN207-03.

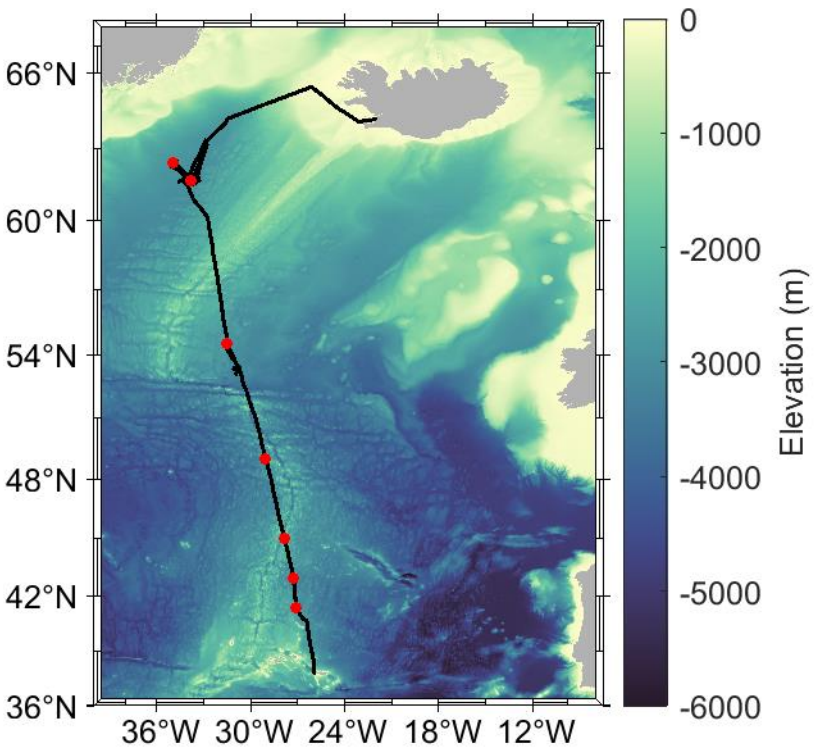

Figure 3.1 – Bathymetry map of the NE Atlantic (data source: GEBCO 2023). Grey areas represent land (elevation ≥ 0). The solid black line represents the R/V Knorr ship´s track from 13th June to 16th July 2012. This expedition was carried out as part of the framework of the international project NA-VICE (cruise reference: KN207-03) and traversed ~2000 nautical

miles from Ponta Delgada, Azores to Reykjavik, Iceland. The red dots represent the positions of the selected CTD station locations used for this work.

3.2. *In situ* Data

3.2.1. CTD

Out of the 98 CTD stations, made with an SBE 911plus from Sea-Bird Electronics, Inc., coupled with a Dissolved Oxygen (DO) SBE 43 sensor, all mounted on a Rosette system, seven (represented in Fig. 3.1) were selected for reaching depths of 1500 and 2000 m (Table 3.1). the remaining profiles were not considered for the identification of meddies since they were all "shallow" (< 300 metres). However, these profiles were useful as they were included in the interpolation of oceanographic data (vertical sections) along the ship´s track. For this study the following variables, measured during the CTD casts (or estimated using these values) were: *in situ* temperature (in ° C), SP (no units), pressure (dbar), density (kg m^{-3}), and DO (ml l^{-1}).

After visual inspection, six out of the seven stations showed a good agreement between both cast directions. However, one of the stations (station 13) showed anomalous values in the downwards salinity profile. An attempt was made to clear the anomalies by removing all values that were higher or lower than the mean plus three times the standard deviation (keeping 99.73% of the values around the mean (Speagel, 1988). The results for station 13 showed a significant improvement. Nevertheless, the upward profiles were chosen over the downward profiles to avoid data biases.

Since the 80s, seawater was described using SP as recognised by the International Oceanographic Commission (IOC) according to the Equation of State of Seawater – 1980 (EOS-80). In 2009, the EOS-80 was replaced by the Thermodynamic Equation of Seawater – 2010 (TEOS-10) in IOC's 25th assembly (https://www.teos-10.org/). The main change was the adoption of a new variable, SA, to describe the mass fraction of salt in seawater as opposed to the previous SP which measured the conductivity of seawater. The SA is calculated based on the following equation:

$$\text{Eq. 1. } S_A = \frac{35.165\,04\ g\ kg^{-1}}{35} S_P(1 + R^{\delta}), \text{ for non-Baltic seas.}$$

In this expression S_A is the SA, S_P is the SP, and R^{δ} is the SA Anomaly Ratio calculated based on an internal function of the Gibbs-SeaWater (GSW) Oceanographic Toolbox using pressure, longitude, and latitude (McDougall & Barker, 2011). This toolbox comprises several functions

for computing the thermodynamic properties of seawater (https://www.teos-10.org/pubs/gsw/html/gsw_contents.html) and is available in various processing software.

Using the GSW Oceanographic Toolbox for MATLAB: SA (g kg^{-1}) was computed from SP, pressure, longitude and latitude; Conservative Temperature (CT) (° C) was computed from SA, *in situ t*emperature and pressure; and the Brunt-Väisälä frequency squared (s^{-2}) was computed from SA, CT, pressure and latitude. Although these variables have been standardized, the detection of meddies implies knowing their anomaly in relation to background values. For this reason, the useful variable for identifying meddies is SP and *in situ* temperature since they can be compared against published climatology maps of the NE Atlantic (Bashmachnikov *et al*., 2015b). The vertical profiles of CT and SA are shown in Appendix I.

To confirm the presence of a meddy, Richardson *et al*. (1991) criteria complemented by Bashmachnikov *et al*. (2015a) criteria were used employing the MEDTRANS dataset (https://www.mare-centre.pt/en/research/data-library/medtrans-data), the most recent climatology of temperature and salinity distributions in the Subtropical Northeast Atlantic (25 – 45º N and 6 – 35º W), with a vertical resolution of 25 m depth and a horizontal resolution of 30 km (Bashmachnikov *et al*., 2015b). This dataset was used to make horizontal sections of salinity and temperature fields at several depths as well as, vertical profiles, using the closest point of the dataset to the eddies centre.

Temperature-Salinity (T-S) diagrams (or plots) illustrate two main properties of WMs: temperature and salinity (Pickard & Emery, 1982). Traditionally, these graphics also represent density by adding curves of equal density (isopycnic or iso-density lines). The T-S diagrams were created in this study to infer the main WMs of the North Atlantic basin according to their temperature, salinity (SP), and density signatures, following a study compilation by Magalhães-Loureiro (2022), which summarizes the major WMs' properties in the Atlantic Ocean (Appendix II). The areas occupied by these WMs were then overlapped on the T-S diagram. The isopycnals were computed using GSW *in situ* density function with a reference pressure of 10.1325 dbar (absolute reference pressure at sea level) (McDougall & Barker, 2011).

The vertical sections obtained by interpolating the CTD casts performed along the ship's track were processed and analysed using the software package Ocean Data View (version 5.6.3) (ODV) (https://odv.awi.de/). The complete dataset containing all 98 stations was used to create sections of SP, temperature, DO, and Brunt-Väisälä frequency (computed using ODV's TEOS-

10 toolbox of physical properties). A costume sample filter was applied to the salinity parameter allowing only values between 34.5 – 36.5, which, based on measured *in situ* values, was found acceptable for this representation. All the parameters were represented by depth as a function of latitude from 40 to 63º N, and the values were gridded using ODV's DIVA gridding software with a scale of 24 × 24 permille (depth over latitude).

Table 3.1.: Name of the selected stations according to the CTD log ("u" refers to an upward cast). Stations' geographical coordinates are provided in degrees of longitude and latitude and the distance between stations is given in kilometres (km). The time of stations' casts is indicated in Coordinated Universal Time (UTC) (day/month/year) and in Julian days for leap years, respectively.

Station Name	**Latitude**	**Longitude**	**Distance between Stations**	**Date**	
Up	**N**	**W**		**UTC (d/m/y)**	**Julian day**
u20703004	41.3503	27.1142	**km**	16/jun/12	168.91
u20703012	42.9503	27.2342	178	19/jun/12	171.64
u20703013	45.0015	27.8565	223	20/jun/12	172.27
u20703017	48.9965	29.0288	453	21/jun/12	173.65
u20703044	54.5432	31.4870	639	28/jun/12	180.77
u20703071	61.6938	33.7778	806	04/jul/12	186.83
u20703091	62.4280	34.9687	102	09/jul/12	191.07

3.2.2. ADCP

Velocity measurements were made using a hull-mounted ADCP installed on R/V Knorr. The Shipboard ADCP data acquisition system was the University of Hawaii Data Acquisition System or UHDAS. The ADCP had two devices from Teledyne RD Instruments: an Ocean Surveyor operating at 75 kHz (OS-75) in BroadBand (BB) and NarrowBand (NB), and a Workhorse operating at 300 kHz (WH-300). The OS-75 was used for this work in its NB mode for its higher range and accurate velocity measurements (Hummon & Firing, 2003).

The data calibration and editing were verified using the Common Ocean Data Access System (CODAS) software (https://currents.soest.hawaii.edu/docs/adcp_doc/codas_doc/index.html),

Using MATLAB, the current velocity measurements were plotted in vertical sections in their two dimensions, with "U" (zonal velocity) being positive towards the East, negative towards the West, and "V" (meridional velocity) being positive towards the North, and negative towards the South. Two types of vertical sections were obtained: depth as a function of time and depth as a function of latitude. The vertical sections were completed by horizontal profiles to represent the ship's track when passing stations 4 and 12, with the current velocity measurements represented as arrows concerning the first and last layer measured by the ADCP.

3.3. Satellite Data

3.3.1. Altimetry

Altimetry data was downloaded from Copernicus' Global Ocean Gridded L4 Sea Surface Height and Derived Variables Reprocessed 1993 Ongoing product (https://doi.org/10.48670/moi-00148). This product from Copernicus Marine Service uses a twenty-year, 1993 – 2012, altimetry dataset to compute Sea Level Anomaly (SLA), which is estimated by interpolation and merging of Level-3 along-track measurements from several altimeter missions available, resulting in a Level-4 product with 0.25º × 0.25º resolution updated annually. Other variables obtained from this product were surface geostrophic eastward and northward sea water velocity, and sea surface height (SSH) above sea level standard error. The formal mapping error for the location of stations 4 and 12 was plotted and found to vary between 1 – 3 cm (Appendix III).

The SLA daily measurements were downloaded for the period of 2008 – 2014. Horizontal maps of SLA with geostrophic currents and velocity modulus computed from the surface geostrophic seawater velocities for the time and location of the cruise were made to compare against the position of the stations. After identifying the eddy structures, these were followed back and forth in time by making SLA maps of each month's first and fifteenth days. These maps present bathymetric data from GEBCO 2023, with a 15 arc-second interval grid, available at: https://www.gebco.net/data_and_products/gridded_bathymetry_data/.

Further analyses used an eddy detection algorithm for MATLAB – *SimpleEddyDetection*, developed by Xu (2020) and available at https://www.mathworks.com/matlabcentral/fileexchange/103810-simpleeddydetection. Some adjustments to the algorithm were made namely, to transpose the latitude and longitude coordinates inside the function to ensure it correctly saved the eddies boundaries. This

algorithm computes eddy boundaries using SLA contours. It runs two "for" functions (loop functions), one dedicated to detecting anticyclones and another dedicated to detecting cyclones. The outputs of the function are the type of eddy (cyclonic or anticyclonic), the amplitude of the eddy in centimetres (with the coordinates of the maximum/minimum value), the centre and edge of the computed eddy boundary, and the radius of the contour by approximation to a circumference (eddy radius).

3.3.2. Ocean Colour (OC)

Satellite OC images were downloaded from Canopus, a software developed at the University of Azores – Department of Oceanography and Fisheries to process satellite imagery. This system acquires daily Level-2 MODIS - AQUA (Table 3.2) images (from the National Aeronautics and Space Administration (NASA) OC website: https://oceancolor.gsfc.nasa.gov/), with 1 × 1 km^2 resolution, that contain at least 25% of an area of interest previously defined. The Level-2 images are processed by applying the Plate Carree cylindrical projection and cropped to the area of interest. If an image has less than 5% of valid pixels, it is discarded. The downloaded products were nighttime – long wave SST 11 µm (º C); daytime – Chlorophyll-*a* (Chlor-a) (mg m^{-3}), Particulate Inorganic Carbon (PIC) (mol m^{-3}), Particulate Organic Carbon (POC) (mg m^{-3}), kd_490 (m^{-1}), and Photosynthetically Active Radiation (PAR) (Einstein m^{-2} d^{-1}). Each product has a threshold within which the parameters are considered valid: SST [13.0 – 29.0º C], Chlor-a [0.001-3.000 mg m^{-3}], PIC [1.0×10^{-5}-0.05 mol m^{-3}], POC [10.0-1000.0 mg m^{-3}], kd_490 [0.01 – 5 m^{-1}], PAR [0 – 70 Einstein m^{-2} d^{-1}]. If a pixel presents a value outside of the threshold, it is discarded.

The images were post-processed after download using SeaDAS (version 8.3.0), a software from the NASA to process satellite imagery. This step consisted of cropping the images to the study area and applying a filter to smooth the image, in this case, arithmetic means of 3 × 3 pixels.

Table 3.2.: Description of the MODIS - AQUA ocean products acquired through the National Aeronautics and Space Administration (NASA) OC website (https://oceancolor.gsfc.nasa.gov/) and automatically downloaded and processed using the Canopus satellite processing system, specifying their name, acronym, and unit according to the International System of Units (SI). Taken from https://modis.gsfc.nasa.gov/data/dataprod/.

Name	Acronym	Unit	Description
Chlorophyll-*a* Concentration	Chlor-a	mg m^{-3}	Near-surface concentration of Chlor-a calculated using an empirical relation between *in situ* measurements (of Chlor-a) and blue-to-green band ratios of remote sensing reflectance. Dependent on the availability of three or more sensor bands from 440 – 570 nm spectral regime.
Diffuse Attenuation Coefficient at 490 nm	kd_490	m^{-1}	The kd_490 is calculated using an empirical relation derived from *in situ* measurements (of kd_490) and blue-to-green band ratios of remote sensing reflectance. Dependent on the availability of remote sensing reflectance in the blue-green spectral region (490 – 564 nm).
Particulate Inorganic Carbon Concentration	PIC	mol m^{-3}	Concentration of PIC calculated using *in situ* relations between water-leaving radiances, spectral backscattering coefficients, and concentrations of PIC (i.e.: calcium carbonate or calcite). Dependent on the availability of sensor bands near 443 and 555 nm.
Particulate Organic Carbon Concentration	POC	mg m^{-3}	Concentration of POC calculated using an empirical relation derived from *in situ* measurements of POC and blue-to-green band ratios of remote sensing reflectance.
Daily Mean Photosynthetically Available Radiation	PAR	Einstein m^{-2} d^{-1}	Estimation of daily average PAR at the ocean surface. This product is defined as the quantum energy flux from the Sun in the 400 – 700 nm range. Dependent on the availability of observed top-of-atmosphere radiances in the visible spectral regime that do not saturate over clouds.

4. Results

4.1. CTD

The CTD vertical profiles of temperature and salinity (Figure 4.1) show a clear segregation between profiles 4, 12, 13, and 17, made south of 50º N (southern profiles), and profiles 44, 71, and 91, made north of 50º N (northern profiles). However, profile 17 appears to be located close

to a transitioning zone. This segregation is more pronounced in the first 400 m of the water column, and more noticeable in terms of temperature.

After 400 m depth, profile 4 starts to separate from profiles 12, and 13, showing higher values of both temperature and salinity decreasing at a steady slope. At 730 m depth, profile 12 starts increasing in both temperature and salinity, 1º C and 0.3, respectively, until 790 m. From 790 m to 860 m, it increases another 0.1º C and 0.1. Afterwards, it starts decreasing rapidly until 925 m, 1.4º C and 0.2, and then at a steady rate until it converges with the other profiles. As profile 12 reaches its deep salinity maximum, salinity in profile 4 stabilizes at 35.51 and at 930 m there is an increase in salinity of 0.04 until 1050 m and then a decrease of 0.4 until 1380 m. Between 1380 m and 1430 m there is a smaller increase in salinity of 0.01 and then it starts decreasing until it converges with the other profiles. There is no increase in temperature in profile 4, however, the decrease rate varies with depth. From 340 m to 760 m temperature decreases approximately 0.2 º C per 100 m. From 760 m to 1380 m, as salinity increases, temperature decreases by approximately 0.9º C per 100 m (from 11.5 – 5.7 ºC). From 1380 m to 1435 m there is no significant variations in temperature and after 1435 m it decreases at a steady rate until converging with the other profiles.

Profiles 13 and 17 show several salinity spikes between the surface and 940 m. These spikes coincide at the same depth, meaning the same phenomenon could influence them, although they are 440 km apart. The same can be said about the temperature, but the variations are much smaller. Profiles 44, 71, and 91 show a very pronounced thermocline between the surface and 30 m depth, varying from 4º C to 5º C. On the other hand, they present a very weak halocline that can go from 12 m to 20 m. Their slight variations represent a well-mixed water column, especially for vertical profile 71, which, from 150 m to 500 m, has a temperature variation of 0.02º C and no variation in salinity. In profile 44, temperature decreases slowly until 380 m after the thermocline, after which there is a very slight increase of 0.01º C as the salinity increases steadily. Between 500 m and 600 m, profiles 44 and 71 show a decrease in temperature and salinity. Below 950 m depth all profiles tend to stabilize except for profile 4.

From the analysis of the T-S diagram (Figure 4.2) it is possible to infer that as the cruise headed north, the NACW was confined closer to the surface with its lower limit decreasing from 970 m in profile 4 to 470 m in profile 17. Profiles 71 and 91 also show the influence of the NACW at the surface. In the first 30 to 40 m depth, no WMs were identified on profiles 4, 12, and 13. Profiles 4 and 12 present characteristics of MW between 1060-1300 m and 750-900 m,

respectively. In the first 300 m depth no WMs were identified in profile 44. Profiles 13, 17, 44, 71 and 91 present characteristics of the SAIW between 790 – 1100 m, 530 – 890 m, 300 – 830 m, 10 – 730 m, and 26 – 170 m, respectively. Only profiles 44, 71, and 91 show characteristics of NADW at depths higher than 1600/1700 m.

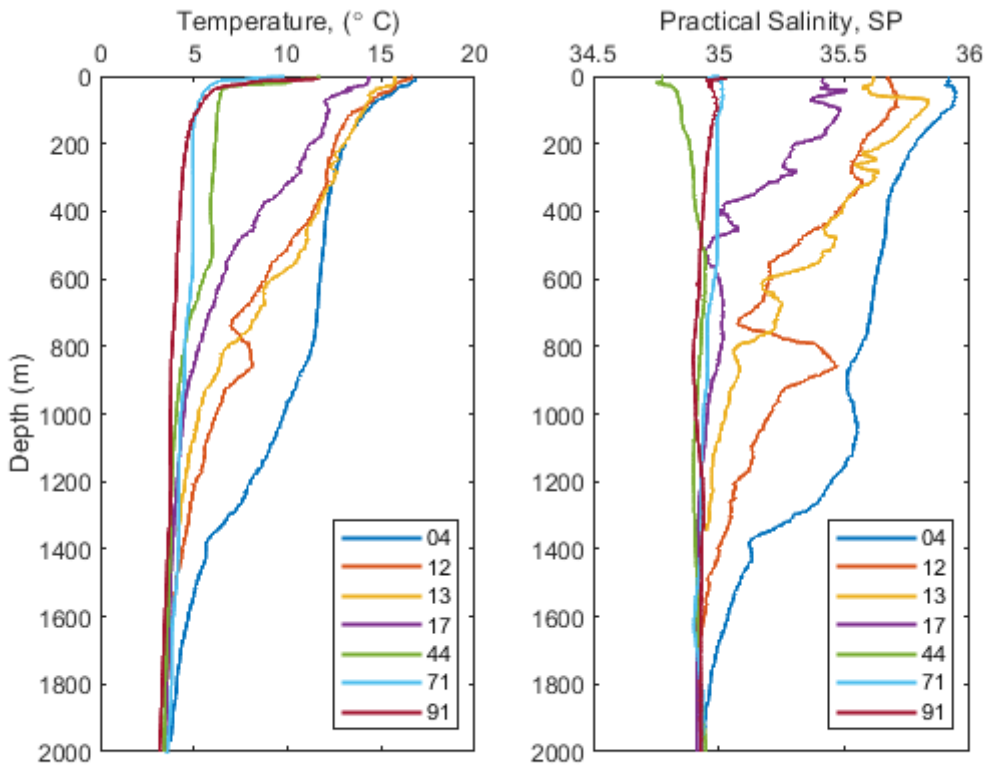

Figure 4.1 – *In situ* temperature and Practical Salinity (SP) vertical profiles of the seven selected stations, used in this study. The number associated with each profile is the last two characters of the station identification number according to the cruise KN207-03.

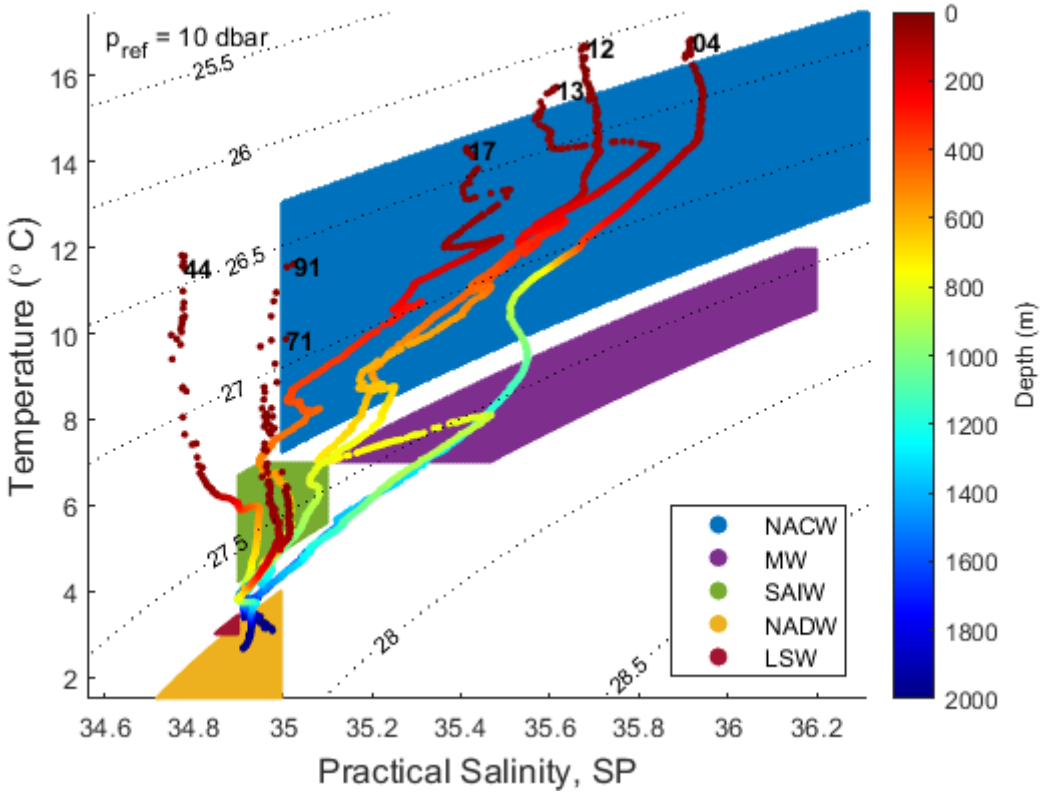

Figure 4.2 – Temperature-Salinity (T-S) diagram of the seven selected stations, used in this study. Each profile is identified with the last two characters of the station identification number from cruise KN207-03. Distinct Water Masses (WMs) and their extent in terms of temperature, salinity and density as reported by Magalhães-Loureiro (2022) are also represented. The identified WMs are NACW (North Atlantic Central Water), MW (Mediterranean Water), SAIW (South Arctic Intermediate Water, NADW (North Atlantic Deep Water) and LSW (Labrador Sea Water). See the text for a more detailed discussion.

Since profiles 4 and 12 show the presence of MW, these were evaluated according to Richardson´s and Bashmachnikov's criteria (Richardson *et al*. 1991; Bashmachnikov *et al*. 2015a). From 700 – 1300 m depth, the mean salinity is 35.51 on profile 4 and 35.19 on profile 12, corresponding to an anomaly of 0.2 and -0.04, respectively, in relation to the climatology. The peak salinity in profile 4 was 35.55 at 1050 m and in profile 12 was 35.46 at 860 m. Compared to the MEDTRANS climatology, the anomaly at 1050 m in profile 4 is 0.23, but the maximum anomaly is 0.24 at 1100 m. In profile 12, the anomaly corresponding to the peak salinity is 0.16. Between 700 – 1300 m depth, the temperature anomaly is 2.18ºC in profile 4 and -0.84ºC in profile 12, in relation to the MEDTRANS climatology. In profile 12, no temperature value was higher than the climatology. The MEDTRANS profiles in Figure 4.3 correspond to the closest point in the climatology to the stations: MEDTRANS 4 – 27º W, 41.4º

N; MEDTRANS 12 – 27.33º W, 42.89º N. For the visualization of the horizontal fields of salinity and temperature from 700 – 1300 m, with 100 m intervals, the reader is referred to Appendixes IV and V.

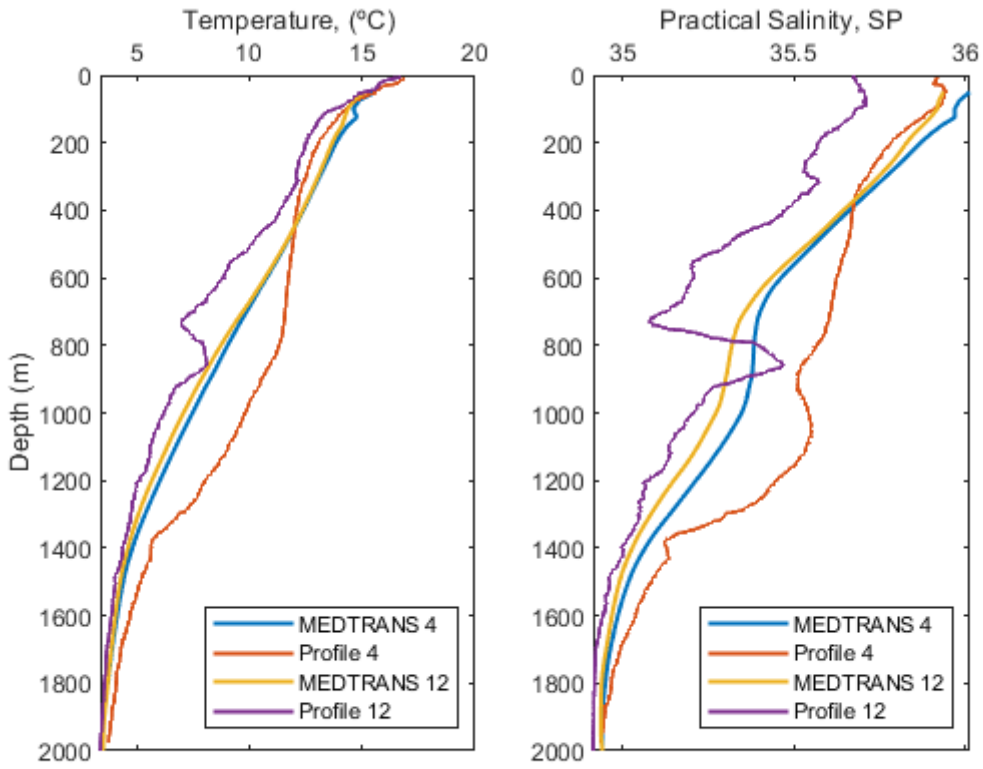

Figure 4.3 – Vertical profiles of *in situ* Temperature and Practical Salinity (SP) for stations 4 and 12 of the cruise KN207-03, and for the MEDTRANS climatology points closer to these stations. Profile MEDTRANS 4 corresponds to the position 27º W - 41.41º N and profile MEDTRANS 12 corresponds to the position 27.33º W - 42.89º N.

When plotting the density, computed as a function of CT, SA, and pressure (Figure 4.4a), it is possible to see the segregation of the northern and southern profiles in the first 400 m. Although the distance between the profiles is in the order of hundreds of kilometres, they all start converging to 27,7 kg m^{-3} at around 900 m, except for one. From 500 m to 800 m profile 4 shows a well-mixed water column followed by a picnocline between 800 m and 1300 m. At 930 m, profile 4 has a density of 27.3 kg m^{-3}. Profile 44 shows an intermediate density higher than the southern profiles but lower than the northern profiles with a well-mixed water column between 40 m and 500 m.

In the first 300 m of the water column both southern and northern profiles are well divided in terms of DO (Figure 4.4b). Bellow 300 m, as the southern profiles keep decreasing in DO, profile 4 increases until 650 m with several small fluctuations. Meanwhile, profile 44 starts decreasing at 500 m until 650 m when it reaches a DO minimum of 5.4 mL L^{-1}, close to profile 4. Profiles 12, 13, and 17 have DO minimums at 612 m, 576 m, and 425 m respectively with concentrations between 3.9 mL L^{-1} and 4.3 mL L^{-1}. Profile 4 starts decreasing at 700 m until it reaches its DO minimum at 974 m of 4.04 mL L^{-1}. Profile 71 shows a very well-oxygenated water column down to 1500 m. Profile 91 shows a well-mixed water column from 100 m to 730 m. Bellow 1800 m all profiles converge to a value of approximately 6 mL L^{-1}.

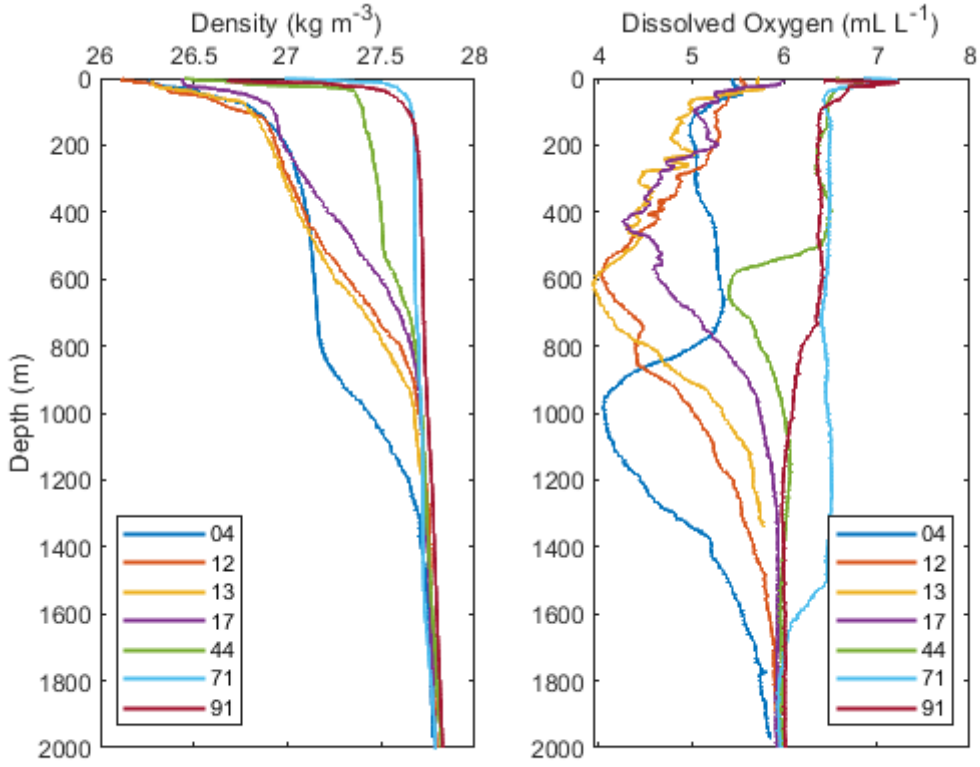

Figure 4.4 – Density and Dissolved Oxygen (DO) vertical profiles of the seven selected stations, used in this study. The number associated with each profile is the last two characters of the station identification number according to the cruise KN207-03.

When looking at the oxygen-salinity (O-S) diagram (Figure 4.5), there is no apparent relation between the two parameters, and it is interesting to notice how profiles 4 and 12 correlate with

oxygen varying inversely proportionate to SA. This happens between oxygen concentrations of 4.5 mL L^{-1} and 5.8 mL L^{-1} and salinities of 35.1 g kg^{-1} and 35.6 g kg^{-1}.

The temperature-oxygen (T-O) diagram (Figure 4.6) shows the relation between these two variables and the influence of meridional gradients at the surface. The biggest difference in oxygen happens between 8º C and 10º C, since at this temperature the northern profiles are at the surface while the southern profiles are hundreds of meters deep. Profile 44 shows a rapid decrease of oxygen at 6º C, switching from a characteristic northern profile to a southern profile. This change is also seen in the vertical profiles between 500 m and 600 m depth and the O-T diagram is characterized by a smooth "U" shape. The same "U" shape is seen in profile 4 between the concentrations of 5.3 mL L^{-1} and 4 mL L^{-1}.

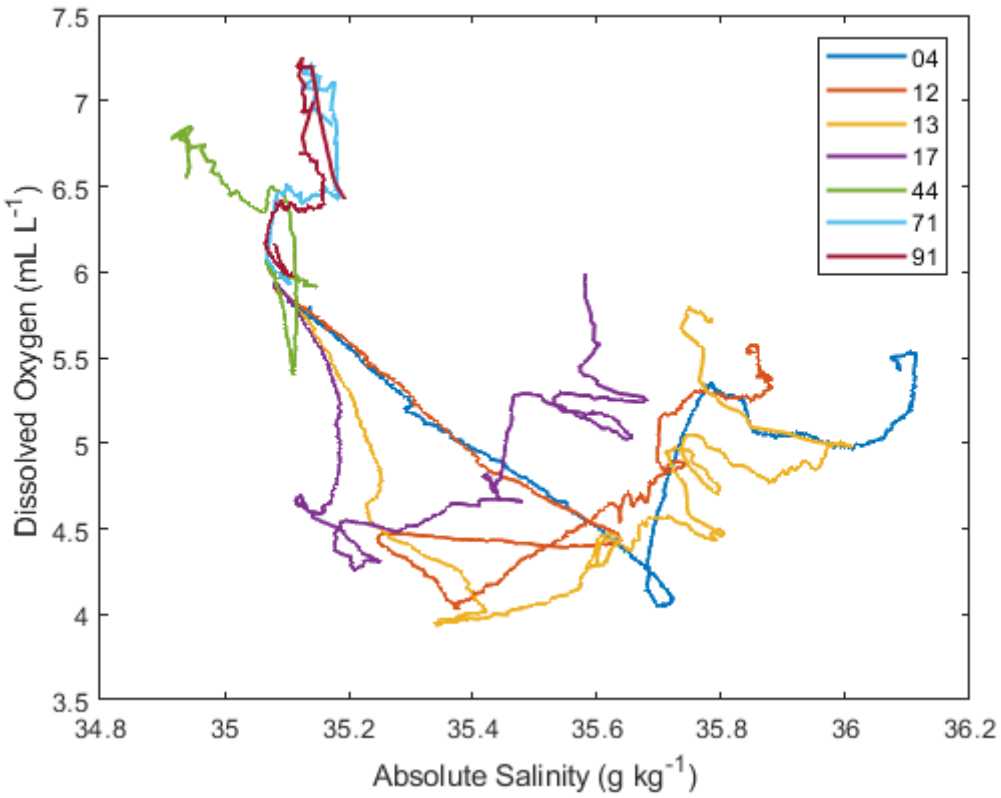

Figure 4.5 – Oxygen-Salinity (O-S) diagram of the seven selected stations, used in this study. The number associated with each profile is the last two characters of the station identification number according to the cruise KN207-03.

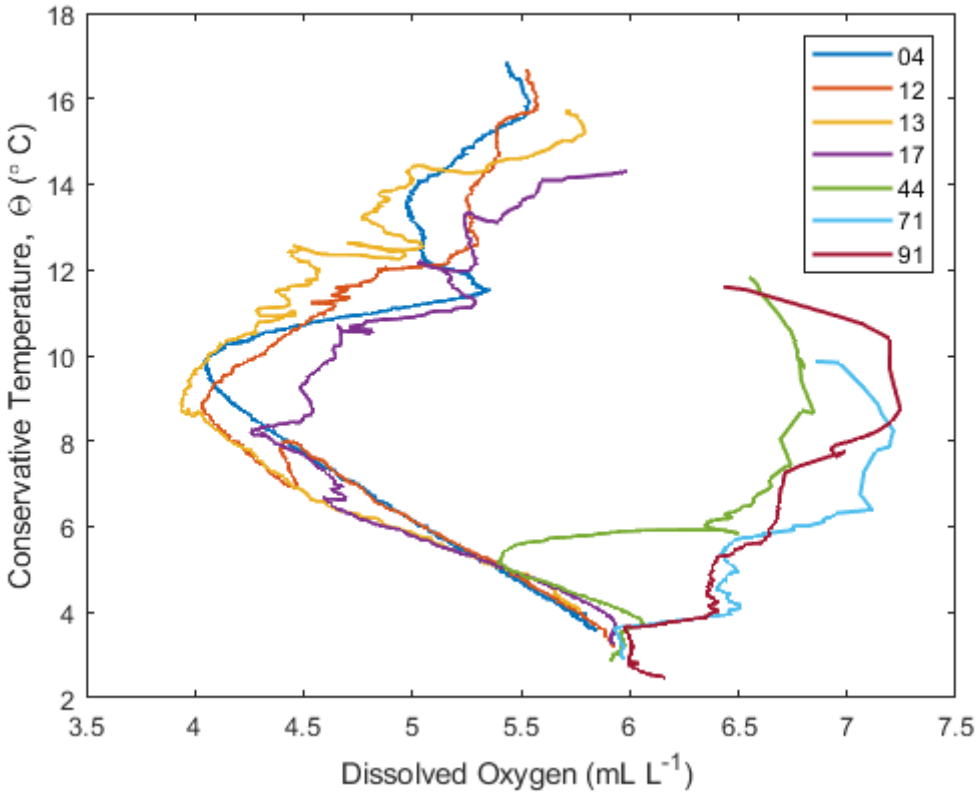

Figure 4.6 – Temperature-Oxygen diagram of the seven selected stations, used in this study. The number associated with each profile is the last two characters of the station identification number according to the cruise KN207-03.

The Brunt-Väisälä frequency shows how a particle of water will oscillate when displaced vertically. This way, if the water column is well stratified the frequency will be positive and the particle of water will tend to go back to its original position, but if the water column is well mixed the frequency will be close to 0 or negative and the displaced particle will remain in its new position. This parameter is a measure of the stability of the water column. By analysing Figures 4.7 and 4.8 it is possible to tell that the water column is more stratified in the first 100 m.

After the pycnocline, the profiles tend to show a decrease in stratification. In profile 17, the water column becomes more stratified between 200 m and 800 m. In profiles 12 and 13 this increase in stratification happens between 400 m and 900 m approximately. In profile 4, the water column is very well mixed between 400 m and 800 m and stratification increases between 800 m and 1400 m.

Profiles 71 and 91 correspond to a low-stratified well-mixed water column. Profile 44 is similar to profiles 71 and 91 except between 500 m and 800 m where there is an increase in frequency, meaning that the water is more stratified.

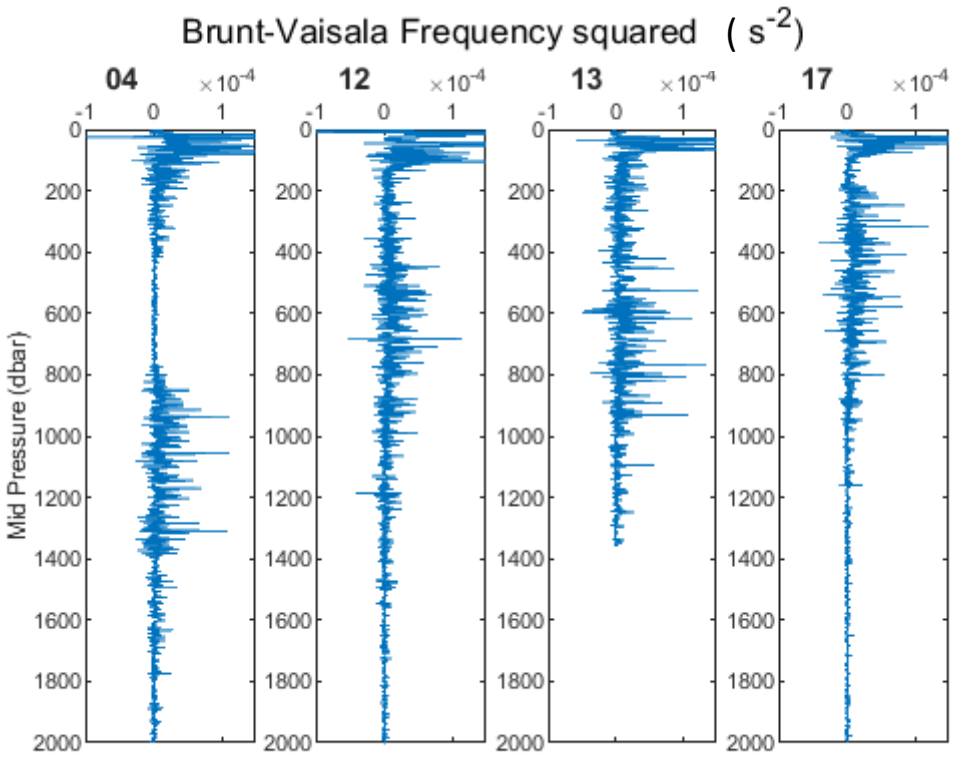

Figure 4.7 – Brunt-Väisälä frequency squared vertical profiles of stations 4, 12, 13, and 17. The number associated with each profile is the last two characters of the station identification number according to the cruise KN207-03.

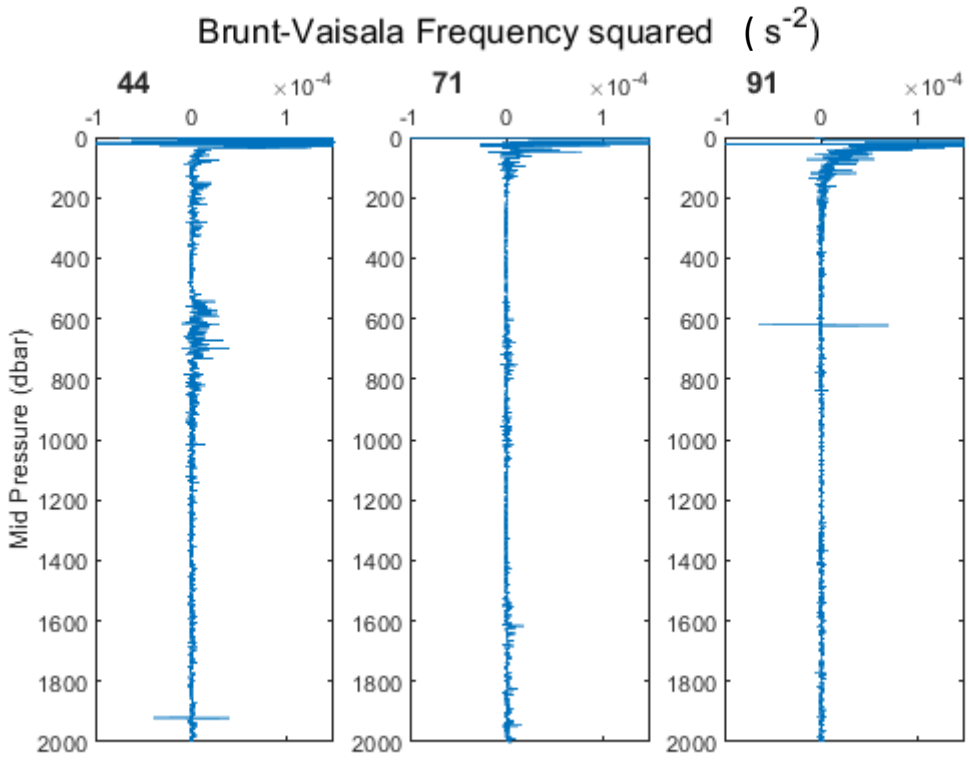

Figure 4.8 – Brunt-Väisälä frequency squared vertical profiles of stations 44, 71, and 91. The number associated with each profile is the last two characters of the station identification number according to the cruise KN207-03.

The vertical section of SA (Figure 4.9) shows strong horizontal gradients from 40 – 45º N, between 500 – 1000 m depth, as well as the presence of saline structures. More saline water is spreading further at the surface, as far as 50º N, while between 1000 – 1500 m depth it is confined to 42º N. Between 51 – 57º N, in the first 150 m depth, there is a low salinity WM, after which the SA increases again sinking to 500 m. Like the SA, the CT vertical section (Figure 4.10) presents very tilted isothermal from 40 – 45º N, some vertical, with the presence of a thermal structure at 42º N. From 52 – 62º N, the CT is highly stratified in the first 40 m depth and highly mixed below that.

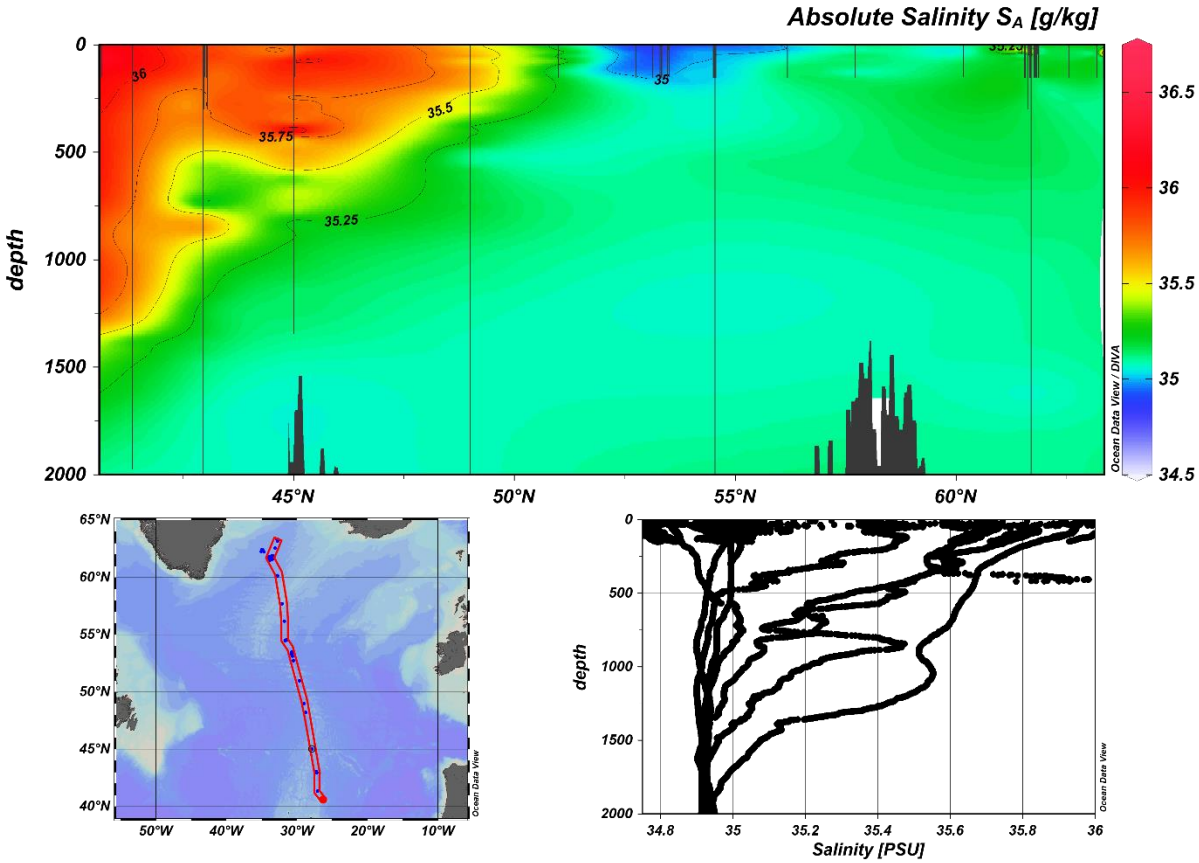

Figure 4.9 – Vertical section of Absolut Salinity (SA, in g kg^{-1}) along the cruise KN207-03's track. The location of the stations is shown in the bottom left figure and the vertical profiles from the stations inside the red polygon are represented in the bottom right figure.

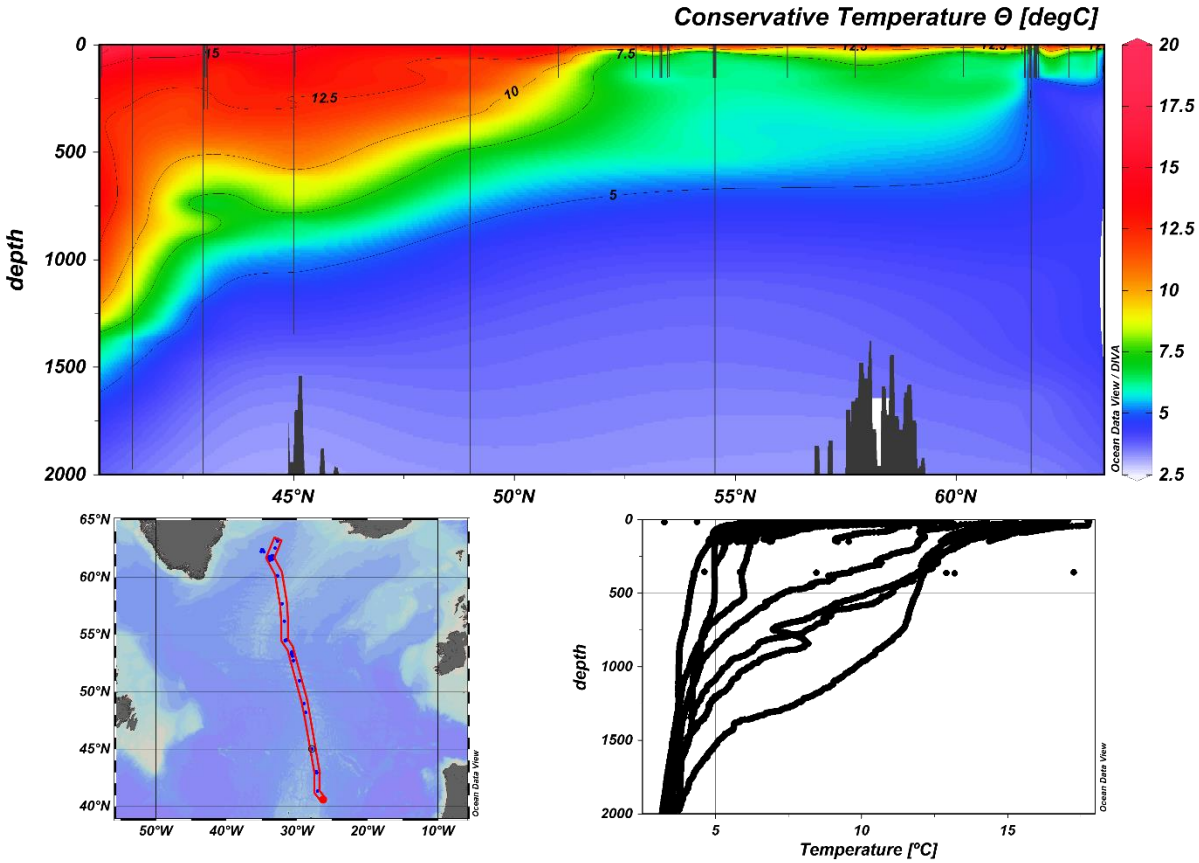

Figure 4.10 – Vertical section of Conservative Temperature (CT, in ºC) along the cruise KN207-03's track. The location of the stations is shown in the bottom left figure and the vertical profiles from the stations inside the red polygon are represented in the bottom right figure.

The oxygen vertical section (Figure 4.11) shows a minimum concentration between 800 – 1400 m depth from 40 to about 42º N connected to a blob of oxygen minimum between 250 – 1000 m depth, from 42 – 50º N. The oxygen concentrations seem to increase at higher latitudes. From 55 – 60º N around 500 m depth there is an oxygen maximum. Above this, at the surface, the waters are well-oxygenated. Oxygen concentrations increase between 250 – 1500 m depth after 62º N.

The Brunt-Väisälä frequency (Figure 4.12) shows that the water column is stratified in its first 100 m depth. Most of the deeper ocean is well mixed, except for the presence of a few features. At the location of station 4, the frequency increases between 800 – 1400 m depth, followed by an increase in frequency between 350 – 800 m depth throughout stations 12, 13, and 17. This feature shows a high resemblance with the oxygen concentration. At 60º N between 200 – 500 m depth, there is a strong increase in frequency.

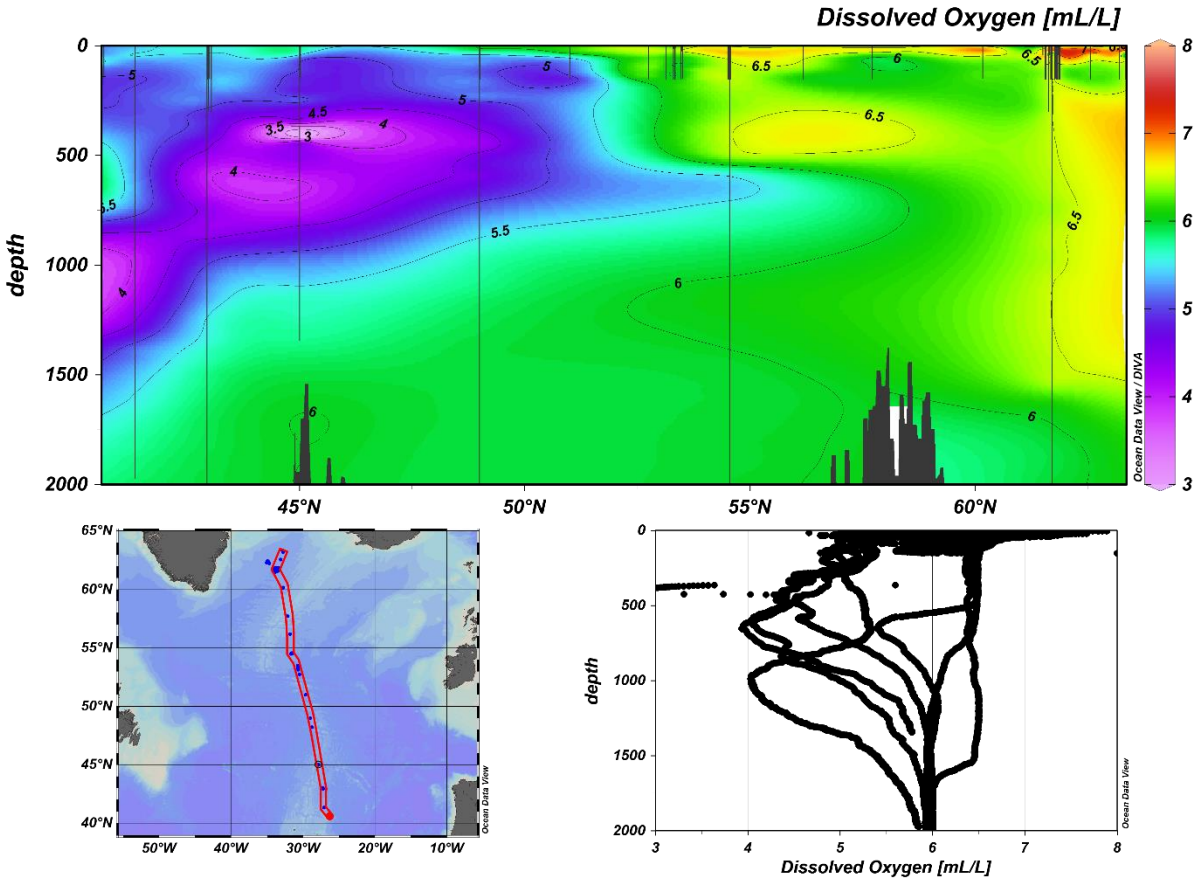

Figure 4.11 – Vertical section of Dissolved Oxygen (DO, in ml l^{-1}) along the cruise KN207-03's track. The location of the stations is shown in the bottom left figure and the vertical profiles from the stations inside the red polygon are represented in the bottom right figure.

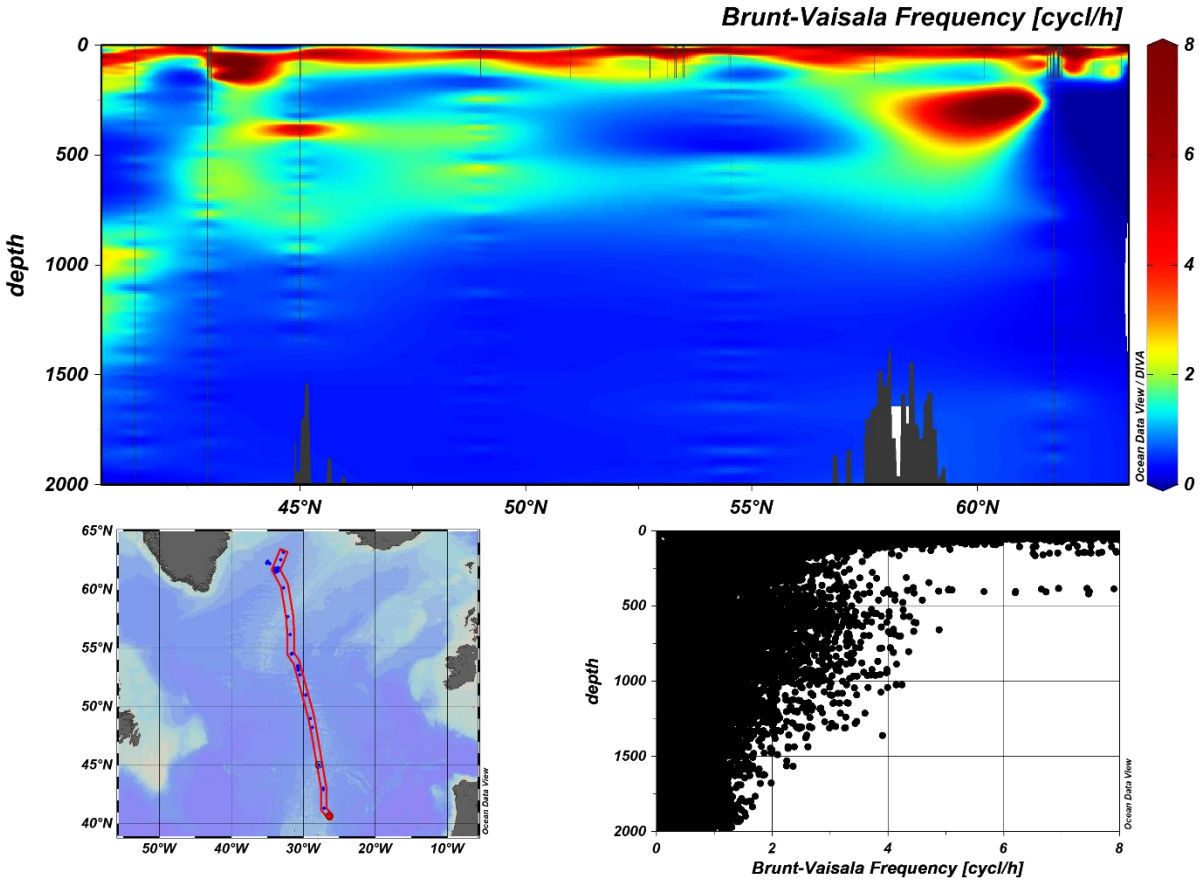

Figure 4.12 - Vertical section of Brunt-Väisälä frequency (cycles/h) along the cruise KN207-03's track. The location of the stations is shown in the bottom left figure and the vertical profiles from the stations inside the red polygon are represented in the bottom right figure.

4.2. ADCP

The current velocity data retrieved from the hull-mounted ADCP is the following for profiles 4 and 12 to get further insight into the eddies present at these stations. The data comprises averaged bins with 10 m vertical resolution, from 33 – 813 m, although the first layer data was removed during processing, so the valuable data ranges from 43 – 813 m depth.

For profile 4, the data shows an increase in velocity with depth in the zonal component, while the meridional component shows higher velocities at the surface, although much weaker than the zonal velocities (Figure 4.13). The variations along latitude show that the cruise stopped to sample south of the centre of the eddy observed through the cuts in the plotted data (Figure 4.14). The velocity, which was about -0.2 m s^{-1} at the surface, increases (in component U) with depth from -0.3 m s^{-1} to -0.4 m s^{-1} (Figure 4.15). Looking at the meridional variations, the velocity which was about -0.4 m s^{-1} drops to 0 m s^{-1} very suddenly, increasing immediately

after to 0.4 m s^{-1}, indicating the centre of an eddy. Later, it stabilizes between -0.1 m s^{-1} and 0.1 m s^{-1}.

Within the time range of profile 12, it is possible to identify higher velocity changes in the first 300 m depth, where the more significant changes are again seen in the zonal component "U" (Figure 4.16). When analysing the velocity measurements along latitude, there is a big data gap, meaning that, like with the anticyclone, the cruise stopped to sample close to the eddy centre (Figure 4.17). This is also seen in Figure 4.18, where a high density of velocity measurements marks the station's location. The difference between 40 m and 800 m is insignificant in this case.

As the ship headed north there was an increase in velocity in the zonal component (up to 0.3 m s^{-1}) and a change in the current direction in the meridional component. While the data in the lower latitudes shows that velocity changes a lot with depth in the first 800 m, the scenario is the opposite in northern latitudes. The direction of the currents seems to change more frequently with latitude, and the patrons change mostly horizontally with very few differences in depth (Appendix VI).

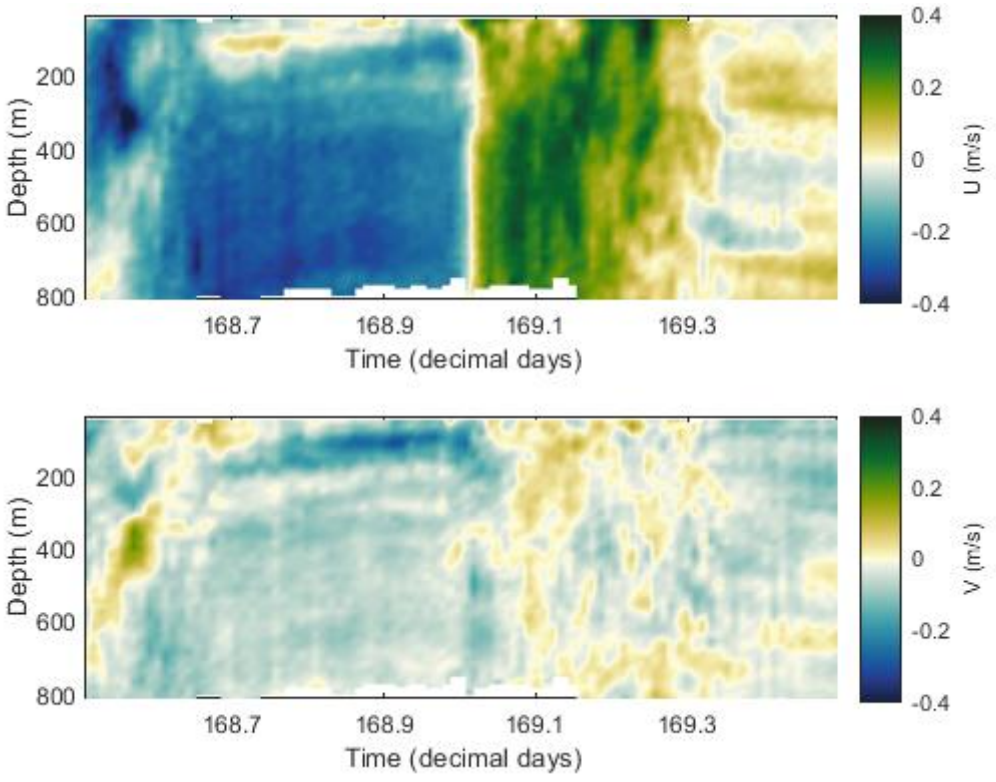

Figure 4.13 - Current velocity measurements obtained aboard the R/V Knorr (cruise KN207-03) from the hull-mounted ADCP along time, centred around the date of station 4. The top

figure shows the “U” component, positive towards the East and negative towards the West. The bottom figure shows the “V” component, positive towards the North and negative towards the South.

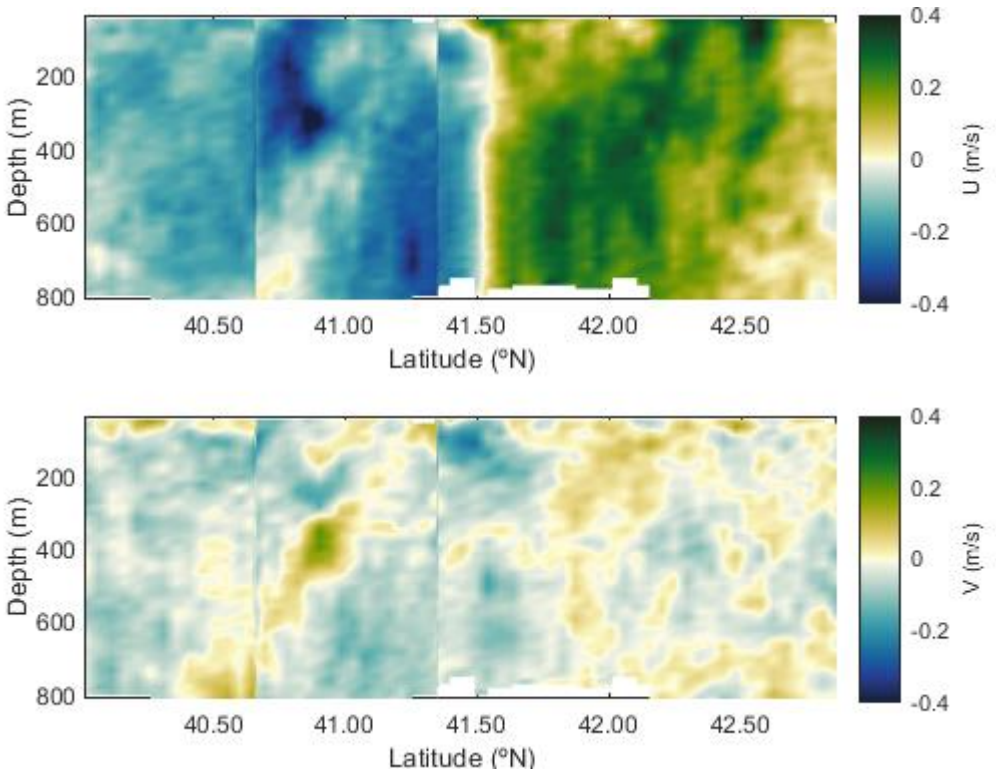

Figure 4.14 – Current velocity measurements obtained aboard the R/V Knorr (cruise KN207-03) from the hull-mounted ADCP along latitude, centred around the location of station 4. The top figure shows the “U” component, positive towards the East and negative towards the West. The bottom figure shows the “V” component, positive towards the North and negative towards the South.

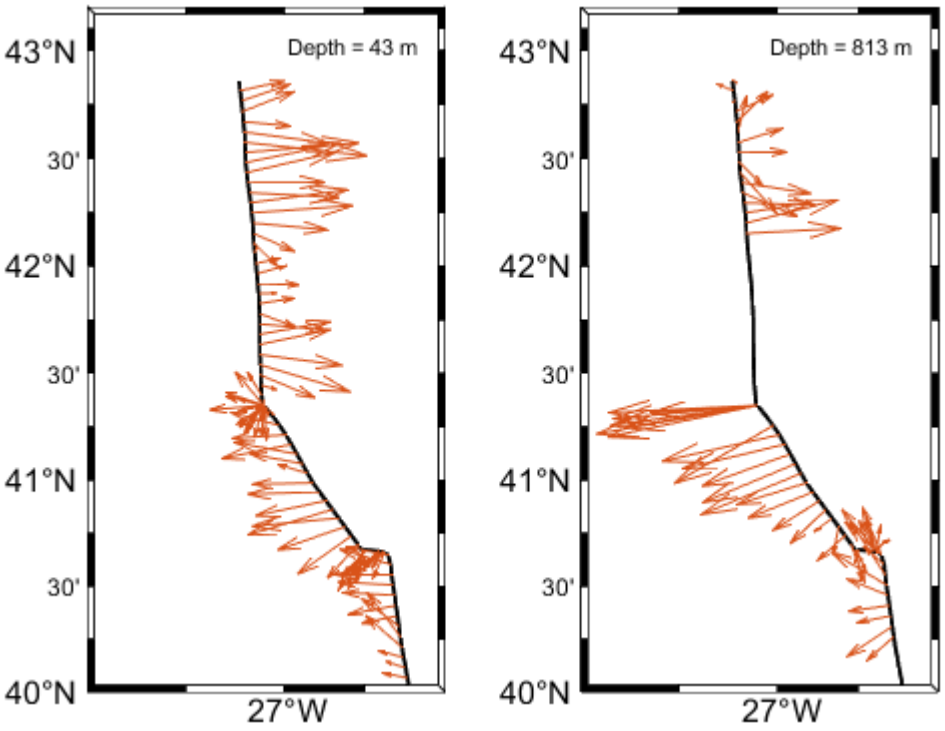

Figure 4.15 – Cruise KN207-03's track with vectorial arrows representing the direction and intensity of the current velocity from the hull-mounted ADCP, centred around station 4. The left figure represents the first depth layer at 43 m and the right figure represents the last depth layer at 813 m, after processing.

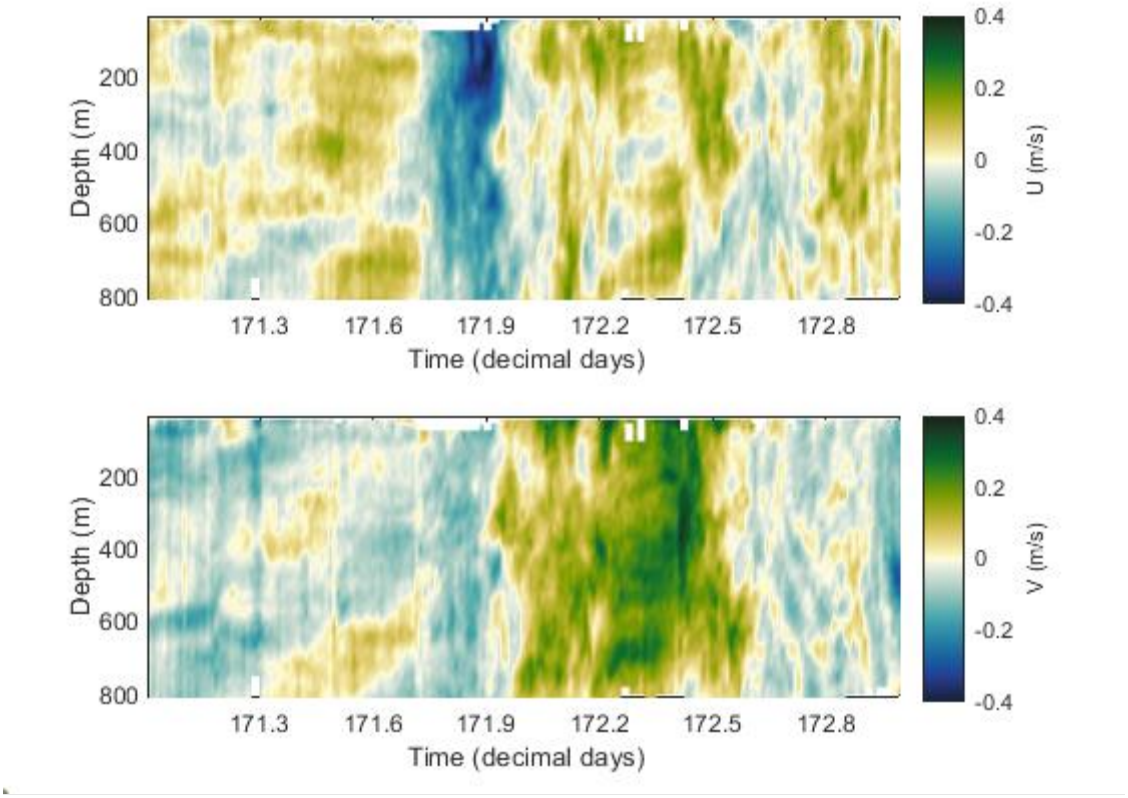

Figure 4.16 - Current velocity measurements obtained aboard the R/V Knorr (cruise KN207-03) from the hull-mounted ADCP along time, centred around the date of station 12. The top figure shows the "U" component, positive towards the East and negative towards the West. The bottom figure shows the "V" component, positive towards the North and negative towards the South.

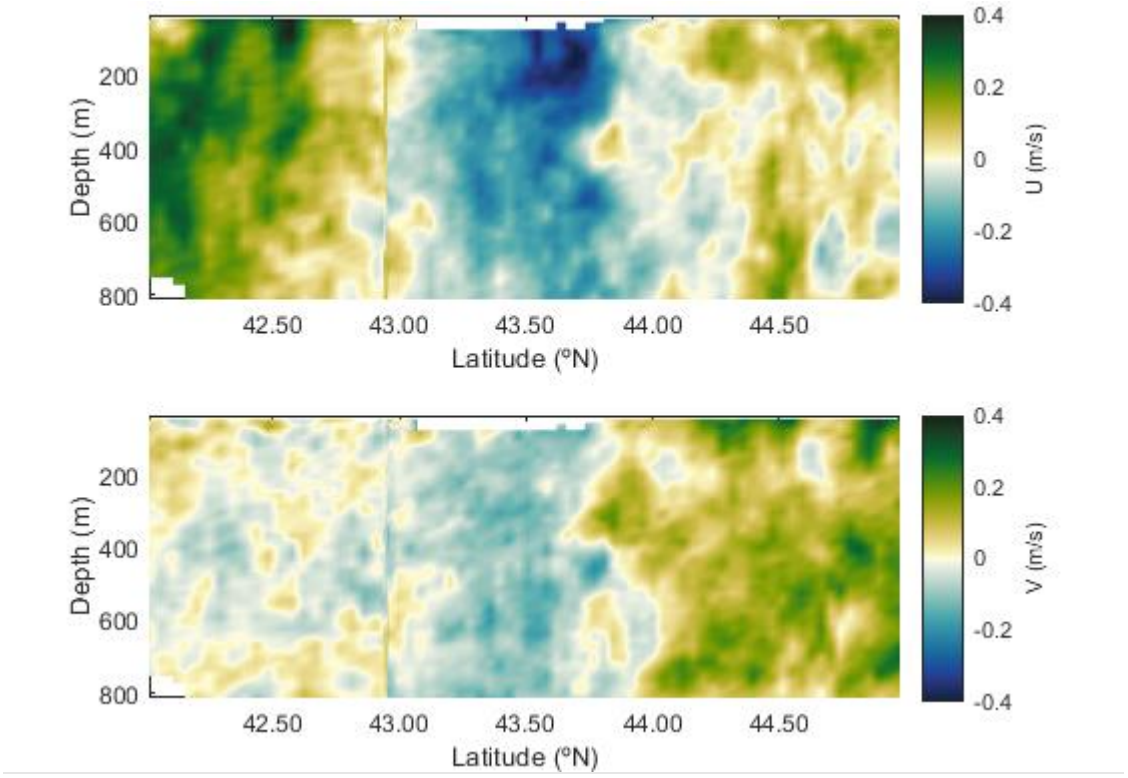

Figure 4.17 – Current velocity measurements obtained aboard the R/V Knorr (cruise KN207-03) from the hull-mounted ADCP along latitude, centred around the location of station 12. The top figure shows the "U" component, positive towards the East and negative towards the West. The bottom figure shows the "V" component, positive towards the North and negative towards the South.

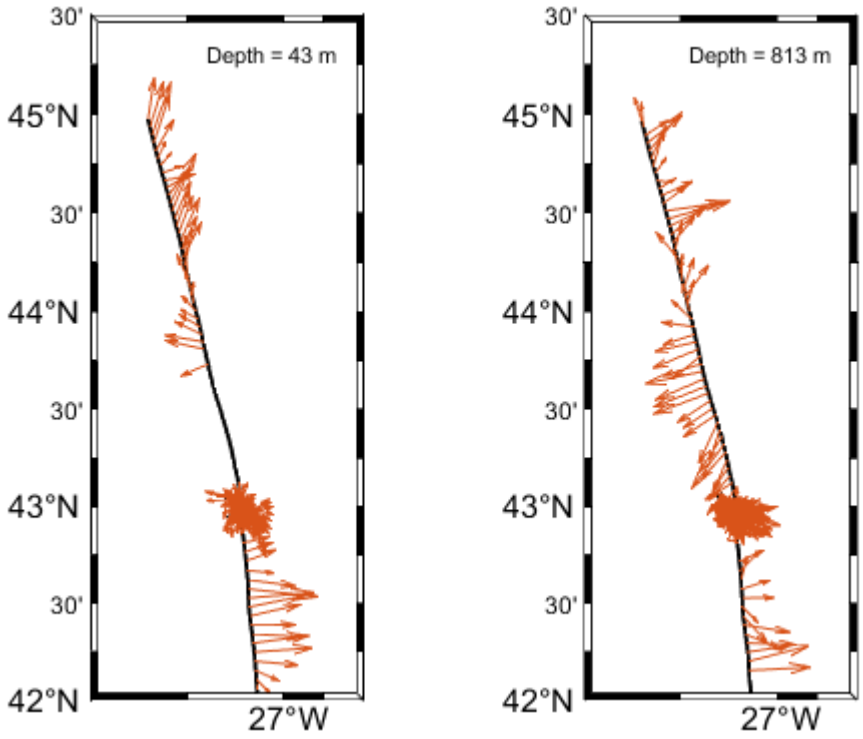

Figure 4.18 - Cruise KN207-03's track with vectorial arrows representing the direction and intensity of the current velocity from the hull-mounted ADCP, centred around station 12. The left figure represents the first depth layer at 43 m and the right figure represents the last depth layer at 813 m, after processing.

4.3. Altimetry

Maps of SLA were created for the position of profiles 4 and 12 due to the interest in the eddies present at these locations. The paths and history of these eddies were further analysed. Figure 4.19 shows the altimetry map for June 16th, 2012, the day of profile 4. In the two days that passed between profiles 4 and 12, there were almost no changes in the SLA, so this figure is representative of both profiles. The image shows a positive anomaly of 0.15 m in SLA at the location of profile 4 and a negative anomaly of -0.1 m at the location of profile 12. The signal of the anomaly along with the direction of the geostrophic currents (clockwise for profile 4 and anticlockwise for profile 12) represent the presence of an anticyclone at the location of profile 4 and a cyclone at the location of profile 12.

The values of the geostrophic current velocity can be seen in Figure 4.20. The image confirms that the changes seen in the ADCP data were due to vorticity. At profile 4, the cruise passed very close to the centre of the anticyclone (see Figure 4.13) from south to north, which explains the strong westward current followed by a strong eastward current separated by a no-motion

zone. At the location of profile 12, the cruise passed by a cyclonic eddy, which also validates the change in the current direction from the ADCP. This image shows that both eddies have azimuthal speeds between 0.20 m s^{-1} and 0.35 m s^{-1}, with the strongest geostrophic current velocities located in the interface between them.

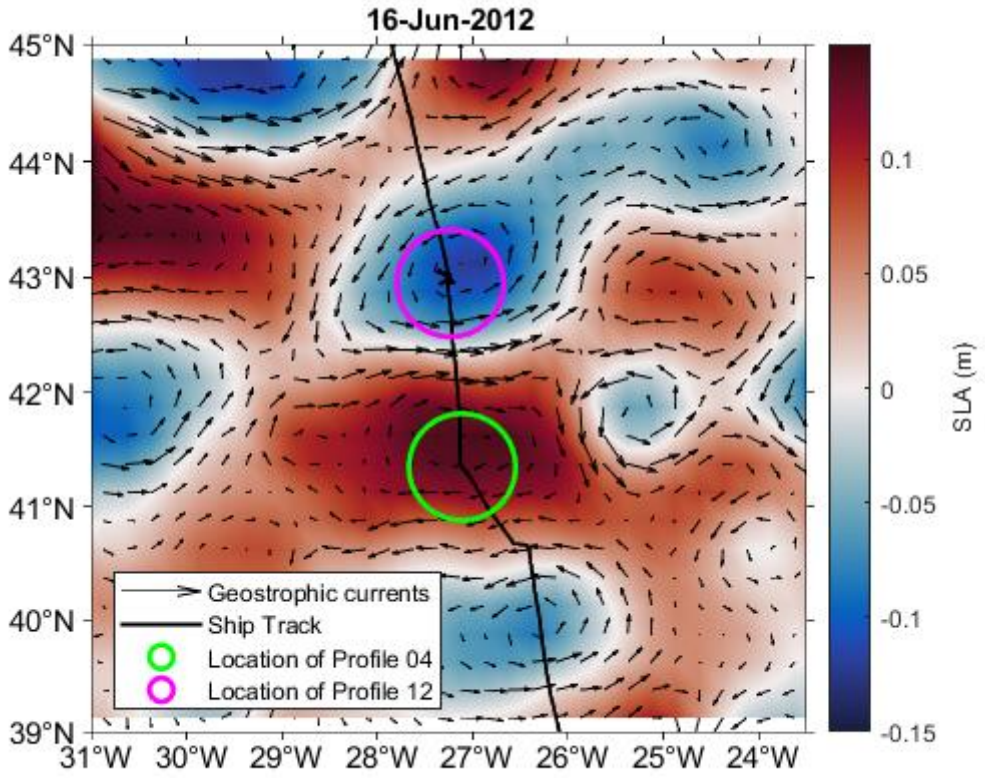

Figure 4.19 – Sea Level Anomaly (SLA) map (https://doi.org/10.48670/moi-00148) for the 16th of June 2012. Black arrows represent the geostrophic current velocities. The solid line represents the cruise KN207-03's track, and the green and purple circles represent the location of stations 4 and 12 respectively.

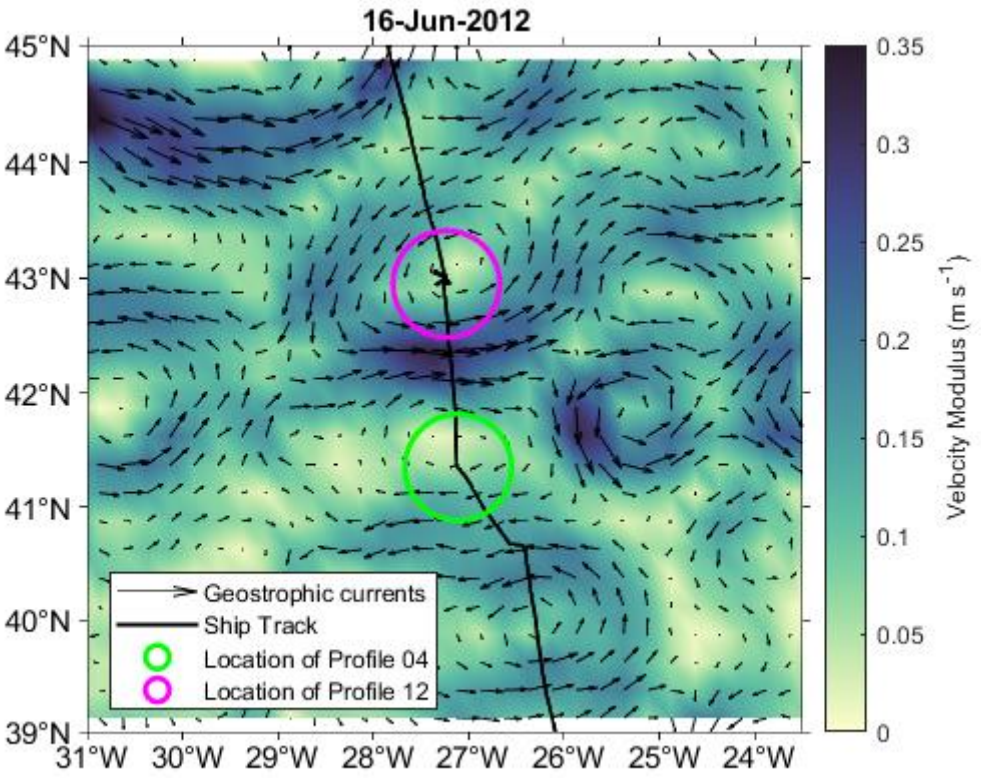

Figure 4.20 – Velocity modulus map (https://doi.org/10.48670/moi-00148) for the 16th of June 2012. Black arrows represent the geostrophic current velocities. The solid line represents the cruise KN207-03's track, and the green and purple circles represent the location of stations 4 and 12 respectively.

After running the *SimpleEddyDetection* algorithm, both eddies were identified (Figure 4.21). The anticyclone was detected with an amplitude of 6 cm and a radius of 100 km. At that time, the cyclone seemed to be merging with another smaller cyclone to the northeast. The algorithm detected both eddies as one with a radius of 115 km and an amplitude of 9.2 cm. If we consider the larger cyclone by itself, its radius is 70 km, and its amplitude is 6.2 cm.

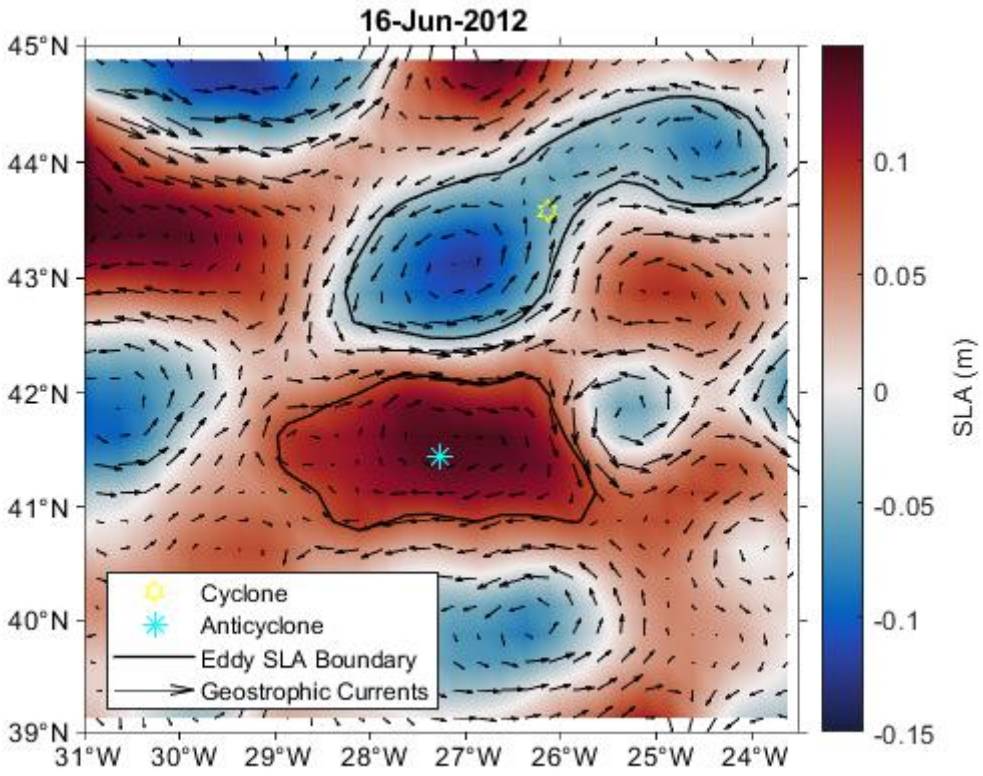

Figure 4.21 – Sea Level Anomaly (SLA) (https://doi.org/10.48670/moi-00148) map for the 16th of June 2012. Black arrows represent the geostrophic current velocities. The solid lines represent the boundary of the eddies SLA signal detected by the algorithm. The yellow star represents the central position of the cyclonic eddy's boundary, and the blue star represents the central position of the anticyclonic eddy's boundary.

The anticyclone's history was tracked by following its path backwards and forward in time using the SLA maps. In total, 4.5 years of SLA were analysed tracing the anticyclone's origin three years and two months before its discovery, on the 16th of June 2012, and its end nine months after this date, with a total lifespan of three years and eleven months. During this time, the anticyclone travelled 1273 km, resulting in an average velocity of 0.89 km d^{-1} (0.0103 m s^{-1}), in a southwestwardly direction. The SLA maps prior to April 2009, show that this anticyclone was the result of a merging event between two other anticyclonic eddies. After March 2013, the signal of the anticyclone became too weak to be identified by the detection algorithm. Without *in situ* data to analyse the eddy signals before and after the anticyclone it is not possible to track it further. Although it is not possible to show the full path of the anticyclone due to the density of images, four (Figures 4.22 to 4.25) were selected representing it during interleaved phases of its life. Figures 4.22 and 4.25 represent the first and last time the anticyclone was detected by the algorithm. Figures 4.23 and 4.24 represent two equally

distributed phases of the anticyclone's life. The analysis of the maps dating prior to Figure 4.22 shows that the eddies that merged into the anticyclone originated off the Goban Spur and Porcupine Seabight (Figure 2.1). After its formation, the anticyclone travelled south and then east close to the Charcot Seamounts. From September 2009 to February 2010, it stayed stationary. From February 2010 to April 2011, it travelled at a constant speed headed southwest, after which it turned northwest subsequently becoming stationary from August 2011 to January 2012. By February 2012, it reached the Azores plateau where it slowed down. As the anticyclone was "climbing" the plateau, its heading changed to the northwest, and once it got on the plateau it headed southwest as it faded away. Figure 4.23 shows an interesting interaction between three anticyclonic eddies, including the anticyclone from profile 4, where they were all meridionally aligned.

The amplitudes registered by the detection algorithm, compared to the value from when the anticyclone was found, were higher after its formation, 9.4 cm, and lower before its dissipation, 4.9 cm. The same relation is seen in the radius values with 110 km after its formation and 91 km before its dissipation. However, on the 15th of August 2010, the meddy's amplitude and radius was 8.7 cm and 59 km, respectively, while on the 15th of December 2011, was 5.7 cm and 57 km, respectively. For the interpretation of these values, it is important to consider that the algorithm makes these computations based on enclosed contours. When a contour covers more than one eddy (i.e.: during a merging event) this affects the actual values of the eddies. Such might be the case for the first and last amplitude/radius registered.

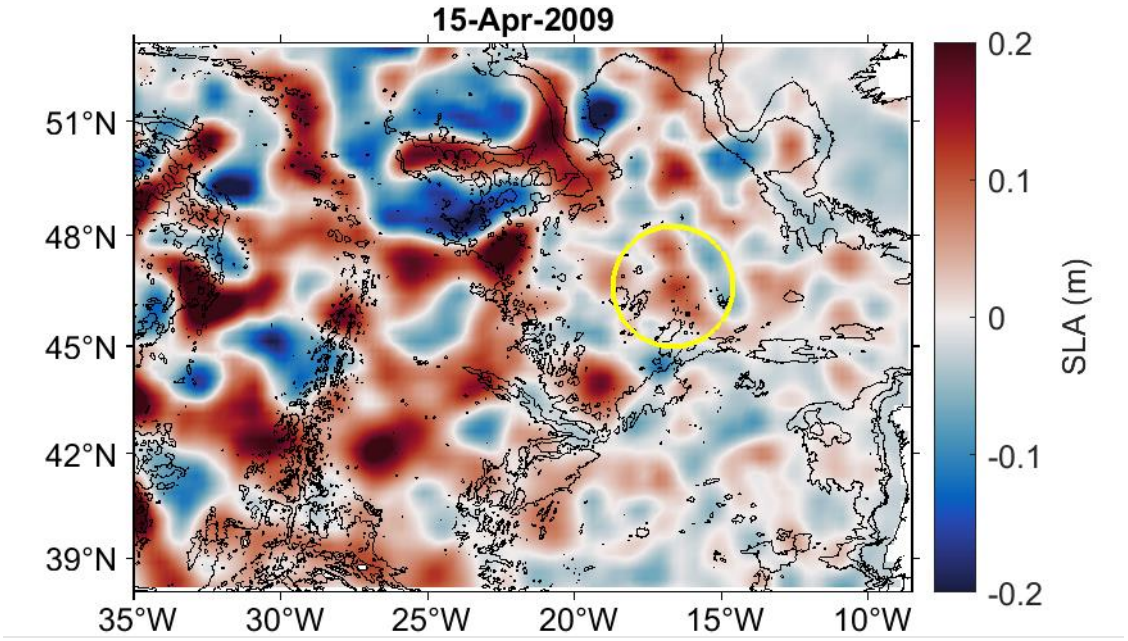

Figure 4.22 – Sea Level Anomaly (SLA) map (https://doi.org/10.48670/moi-00148) for the 15th of April 2009. The solid lines represent the bathymetry contours from 0 – -3000 m depth with 1000 m interval. The yellow circle represents the location of the anticyclone SLA peak amplitude.

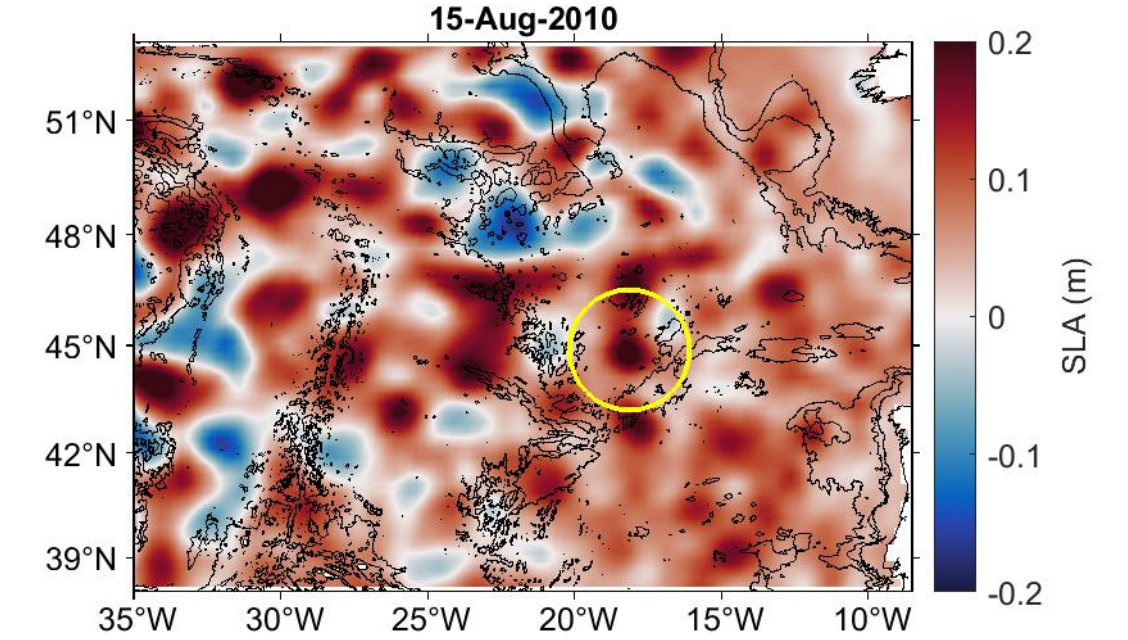

Figure 4.23 – Sea Level Anomaly (SLA) map (https://doi.org/10.48670/moi-00148) for the 15th of August 2010. The solid lines represent the bathymetry contours from 0 – -3000 m depth with 1000 m interval. The yellow circle represents the location of the anticyclone SLA peak amplitude.

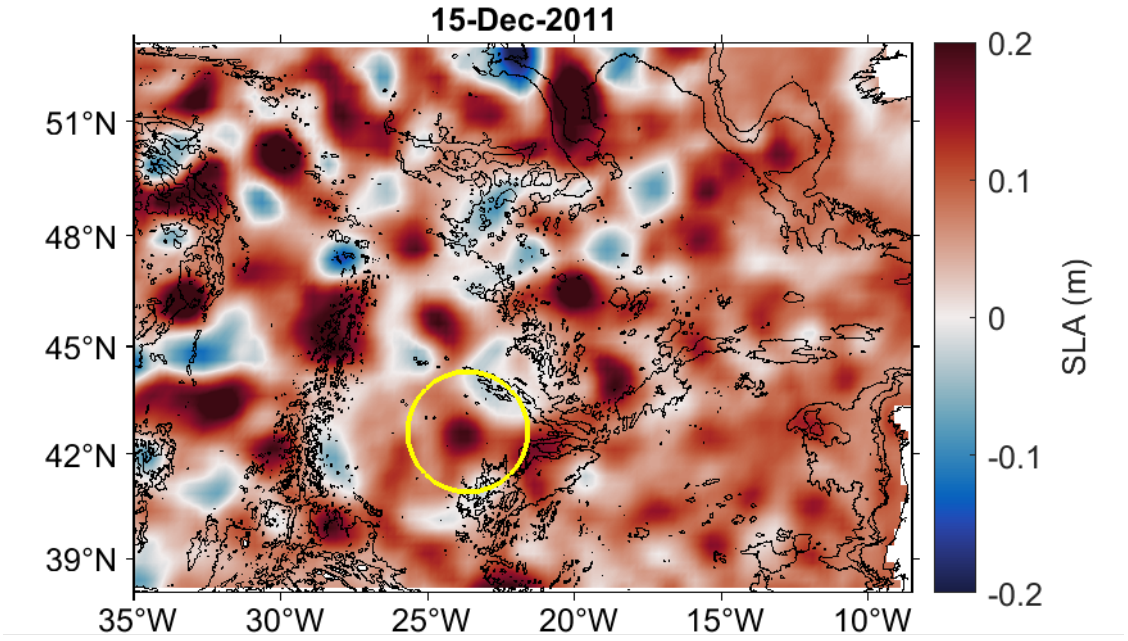

Figure 4.24 – Sea Level Anomaly (SLA) map (https://doi.org/10.48670/moi-00148) for the 15th of December 2011. The solid lines represent the bathymetry contours from 0 – -3000 m depth with 1000 m interval. The yellow circle represents the location of the anticyclone SLA peak amplitude.

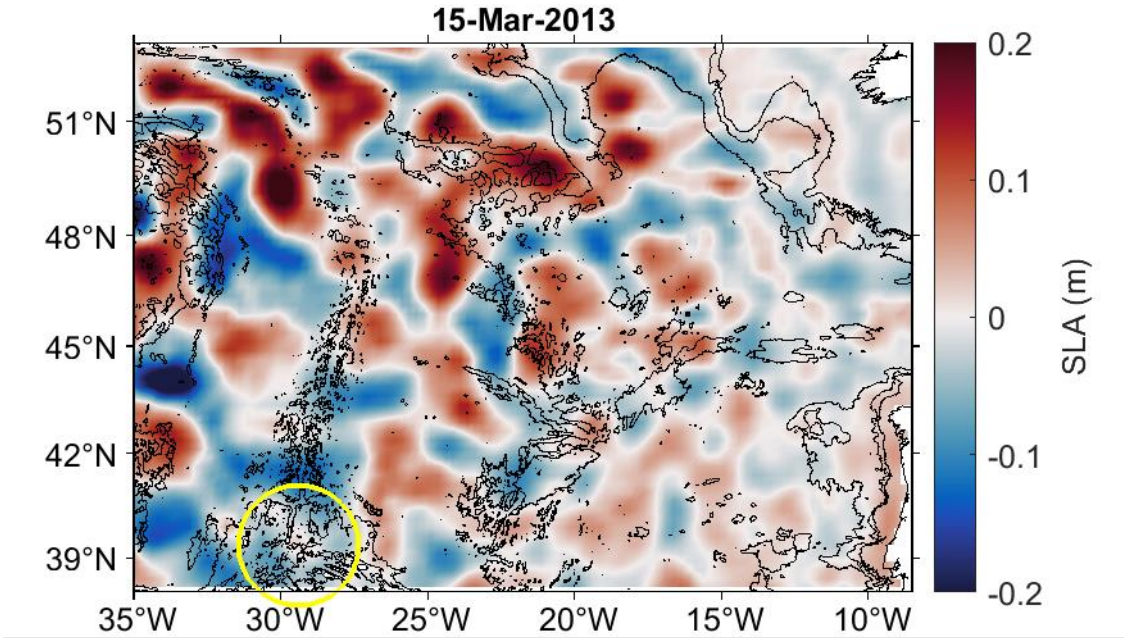

Figure 4.25 – Sea Level Anomaly (SLA) map (https://doi.org/10.48670/moi-00148) for the 15th of March 2013. The solid lines represent the bathymetry contours from 0 – -3000 m depth with 1000 m interval. The yellow circle represents the location of the anticyclone SLA peak amplitude.

4.4. Ocean Colour (OC)

After inspecting the days of the cruise, the 17th of June 2012 (day 169 of the Julian calendar in leap years), showed the best data with the least interference from clouds. This date will be used as a reference to all OC images to be analysed for the time of the cruise.

Figure 4.26 shows that at 41º N and between 28 – 26º W, there is an increase in SST reaching 17.5º C. Between 42.5 – 44º N and 28.5 – 26.5º W, there seems to be a decrease in temperature relative to its surroundings with values between 15.6 – 16.4º C. Overall, the figure shows a high thermal region between 40.6 – 42.3º N and 30.4 – 25.7º W. The gradient of temperature decreasing with latitude is also observable, with a strong thermal front at 42.5º N.

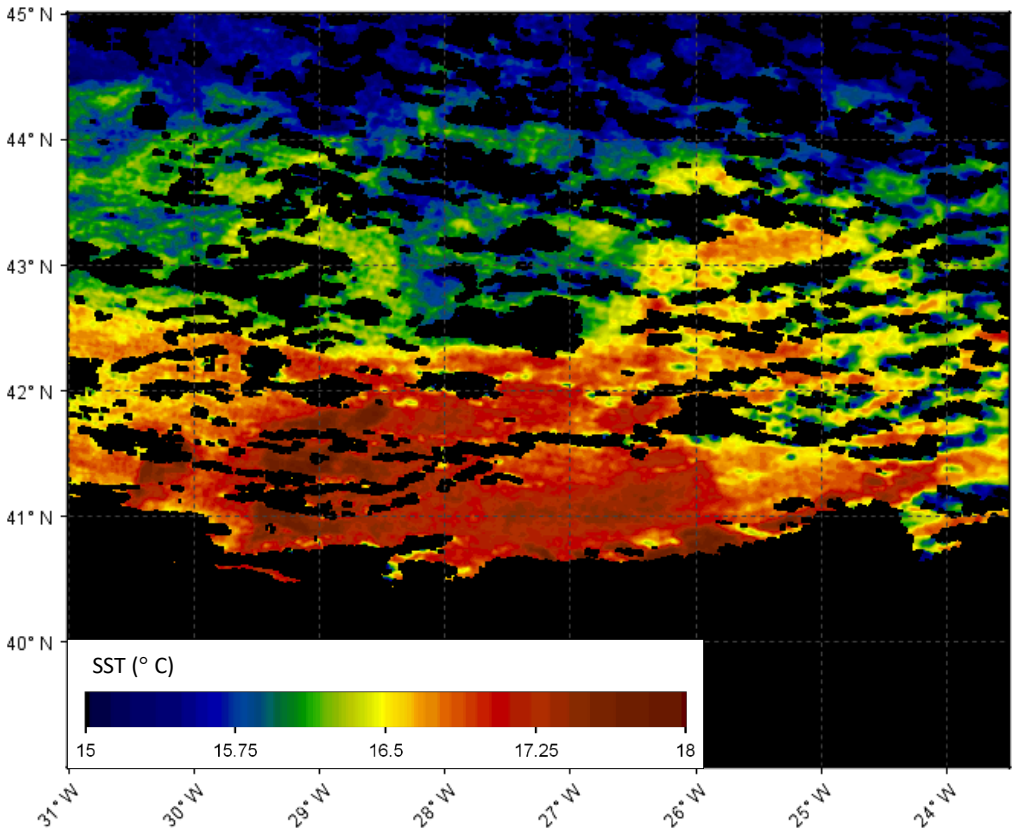

Figure 4.26 – MODIS - Aqua derived Sea Surface Temperature (SST), 4 µm (nighttime) image with 1 km resolution from Canopus, for the 17th of June 2012.

Figure 4.27 shows the Chlor-a concentration for the region of interest. This figure shows a decrease in Chlor-a concentration centred at 42º N and between 28 – 27º W, with values as low as 0.05 mg m^{-3}. Further north, the presence of the cyclonic eddy is related to an increase in Chlor-a concentration, up to 0.6 mg m^{-3}, which connects the two cyclones identified by the algorithm (Figure 4.21). Between the cyclone and the anticyclone, there is a Chlor-a front, in the corresponding region of strong geostrophic currents (Figure 4.20) coinciding with the upper limit of a structure located between 41.5 – 42.5º N and with an eastern boundary at approximately 26º W.

The kd_490 coefficient (Figure 4.28) shows an increase in attenuation above both eddies (cyclone and anticyclone). This increase in kd_490 is higher in the cyclone, reaching 0.10 m^{-1}, while the maximum value above the anticyclone is 0.05 m^{-1}.

The POC concentration (Figure 4.29) shows an increase above the cyclonic eddy with values reaching 130 mg m^{-3}. At the location of the anticyclone, the POC concentration is on average 60 mg m^{-3}. Much like the previous figures, between the eddies, there is a front where POC concentration increases by 30 mg m^{-3} in a short distance.

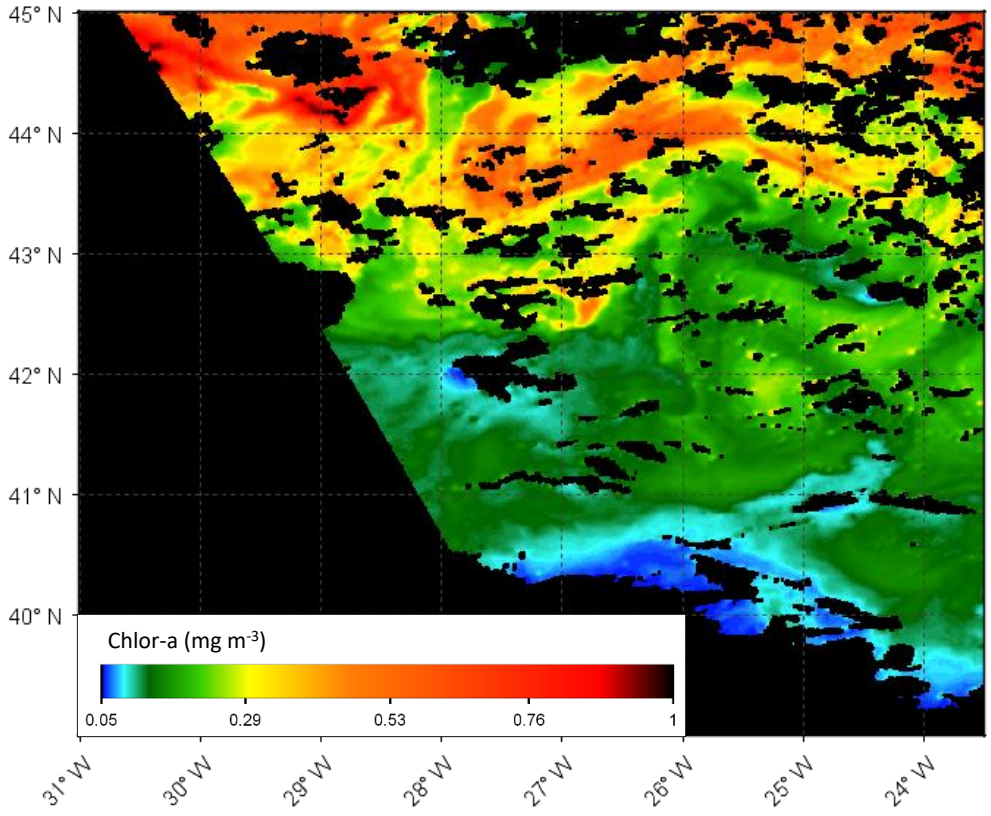

Figure 4.27 – MODIS - Aqua derived Chlorophyll-a concentrations (Chlor-a, in mg m^{-3}) image with 1 km resolution from Canopus, for the 17th of June 2012.

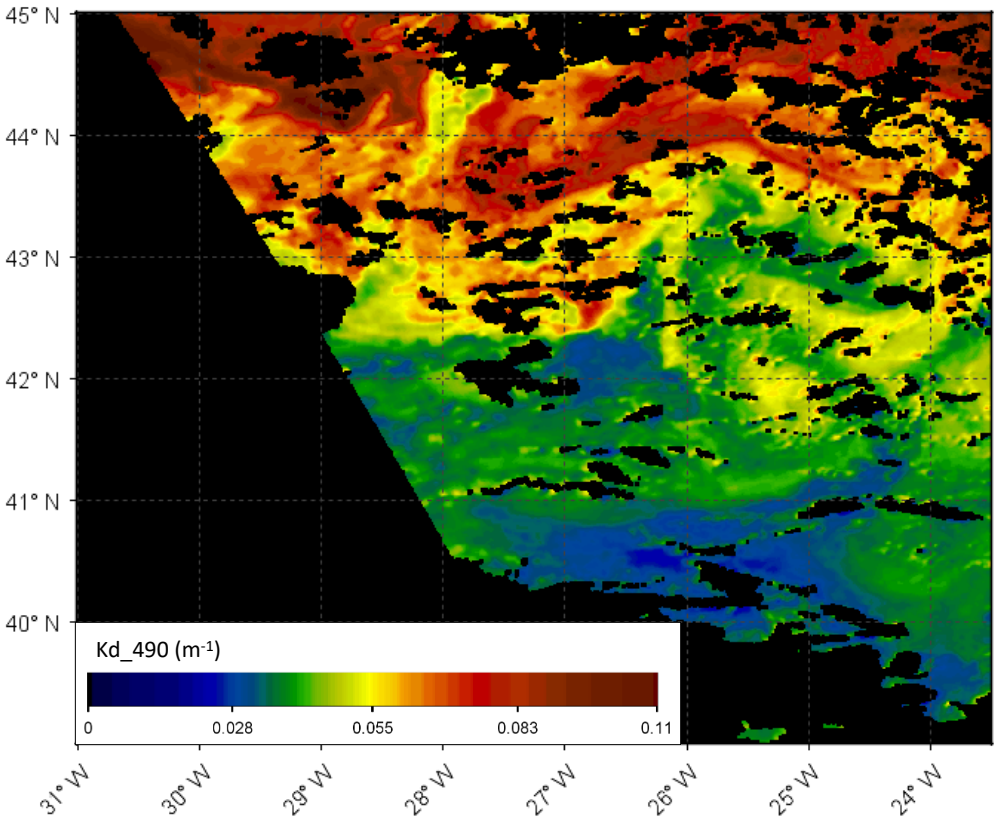

Figure 4.28 – MODIS - Aqua derived Diffuse Attenuation Coefficient at 490 nm (kd_490, in m^{-1}) image with 1 km resolution from Canopus, for the 17th of June 2012.

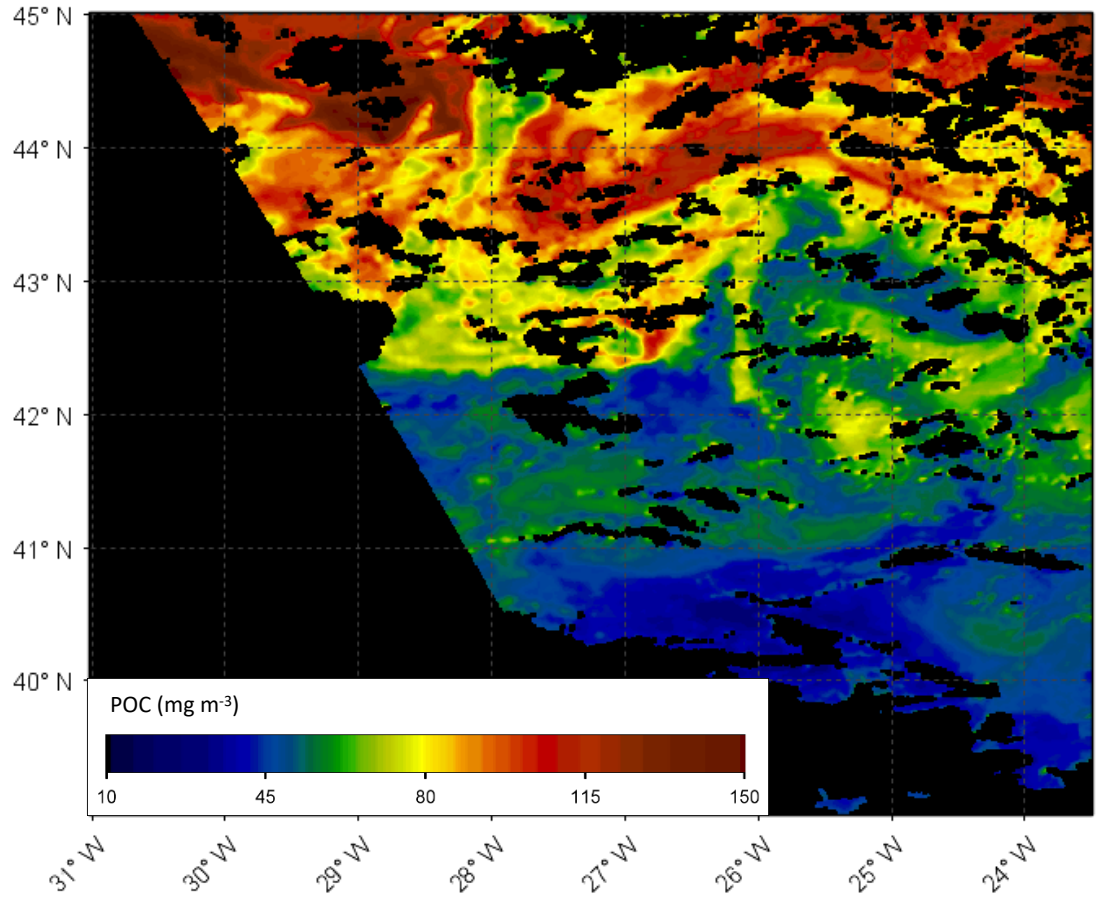

Figure 4.29 – MODIS - Aqua derived Particulate Organic Carbon (POC, in mg m^{-3}) image with 1 km resolution from Canopus, for the 17th of June 2012.

Figure 4.30 shows the PIC concentrations for the area of interest. These concentrations increase in the same region identified in Figure 4.27 as a Chlor-a minimum centred at 42º N and between 28 – 27 º W, at least 0.001 mol m^{-3}. There is also an increase in PIC at the border between the two eddies with values reaching 0.0008 mol m^{-3}. At the centre of the cyclone, there seems to be also an increase in PIC of smaller magnitude, with mean values of 0.0005 mol m^{-3}.

The PAR (Figure 4.31) does not seem to be influenced by the presence of the eddies. As expected, it presents a high correlation with latitude.

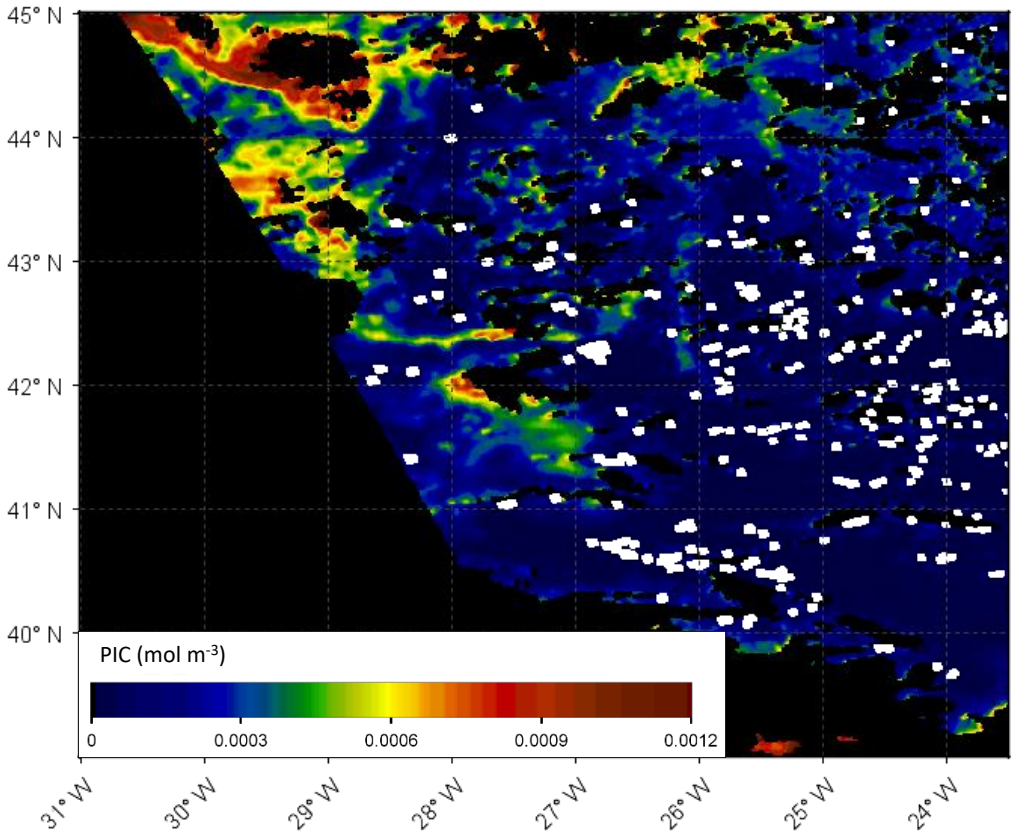

Figure 4.30 – MODIS - Aqua derived Particulate Inorganic Carbon (PIC, in mol m^{-3}) image with 1 km resolution from Canopus, for the 17th of June 2012.

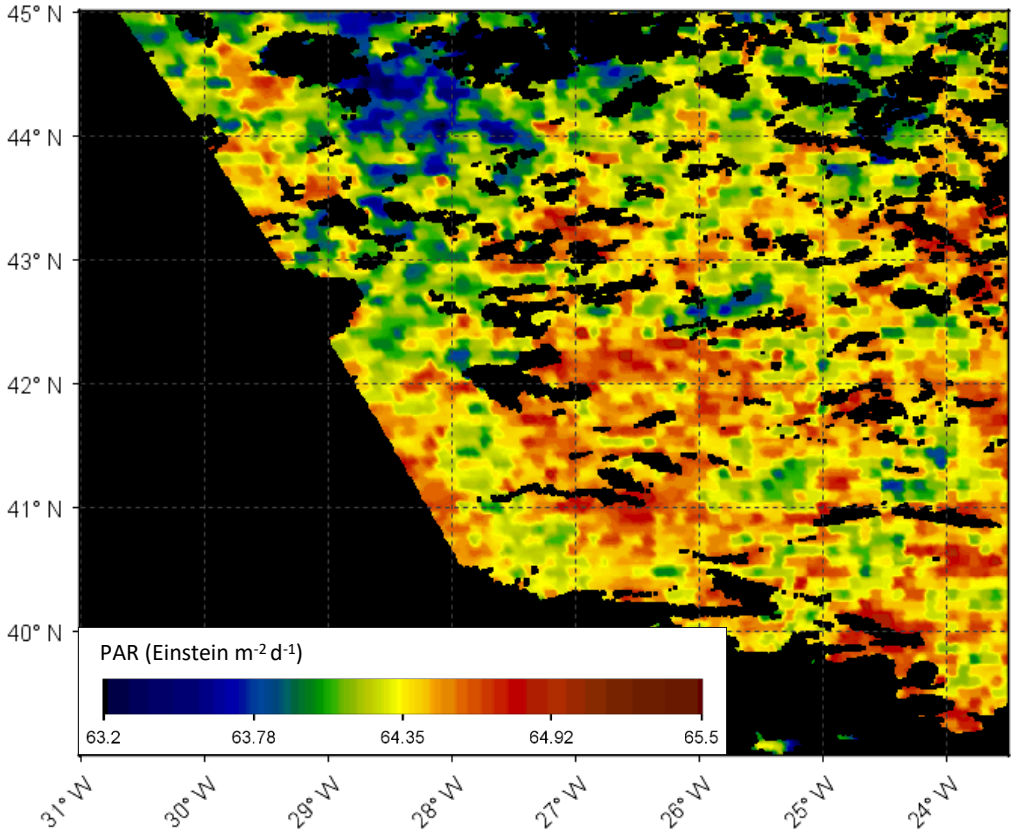

Figure 4.31 – MODIS – Aqua derived Photosynthetic Active Radiation (PAR, in Einstein m^{-2} d^{-1}) image with 1 km resolution from Canopus, for the 17th of June 2012.

5. Discussion

To identify whether there were meddies present in any of the stations from NA-VICE cruise, temperature and salinity profiles were plotted and compared with known WMs using a T-S diagram (Figure 4.2). This revealed that profiles 4 and 12 showed characteristics of MW between 1060-1300 m and 750-900 m, respectively. Since the presence of MW characteristics is not enough to reach a conclusion, Richardson and Bashmachnikov's criteria were tested using MEDTRANS climatology (Appendixes IV and V) through which salinity and temperature anomalies of over 0.2 and 2 ºC, respectively, were computed for profile 4 between 700 – 1300 m depth. These values verify the presence of a meddy at station 4 according to the literature. The anomalies computed for profile 12 failed these criteria, although characteristics of MW were found. This could reveal the interaction between the meddy and a shallower eddy (with its core at approximately 860 m), where properties at its boundary are being transferred to the latter and stored in its core (Richardson *et al*., 2000). The evidence is also seen in the O – S and

T-O diagrams (Figures 4.5 and 4.6) where these stations overlap within the range of MW characteristics, in inverse proportionality between those properties. The results show that the density in profile 4 (Figure 4.4) is much lower compared to the remaining profiles in the depth range of the meddy structure, which is a consequence of the increase in temperature inside its core. An oxygen minimum is observed at 1000 m (Figure 4.4), the lowest in this dataset, which, along with a higher salinity (Figure 4.1), indicates that the meddy core should be between 970 – 1050 m (Brogueira *et al*., 2004). Although the results show that the meddy's influence in the water column is strong up to 600 m, the main structure is located between 800 – 1400 m as shown in the Brunt-Väisälä frequency squared. The meddy is not clear in the salinity and temperature fields represented in Figures 4.9 and 4.10, since no lens structure is observed. However, its effect is detected in the isohalines and isotherms, which become almost vertical. Meanwhile, a lens-shaped structure is visible in the oxygen and Brunt-Väisälä frequency sections (Figures 4.11 and 4.12) centred at 1000 m depth, and it is possible to detect a connection between this structure and a second shallower lens centred at 500 m and stretching northward. This corroborates the hypothesis of the interaction between the meddy and a shallower structure.

The ADCP data shows that the cruise crossed an anticyclonic structure, very close to its centre (Figure 4.13), around station 4, with velocities at 800 m depth higher than at 40 m (Figure 4.15). This indicates that the core of the structure is below 800 m (the maximum range of the ADCP). These results highlight the meddy's presence corroborating the CTD data and proving that the meddy's expression is felt throughout the water column until the surface, as initially deduced by Käse & Zenk (1987). The data around station 12 shows a cyclonic structure with higher expression in the first 300 m depth (Figures 4.16 and 4.18), whose influence affects at least the first 500 m of the water column (Figure 4.17). This structure is responsible for trapping a WM with MW characteristics at shallower depths, most likely transferred from the nearby meddy.

The presence of the meddy and the cyclonic eddy is also evidenced through their surface expression in the SLA maps (Figure 4.19). These maps validate the ADCP results showing the cruise track passing near the SLA peak value of each structure where the azimuthal velocity is smaller (Figure 4.20), and the geostrophic currents direction coinciding with the vector arrows of the ADCP. These maps also show that besides the interaction with the meddy, the cyclonic eddy interacts with another cyclone (Figure 4.21). The southwestward trajectory described by the meddy agrees with the descriptions given by other authors (Richardson *et al*., 1991) as well as the average translation velocity. The velocity was computed by dividing the distance between

the first and last known position of the meddy with the travel time between them, but since the meddy was stationary for long periods of time, its actual translation velocity was higher than the calculated. All of the meddy's main physical properties are depicted in Table 5.1., where they are compared with known values from the literature. There seems to be a link between the meddy trajectory and the plotted bathymetry contours, which could be causing it to become stationary.

Its trajectory implies that most likely the meddy was formed at either the Goban Spur or the Porcupine Seabight (Figre 2.1). Although not confirmed, these spots have been reported before as possible meddy generation sites by Shoosmith *et al*. (2005). The idea of meddies being formed in the north is relatively recent since most reports before 2000 referred to them as meddy-like structures, and even recent articles do not mention meddy generation sites further north than Cape Finisterre or Cape Ortega, which is inconsistent with the presence of meddies north of 43º N, and assuming their predominant trajectory is westward/southwestward (Richardson *et al*., 1991, 2000; Bashmachnikov *et al*., 2015a). Indeed, Bashmachnikov *et al*. (2015a) could not explain the increase in the number of meddies at the western tip of Galicia Bank. Thanks to numerical modelling, a high number of meddy structures have been identified as far as 45º N (Ienna *et al*., 2022) even though few direct observations have been made (i.e.: Paillet *et al*., 1999). The reason for such uncertainty is the fact that as the MOW flows northward, it interacts with ambient water exchanging properties, hence the characteristics of the MOW south of the Iberian Peninsula are different from its characteristics to the north (Mauritzen *et al*., 2001; Ambar *et al*., 2002). Assuming the meddy formation mechanisms are the same in all of the identified generation sites, the core properties of the meddy will depend on the characteristics of the MOW at the site. This means that southern meddies will be easier to identify, especially further from the coast, because of their stronger salinity and temperature anomalies (Bashmachnikov *et al*., 2015a). Nonetheless, northern meddies, even if formed at the Irish continental shelf where MOW characteristics are much weaker, play an important role in the transport of heat and salt (probably even other properties as well as fauna) in the North Atlantic Ocean, thus being relevant for the study of meddies physical and biogeochemical properties.

Table 5.1.: Comparative table showing the range of known meddy parameters compiled from several authors (Richardson *et al*., 1991, 2000; Bashmachnikov 2015a; Ienna *et al*., 2022) and the values of the meddy detected during the NA-VICE expedition. For the salinity and temperature anomalies as well as for the azimuthal velocity and Sea Level Anomaly (SLA), the maximum values registered were used.

	Values From Literature	**NA-VICE Meddy**
Salinity Anomaly	0.2 – 1	0.24
Temperature Anomaly	0.5 – 4 ºC	2.18 ºC
Azimuthal Velocity	0.10 – 0.50 m s^{-1}	0.35 m s^{-1}
Translation Velocity	0.01 – 0.05 m s^{-1}	0.01 m s^{-1}
Radius	10 – 150 km	100 km
SLA	0.05 – 0.20 m	0.15 m
Lifetime	1 – 5 years	3.9 years

Contrary to the discoveries by Bashmachnikov *et al*. (2013) and according to the description of Oliveira *et al*. (2000), the SST showed an increase in temperature associated with the meddy core, and north of it a decrease in temperature above the cyclone. This validates the hypothesis that meddies present a surface signal characteristic of anticyclonic eddies. However, it does not disprove Bashmachnikov's theory that during their formation, meddies can trap colder water at the centre of their surface vorticity field, which becomes surrounded by warmer SST. This theory could also be a consequence of their formation site, with influence from phenomena, i.e., upwelling, localized on western coasts. Perhaps one of this work's most significant contributions is the first attempt to describe meddies' biogeochemical properties using remote sensing OC. The results show that this meddy can be observed in terms of Chlor-a, kd_490, POC, and PIC, but no apparent signal was found in PAR. An inverse proportionality described by previous authors (Yadav *et al*., 2019) between SST and Chlor-a is observed, as well as a correlation between Chlor-a and kd_490. Additionally, Chlor-a, kd_490, and POC images showed remarkably similar patterns, which means that in these open ocean areas we are in the presence of Case 1 waters, that is, water whose optical properties are determined primarily by phytoplankton and co-varying Coloured Dissolved Organic Matter (CDOM) and detritus degradation products (Gordon & Morel, 1983; Morel, 1988). Magalhães-Loureiro (2022) reported the same relationship for the Azores region and some adjacent areas in the NE Atlantic. The increase of SST combined with a decrease of Chlor-a associated with anticyclonic vortices

indicates downwelling. This could also mean that the aggregation of biological material, such as POC accumulating above the meddy is most likely being pumped down to deeper layers. If a conclusion is reached that meddies can act as sinking mechanisms for POC, their climatic role is more significant than anticipated, acting as a biological pump for storing carbon in the deeper ocean. Another interesting observation was the increase in PIC concentrations. Being a proxy for calcium carbonate produced by shell organisms, in particular for the species *Emiliania huxleyi*, a coccolithophore found in almost all ocean ecosystems from the equator to sub-polar regions (Mitchell *et al*., 2017). This implies that meddies can also act as aggregation and transportation mechanisms for these species.

6. Conclusions and Final Considerations

The NA-VICE expedition took place during summer 2012 from Azores to Iceland, aboard the R/V Knorr (cruise). This study used a combination of NA-VICE *in situ* data (CTD and ADCP) and remote sensing data (altimetry – SLA, geostrophic currents; SST; and OC – Chlor-a, PIC, POC, kd_490, and PAR) to identify and successfully describe the physical properties of a meddy north of the Azores region. It was also possible to recreate the meddy´s path in the NE Atlantic and to infer that this meddy was formed in the Goban Spur/Porcupine Seabight area. Answering a question posed by Richardson *et al*. (2000), the results of this study strongly suggest that the northern meddy-like structures can be classified as meddies and should be considered for the salt and heat budget transport of the Mediterranean. Furthermore, the cyclonic structures with MW characteristics should also be considered given their contribution to this budget. Following the work of Bashmachnikov *et al*. (2015a), a new classification for meddies should be created not only considering the generation site and pathways, but also combining the meddies' core properties with the location of the MOW where those properties can be found.

By integrating OC imagery in this work, it was possible to infer some optical properties of the near-surface waters around the meddies structures, contributing in this way, to the topic of meddies' biogeochemical implications in the open ocean.

Future works should further analyse meddies' OC near-surface expression, preferably combined with *in situ* biological samples, to clarify some of the questions left unanswered: Do meddies act as biological pumps sequestering carbon into the deeper ocean? Can they act as pools of calcium carbonate shell organisms and transport them through oligotrophic oceans?

Finally, understanding the fundamental role of the meddies in the North Atlantic Ocean is complex and challenging. Therefore, it is only through joint efforts from diverse oceanography fields (e.g., physical, biological, chemical, and geological) and multiple data (*in situ* and remote sensing) that we will be able to fully grasp the origin, pathways, properties, and influence of meddies in the Atlantic Ocean.

7. References

Alonso-González, I. J., Arístegui, J., Vilas, J. C., & Hernández-Guerra, A. (2009). Lateral POC transport and consumption in surface and deep waters of the Canary Current region: A box model study. Global Biogeochemical Cycles, 23(2), 1–12. https://doi.org/10.1029/2008GB003185

Ambar, I., Serra, N., Brogueira, M. J., Cabeçadas, G., Abrantes, F., Freitas, P., Gonçalves, C., & Gonzalez, N. (2002). Physical, chemical and sedimentological aspects of the Mediterranean outflow off Iberia. Deep-Sea Research Part II: Topical Studies in Oceanography, 49(19), 4163–4177. https://doi.org/10.1016/S0967-0645(02)00148-0

Ambar, I., Serra, N., Neves, F., & Ferreira, T. (2008). Observations of the Mediterranean Undercurrent and eddies in the Gulf of Cadiz during 2001. Journal of Marine Systems, 71(1–2), 195–220. https://doi.org/10.1016/j.jmarsys.2007.07.003

Arhan, M., Colin De Verdiére, A., & Mémery, L. (1994). The Eastern Boundary of the Subtropical North Atlantic. Journal of Physical Oceanography, 24(6), 1295–1316. https://doi.org/10.1175/1520-0485(1994)024<1295:TEBOTS>2.0.CO;2

Armi, L., Hebert, D., Oakey, N., Price, J. F., Richardson, P. L., Rossby, H. T., & Ruddick, B. (1989). Two Years in the Life of a Mediterranean Salt Lens. Journal of Physical Oceanography, 19(3), 354–370. https://doi.org/10.1175/1520-0485(1989)019<0354:TYITLO>2.0.CO;2

Armi, L., & Stommel, H. (1983). Four Views of a Portion of the North Atlantic Subtropical Gyre. Journal of Physical Oceanography, 13(5), 828–857. https://doi.org/10.1175/1520-0485(1983)013<0828:FVOAPO>2.0.CO;2

Armi, L., & Zenk, W. (1984). Large Lenses of Highly Saline Mediterranean Water. Journal of Physical Oceanography, 14(10), 1560–1576. https://doi.org/10.1175/1520-0485(1984)014<1560:LLOHSM>2.0.CO;2

Balmaseda, M. A., Trenberth, K. E., & Källén, E. (2013). Distinctive climate signals in reanalysis of global ocean heat content. Geophysical Research Letters, 40(9), 1754–1759. https://doi.org/10.1002/grl.50382

Barbosa Aguiar, A. C., Peliz, Á., & Carton, X. (2013). A census of Meddies in a long-term high-resolution simulation. Progress in Oceanography, 116, 80–94. https://doi.org/10.1016/j.pocean.2013.06.016

Bashmachnikov, I., Boutov, D., & Dias, J. (2013). Manifestation of two meddies in altimetry

and sea-surface temperature. Ocean Science, 9(2), 249–259. https://doi.org/10.5194/os-9-249-2013

Bashmachnikov, I., Machín, F., Mendonça, A., & Martins, A. (2009b). In situ and remote sensing signature of meddies east of the mid-Atlantic ridge. Journal of Geophysical Research: Oceans, 114(5), 1–16. https://doi.org/10.1029/2008JC005032

Bashmachnikov, I., Mohn, C., Pelegrí, J. L., Martins, A., Jose, F., Machín, F., & White, M. (2009a). Interaction of Mediterranean water eddies with Sedlo and Seine Seamounts, Subtropical Northeast Atlantic. Deep-Sea Research Part II: Topical Studies in Oceanography, 56(25), 2593–2605. https://doi.org/10.1016/j.dsr2.2008.12.036

Bashmachnikov, I., Neves, F., Calheiros, T., & Carton, X. (2015a). Properties and pathways of Mediterranean water eddies in the Atlantic. Progress in Oceanography, 137, 149–172. https://doi.org/10.1016/j.pocean.2015.06.001

Bashmachnikov, I., Neves, F., Nascimento, Medeiros, J., Ambar, I., Dias, J., & Carton, X. (2015b). Temperature-salinity distribution in the northeastern Atlantic from ship and Argo vertical casts. Ocean Science, 11(2), 215–236. https://doi.org/10.5194/os-11-215-2015

Biescas, B., Sallarès, V., Pelegrí, J. L., Machín, F., Carbonell, R., Buffett, G., Dañobeitia, J. J., & Calahorrano, A. (2008). Imaging meddy finestructure using multichannel seismic reflection data. Geophysical Research Letters, 35(11), 1–5. https://doi.org/10.1029/2008GL033971

Bower, A. S., Le Cann, B., Rossby, T., Zenk, W., Gould, J., Speer, K., Richardson, P. L., Prater, M. D., & Zhang, H. M. (2002). Directly measured mid-depth circulation in the northeastern North Atlantic Ocean. Nature, 419(6907), 603–607. https://doi.org/10.1038/nature01078

Bower, Amy S., Armi, L., & Ambar, I. (1995). Direct evidence of meddy formation off the southwestern coast of Portugal. Deep-Sea Research Part I, 42(9), 1621–1630. https://doi.org/10.1016/0967-0637(95)00045-8

Bower, Amy S., Armi, L., & Ambar, I. (1997). Lagrangian observations of meddy formation during a mediterranean undercurrent seeding experiment. Journal of Physical Oceanography, 27(12), 2545–2575. https://doi.org/10.1175/1520-0485(1997)027<2545:LOOMFD>2.0.CO;2

Brogueira, M. J., Cabeçadas, G., & Gonçalves, C. (2004). Chemical resolution of a meddy emerging off southern Portugal. Continental Shelf Research, 24(15), 1651–1657. https://doi.org/10.1016/j.csr.2004.05.012

Carton, X., Chérubin, L., Paillet, J., Morel, Y., Serpette, A., & Le Cann, B. (2002). Meddy coupling with a deep cyclone in the Gulf of Cadiz. Journal of Marine Systems, 32(1–3), 13–42. https://doi.org/10.1016/S0924-7963(02)00028-3

Ciani, D., Carton, X., Barbosa Aguiar, A. C., Peliz, A., Bashmachnikov, I., Ienna, F., Chapron, B., & Santoleri, R. (2017). Surface signature of Mediterranean water eddies in a long-term high-resolution simulation. Deep-Sea Research Part I: Oceanographic Research Papers, 130(March), 12–29. https://doi.org/10.1016/j.dsr.2017.10.001

Daniault, N., Mazé, J. P., & Arhan, M. (1994). Circulation and mixing of Mediterranean water west of the Iberian Peninsula. Deep-Sea Research Part I, 41(11–12), 1685–1714. https://doi.org/10.1016/0967-0637(94)90068-X

De Graciansky, P. C., & Poag, C. W. (1985). Geologic history of Goban Spur, northwest Europe continental margin. Initial Reports DSDP, Leg 80, Brest to Southampton. Part 2, 1187–1216. https://doi.org/10.2973/dsdp.proc.80.158.1985

De Pascual-Collar, Á., Sotillo, M. G., Levier, B., Aznar, R., Lorente, P., Amo-Baladrón, A., & Álvarez-Fanjul, E. (2019). Regional circulation patterns of Mediterranean Outflow Water near the Iberian and African continental slopes. Ocean Science, 15(3), 565–582. https://doi.org/10.5194/os-15-565-2019

Dushaw, B. D., Gaillard, F., & Terre, T. (2017). Acoustic Tomography in the Canary Basin: Meddies and Tides. Journal of Geophysical Research: Oceans, 122(11), 8983–9003. https://doi.org/10.1002/2017JC013356

Frazão, H. C., Prien, R. D., Müller, T. J., Schulz-Bull, D. E., & Waniek, J. J. (2021). 30 years of temporal variability of temperature and currents below the main thermocline between 1980–2009 in the subtropical Northeast Atlantic (Kiel 276, 33∘N, 22∘W). Journal of Marine Systems, 217(February). https://doi.org/10.1016/j.jmarsys.2021.103517

Gasser, M., Pelegrí, J. L., Emelianov, M., Bruno, M., Gràcia, E., Pastor, M., Peters, H., Rodríguez-Santana, Á., Salvador, J., & Sánchez-Leal, R. F. (2017). Tracking the Mediterranean outflow in the Gulf of Cadiz. Progress in Oceanography, 157, 47–71. https://doi.org/10.1016/j.pocean.2017.05.015

Gordon, H. R. & Morel, A. (1983). Remote Assessment of Ocean Color for Interpretation of Satellite Visible Imagery: A Review. Lecture Notes on Coastal and Estuarine Studies, vol. 4, Springer-Verlag.

Hogg, N. G., & Stommel, H. M. (1990). How currents in the upper thermocline could advect meddies deeper down. Deep-Sea Research, 37(4), 613–623.

Hummon, J. M., & Firing, E. (2003). A direct comparison of two RDI shipboard ADCPs: A 75-kHz ocean surveyor and a 150-kHz narrow band. Journal of Atmospheric and Oceanic Technology, 20(6), 872–888. https://doi.org/10.1175/1520-0426(2003)020<0872:ADCOTR>2.0.CO;2

Ienna, F., Bashmachnikov, I., & Dias, J. (2022). Meddies and Their Sea Surface Expressions: Observations and Theory. Journal of Physical Oceanography, 52(11), 2643–2656. https://doi.org/10.1175/JPO-D-22-0081.1

Ienna, F., Jo, Y. H., & Yan, X. H. (2014). A new method for tracking meddies by satellite altimetry. Journal of Atmospheric and Oceanic Technology, 31(6), 1434–1445. https://doi.org/10.1175/JTECH-D-13-00080.1

Iorga, M. C., & Lozier, M. S. (1999a). Signatures of the Mediterranean outflow from a North Atlantic climatology 1. Salinity and density fields. Journal of Geophysical Research: Oceans, 104(C11), 25985–26009. https://doi.org/10.1029/1999jc900115

Iorga, M. C., & Lozier, M. S. (1999b). Signatures of the Mediterranean outflow from a North Atlantic climatology 2. Diagnostic velocity fields. Journal of Geophysical Research: Oceans, 104(C11), 26011–26029. https://agupubs.onlinelibrary.wiley.com/doi/pdf/10.1029/1999JC900204

Jungclaus, J. H. (1999). A three-dimensional simulation of the formation of anticyclonic lenses (meddies) by the instability of an intermediate depth boundary current. Journal of Physical Oceanography, 29(7), 1579–1598. https://doi.org/10.1175/1520-

0485(1999)029<1579:ATDSOT>2.0.CO;2

Käse, R. H., & Zenk, W. (1987). Reconstructed Mediterranean Salt Lens Trajectories. Journal of Physical Oceanography, 17(1), 158–163. https://doi.org/10.1175/1520-0485(1987)017<0158:RMSLT>2.0.CO;2

Klemas, V., & Yan, X. H. (2014). Subsurface and deeper ocean remote sensing from satellites: An overview and new results. Progress in Oceanography, 122, 1–9. https://doi.org/10.1016/j.pocean.2013.11.010

Liu, M., & Tanhua, T. (2021). Water masses in the Atlantic Ocean: Characteristics and distributions. Ocean Science, 17(2), 463–486. https://doi.org/10.5194/os-17-463-2021

Lozier, S. M., Bower, A. S., Furey, H. H., Drouin, K. L., Xu, X., & Zou, S. (2022). Overflow water pathways in the North Atlantic. *Progress in Oceanography, 208*(August), 102874. https://doi.org/10.1016/j.pocean.2022.102874

Maas, L. R. M., & Zahariev, K. (1996). An exact, stratified model of a meddy. Dynamics of Atmospheres and Oceans, 24(1–4), 215–225. https://doi.org/10.1016/0377-0265(95)00451-3

Magalhães-Loureiro, C. (2022). Azores Oceanic Microbes: Understanding the Structure and Dynamics of Microbial Communities at Various Ocean Space and Timescales [Doctoral dissertation, University of Azores].

Marques, F. O., Catalão, J. C., DeMets, C., Costa, A. C. G., & Hildenbrand, A. (2013). GPS and tectonic evidence for a diffuse plate boundary at the Azores Triple Junction. Earth and Planetary Science Letters, 381, 177–187. https://doi.org/10.1016/j.epsl.2013.08.051

Mauritzen, C., Morel, Y., & Paillet, J. (2001). On the influence of Mediterranean Water on the Central Waters of the North Atlantic Ocean. Deep-Sea Research Part I: Oceanographic Research Papers, 48(2), 347–381. https://doi.org/10.1016/S0967-0637(00)00043-1

McDougall, T. J., & Barker, P. M. (2011). Getting started with TEOS-10 and the Gibbs Seawater (GSW) Oceanographic Toolbox (p. 28).

McDougall, T. J., Jackett, D. R., Millero, F. J., Pawlowicz, R., & Barker, P. M. (2012). A global algorithm for estimating Absolute Salinity. Ocean Science, 8(6), 1123–1134. https://doi.org/10.5194/os-8-1123-2012

McDowell, S. E., & Rossby, H. T. (1978). Mediterranean water: An intense mesoscale eddy off the Bahamas. Science, 202(4372), 1085–1087. https://doi.org/10.1126/science.202.4372.1085

McWilliams, J. C. (1984). The emergence of isolated coherent vortices in turbulent flow. Journal of Fluid Mechanics, 146, 21–43. https://doi.org/doi:10.1017/S0022112084001750

Mitchell, C., Hu, C., Bowler, B., Drapeau, D., & Balch, W. M. (2017). Estimating Particulate Inorganic Carbon Concentrations of the Global Ocean From Ocean Color Measurements Using a Reflectance Difference Approach. Journal of Geophysical Research: Oceans, 122(11), 8707–8720. https://doi.org/10.1002/2017JC013146

Morel, A. (1988). Optical modeling of the upper ocean in relation to its biogenous matter content (case 1 waters). Journal of Geophysical Research, 93(C9), 10749-10768.

Ochoa, J., & Bray, N. A. (1991). Water mass exchange in the Gulf of Cadiz. Deep Sea Research Part A. Oceanographic Research Papers, 38, S465–S503. https://doi.org/10.1016/s0198-

0149(12)80021-5

Oliveira, P. B., Serra, N., Fiúza, A. F. G., & Ambar, I. (2000). Chapter 7 A study of meddies using simultaneous in-situ and satellite observations. Elsevier Oceanography Series, 63(C), 125–148. https://doi.org/10.1016/S0422-9894(00)80008-2

Paillet, J., Le Cann, B., Serpette, A., Morel, Y., & Carton, X. (1999). Real-time tracking of a galician Meddy. Geophysical Research Letters, 26(13), 1877–1880. https://doi.org/10.1029/1999GL900378

Pickard, G. L., & Emery, W. J. (1982). Descriptive Physical Oceanography: An Introduction (Fourth (SI) enlarged edition). Pergamon Press.

Piip, A. T. (1969). Large Cells of Mediterranean Water in the Madeira-Canaries Region. EOS (Transactions American Geophysical Union), 50, pp. (193).

Pingree, R. D., & Le Cann, B. (1993a). A shallow meddy (a smeddy) from the Secondary Mediterranean Salinity Maximum. Journal of Geophysical Research, 98(C11). https://doi.org/10.1029/93jc02211

Pingree, R. D., & Le Cann, B. (1993b). Structure of a meddy (Bobby 92) southeast of the Azores. Deep-Sea Research I, 40(10), 2077–2103.

Pinheiro, L. M., Song, H., Ruddick, B., Dubert, J., Ambar, I., Mustafa, K., & Bezerra, R. (2010). Detailed 2-D imaging of the Mediterranean outflow and meddies off W Iberia from multichannel seismic data. Journal of Marine Systems, 79(1–2), 89–100. https://doi.org/10.1016/j.jmarsys.2009.07.004

Pires, A. C. (2013). Modeling the Western Iberian Margincirculation: present and future [Doctoral dissertation, University of Aveiro]. http://hdl.handle.net/10773/12191

Prater, M. D., & Sanford, T. B. (1994). A Meddy off Cape St. Vincent. Part I : Description. Journal of Physical Oceanography (Vol. 24, pp. 1572–1586).

Richardson, P. L., Bower, A. S., & Zenk, W. (2000). A census of Meddies tracked by floats. Progress in Oceanography, 45(2), 209–250. https://doi.org/10.1016/S0079-6611(99)00053-1

Richardson, P. L., McCartney, M. S., & Maillard, C. (1991). A search for meddies in historical data. Dynamics of Atmospheres and Oceans, 15(3–5), 241–265. https://doi.org/10.1016/0377-0265(91)90022-8

Richardson, P. L., Price, J. F., Walsh, D., Armi, L., & Schröder, M. (1989). Tracking Three Meddies with SOFAR Floats. Journal of Physical Oceanography, 19(3), 371–383. https://doi.org/10.1175/1520-0485(1989)019<0371:TTMWSF>2.0.CO;2

Richardson, Philip L., & Tychensky, A. (1998). Meddy trajectories in the Canary Basin measured during the SEMAPHORE experiment, 1993-1995. Journal of Geophysical Research: Oceans, 103(C11), 25029–25045. https://doi.org/10.1029/97JC02579

Savenkoff, C., Lefevre, D., Denis, M., & Lambert, C. E. (1993). How do microbial communities keep living in the Mediterranean outflow within northeast Atlantic intermediate waters? Deep-Sea Research Part II, 40(1–2), 627–641. https://doi.org/10.1016/0967-0645(93)90036-M

Serra, N., Sadoux, S., Ambar, I., & Renouard, D. (2002). Observations and laboratory modeling of meddy generation at Cape St. Vincent. Journal of Physical Oceanography, 32(1), 3–25.

https://doi.org/10.1175/1520-0485(2002)032<0003:OALMOM>2.0.CO;2

Serra, Nuno, & Ambar, I. (2002). Eddy generation in the Mediterranean undercurrent. Deep-Sea Research Part II: Topical Studies in Oceanography, 49(19), 4225–4243. https://doi.org/10.1016/S0967-0645(02)00152-2

Shoosmith, D. R., Richardson, P. L., Bower, A. S., & Rossby, H. T. (2005). Discrete eddies in the northern North Atlantic as observed by looping RAFOS floats. *Deep-Sea Research Part II: Topical Studies in Oceanography, 52*(3–4), 627–650. https://doi.org/10.1016/j.dsr2.2004.12.011

Spiegel, M. R. (1988). *Schaum's Outline of Theory and Problems of Statistics (Schaum's Outline series - second edition)*. McGraw-Hill Publishing Company.

Stammer, D., Hinrichsen, H. H., & Kase, R. H. (1991). Can meddies be detected by satellite altimetry? *Journal of Geophysical Research, 96*(C4), 7005–7014. https://doi.org/10.1029/90JC02740

Swallow, J. C. (1969). A Deep Eddy Off Cape St Vincent. *Deep-Sea Research, Supplement*, 285–295.

Tomczak, M. (1999). Some historical, theoretical and applied aspects of quantitative water mass analysis. *Journal of Marine Research, 57*(2), 275–303. https://doi.org/10.1357/002224099321618227

Tozer, B., Sandwell, D. T., Smith, W. H. F., Olson, C., Beale, J. R., & Wessel, P. (2019). Global Bathymetry and Topography at 15 Arc Sec: SRTM15+. *Earth and Space Science, 6*(10), 1847–1864. https://doi.org/10.1029/2019EA000658

Wang, Z. F., Sun, L., Li, Q. Y., & Cheng, H. (2019). Two typical merging events of oceanic mesoscale anticyclonic eddies. *Ocean Science, 15*(6), 1545–1559. https://doi.org/10.5194/os-15-1545-2019

Wienberg, C., Wintersteller, P., Beuck, L., & Hebbeln, D. (2013). Coral patch seamount (NE Atlantic) - A sedimentological and megafaunal reconnaissance based on video and hydroacoustic surveys. *Biogeosciences, 10*(5), 3421–3443. https://doi.org/10.5194/bg-10-3421-2013

Xu, C. (2020, September 7). *SimpleEddyDetection*. GitHub. https://github.com/chouj/SimpleEddyDetection

Yadav, V. K., Jahageerdar, S., & Adinarayana, J. (2019). Validation of chlorophyll-a and sea surface temperature concentration and their relationship with the parameters diffuse attenuation coefficient and photosynthetically active radiation using MODIS data: A case study of Gujarat coastal region. *Indian Journal of Geo-Marine Sciences, 48*(9), 1370–1376.

Appendixes

Appendix I – Vertical profiles of Conservative Temperature (CT) and Absolute Salinity (SA) according to the Thermodynamic Equation of Seawater – 2010 (TEOS-10). The profiles represent the seven selected stations from the cruise KN207-03.

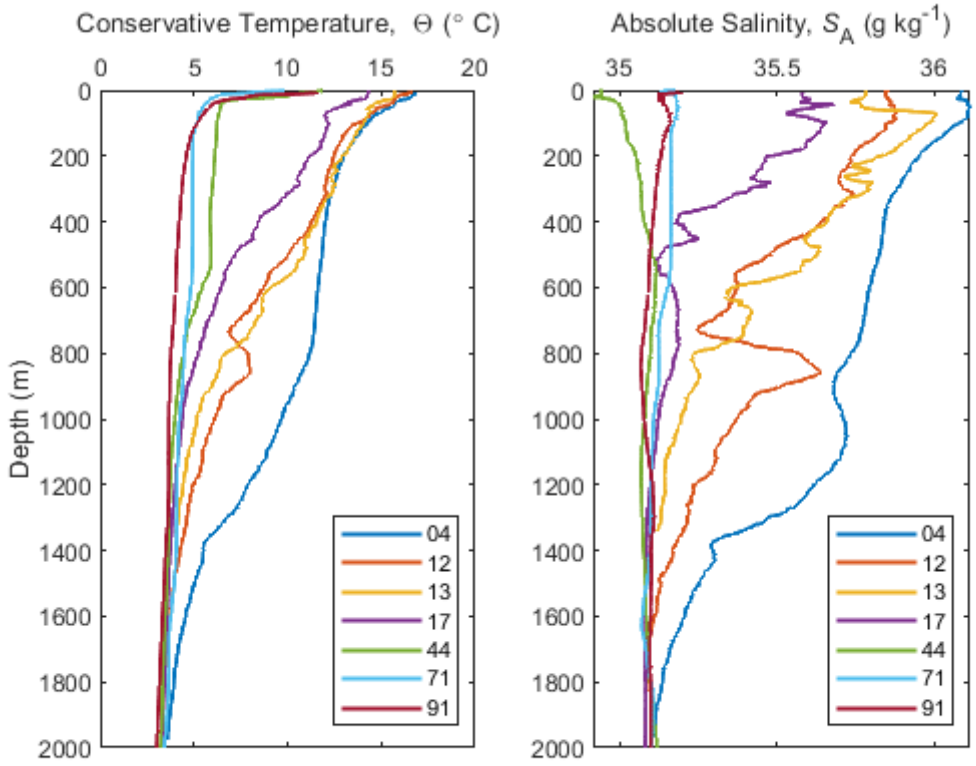

Appendix II – Temperature-Salinity (T-S) diagram showing the location of known Water Masses (WM) from the North Atlantic in terms of salinity, temperature, and density. The identified WMs are NACW (North Atlantic Central Water), MW (Mediterranean Water), SAIW (South Arctic Intermediate Water, NADW (North Atlantic Deep Water) and LSW (Labrador Sea Water). The parameters from each WM were retrieved from Magalhães-Loureiro (2022). The density was computed with a pressure reference of 10.1325 dbar, absolute pressure at sea level (McDougall & Barker, 2011).

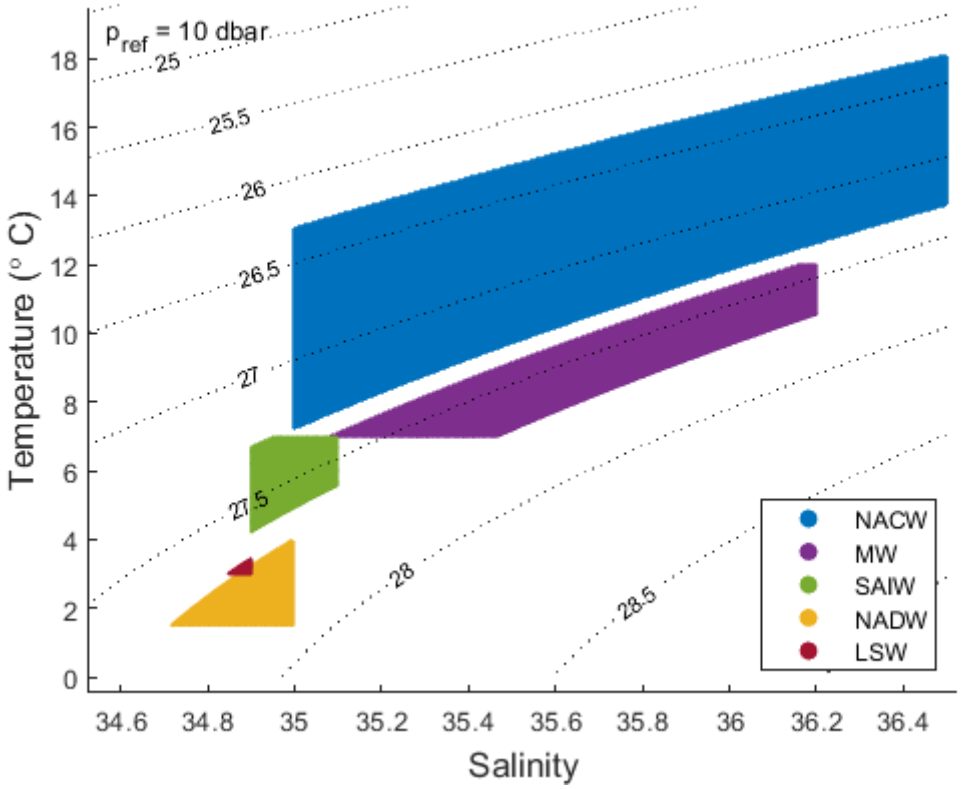

Appendix III – Sea Level Anomaly (SLA) formal mapping error. Data obtained from https://doi.org/10.48670/moi-00148.

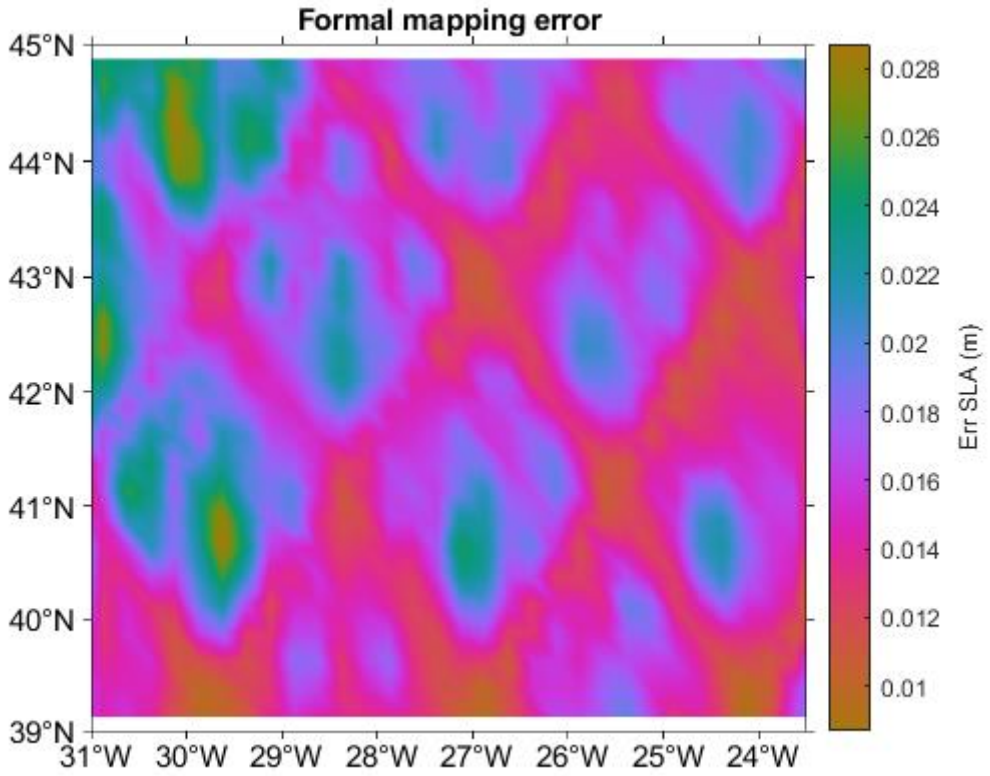

Appendix IV – MEDTRANS Practical Salinity (SP) fields for 700 m, 800 m, 900 m, 1000 m, 1100 m, 1200 m, 1300 m, and 1400 m depth. Dataset obtained from https://www.mare-centre.pt/en/research/data-library/medtrans-data (Bashmachnikov *et al*., 2015b).

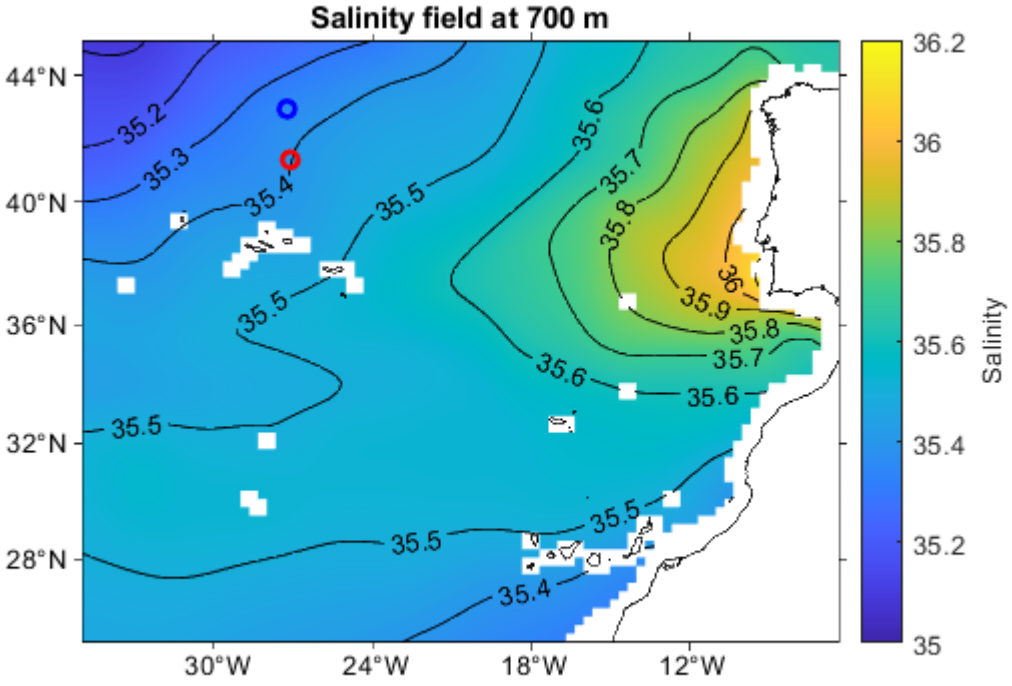

Appendix IV – MEDTRANS Practical Salinity (SP) fields for 700 m, 800 m, 900 m, 1000 m, 1100 m, 1200 m, 1300 m, and 1400 m depth. Dataset obtained from https://www.mare-centre.pt/en/research/data-library/medtrans-data (Bashmachnikov *et al*., 2015b). (cont.)

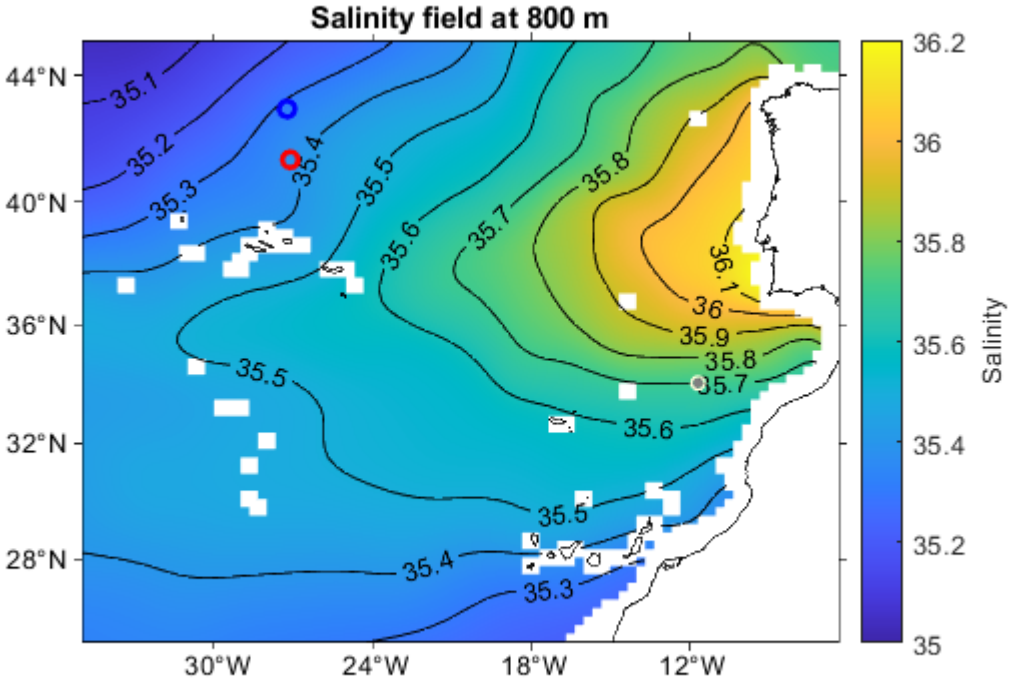

Appendix IV – MEDTRANS Practical Salinity (SP) fields for 700 m, 800 m, 900 m, 1000 m, 1100 m, 1200 m, 1300 m, and 1400 m depth. Dataset obtained from https://www.mare-centre.pt/en/research/data-library/medtrans-data (Bashmachnikov *et al*., 2015b). (cont.)

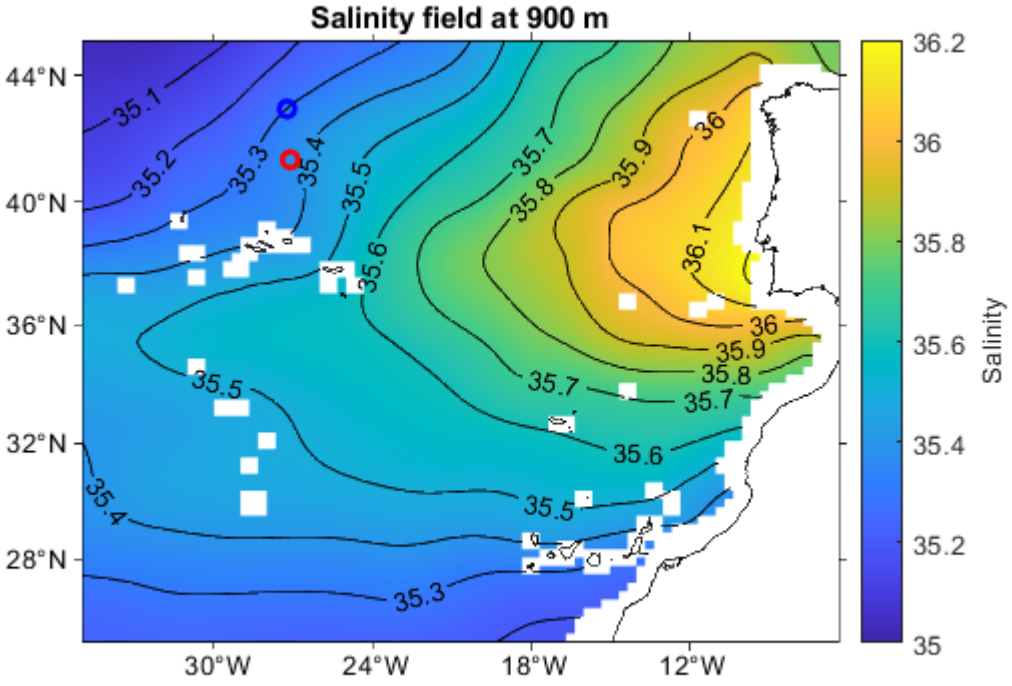

Appendix IV – MEDTRANS Practical Salinity (SP) fields for 700 m, 800 m, 900 m, 1000 m, 1100 m, 1200 m, 1300 m, and 1400 m depth. Dataset obtained from https://www.mare-centre.pt/en/research/data-library/medtrans-data (Bashmachnikov *et al*., 2015b). (cont.)

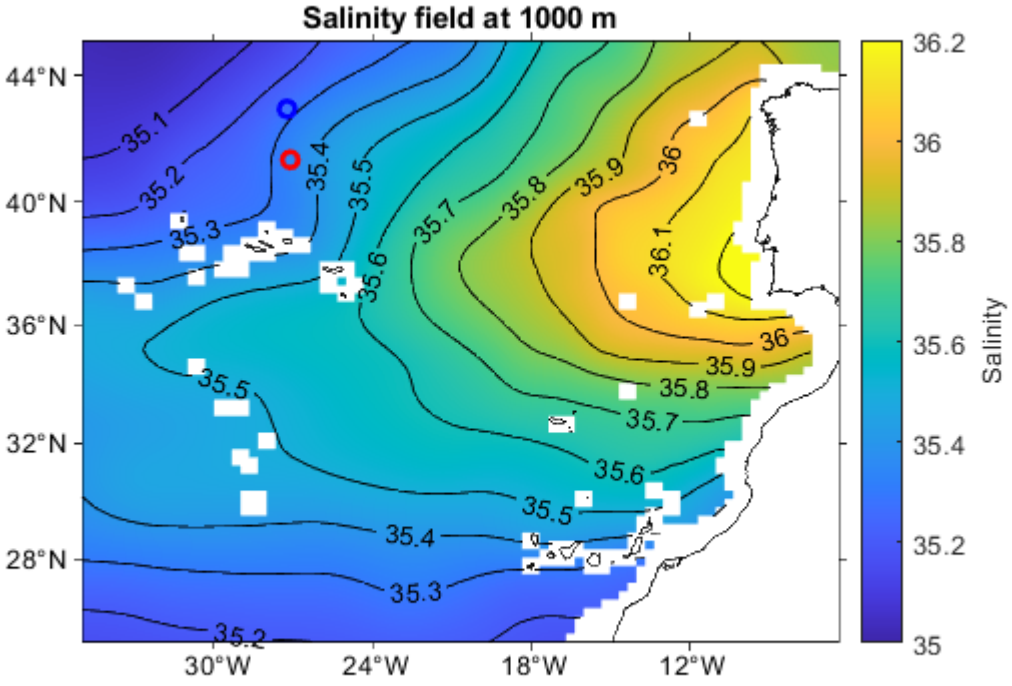

Appendix IV – MEDTRANS Practical Salinity (SP) fields for 700 m, 800 m, 900 m, 1000 m, 1100 m, 1200 m, 1300 m, and 1400 m depth. Dataset obtained from https://www.mare-centre.pt/en/research/data-library/medtrans-data (Bashmachnikov *et al*., 2015b). (cont.)

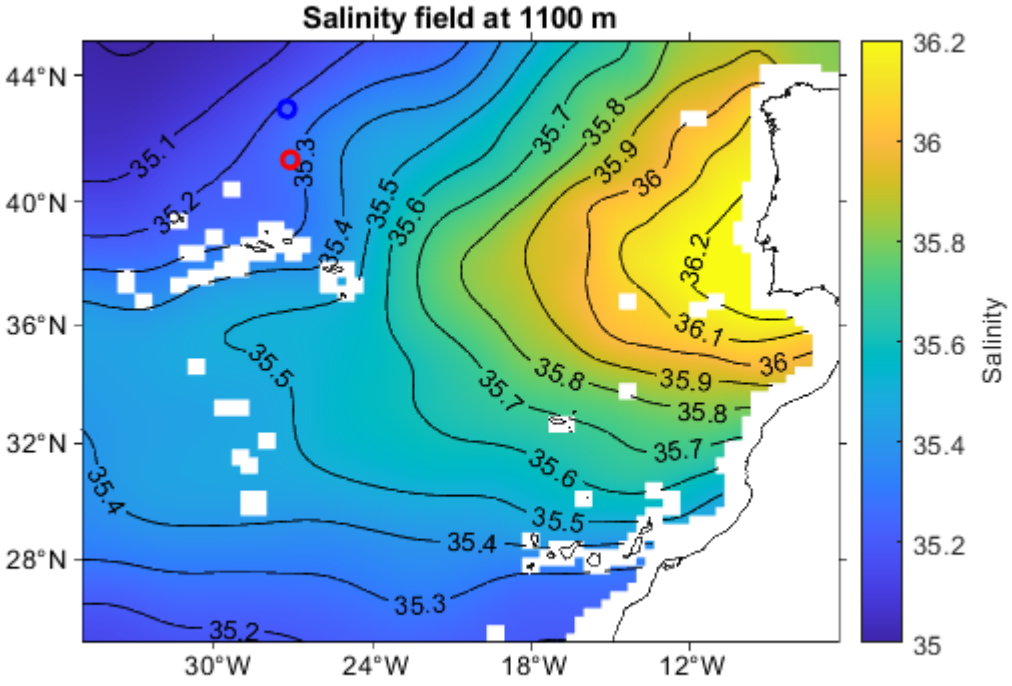

Appendix IV – MEDTRANS Practical Salinity (SP) fields for 700 m, 800 m, 900 m, 1000 m, 1100 m, 1200 m, 1300 m, and 1400 m depth. Dataset obtained from https://www.mare-centre.pt/en/research/data-library/medtrans-data (Bashmachnikov *et al*., 2015b). (cont.)

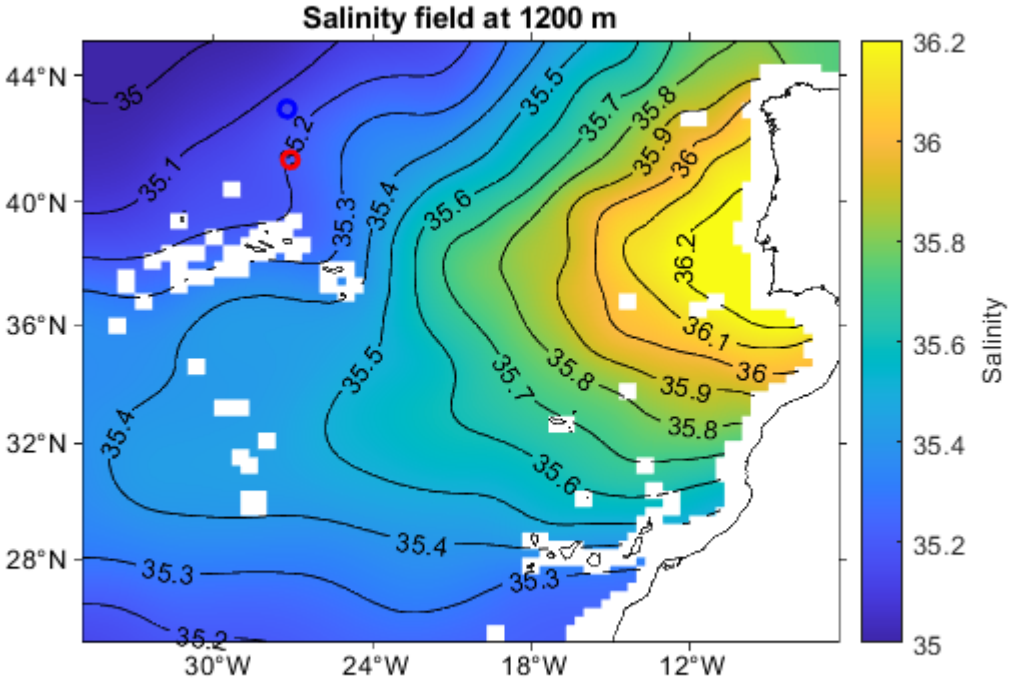

Appendix IV – MEDTRANS Practical Salinity (SP) fields for 700 m, 800 m, 900 m, 1000 m, 1100 m, 1200 m, 1300 m, and 1400 m depth. Dataset obtained from https://www.mare-centre.pt/en/research/data-library/medtrans-data (Bashmachnikov *et al*., 2015b). (cont.)

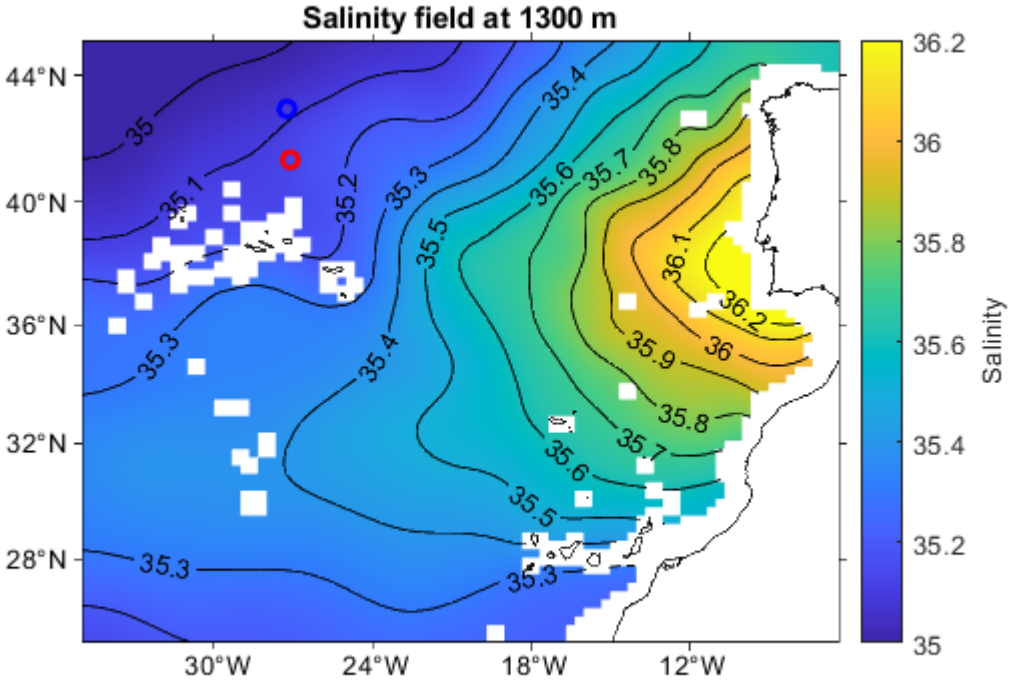

Appendix IV – MEDTRANS Practical Salinity (SP) fields for 700 m, 800 m, 900 m, 1000 m, 1100 m, 1200 m, 1300 m, and 1400 m depth. Dataset obtained from https://www.mare-centre.pt/en/research/data-library/medtrans-data (Bashmachnikov *et al*., 2015b). (cont.)

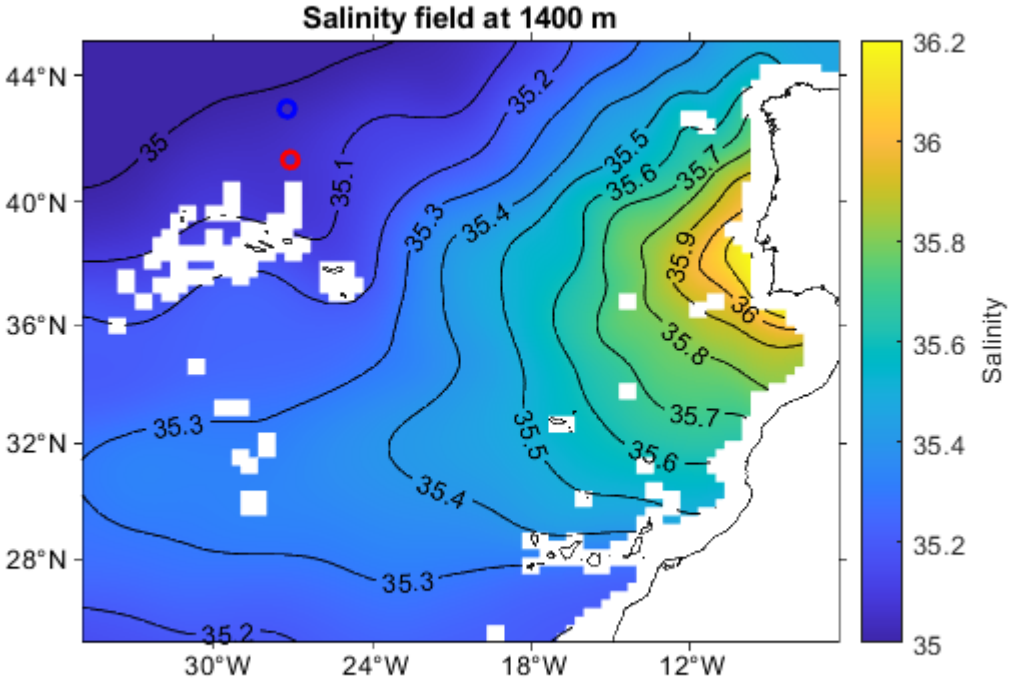

Appendix V – MEDTRANS temperature (º C) fields for 700 m, 800 m, 900 m, 1000 m, 1100 m, 1200 m, and 1300 m depth. Dataset obtained from https://www.mare-centre.pt/en/research/data-library/medtrans-data (Bashmachnikov *et al*., 2015b).

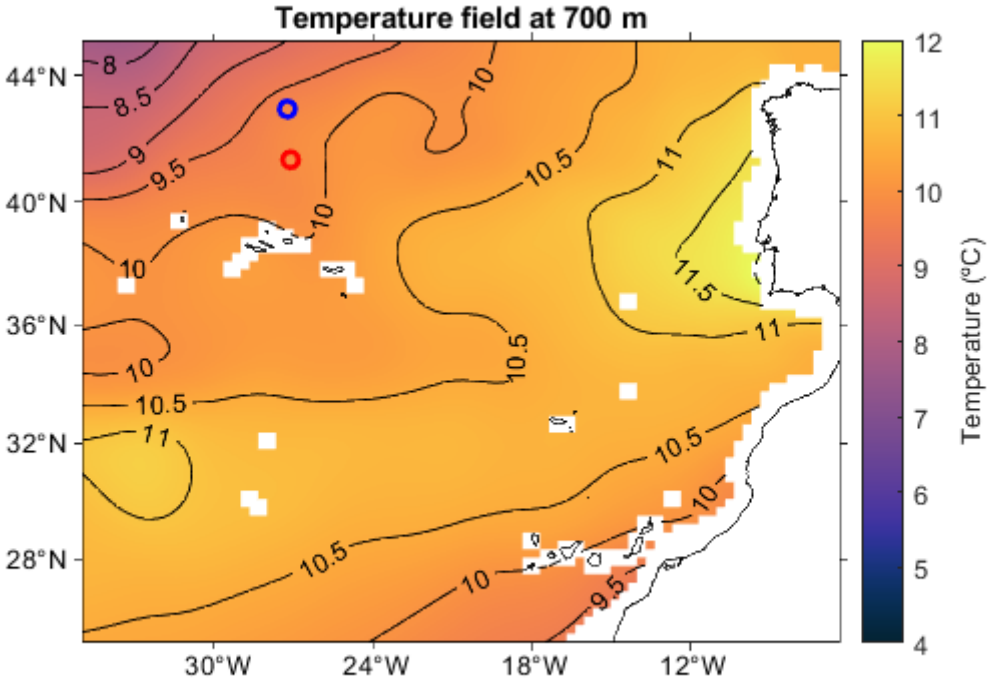

Appendix V – MEDTRANS temperature (º C) fields for 700 m, 800 m, 900 m, 1000 m, 1100 m, 1200 m, and 1300 m depth. Dataset obtained from https://www.mare-centre.pt/en/research/data-library/medtrans-data (Bashmachnikov *et al*., 2015b). (cont.)

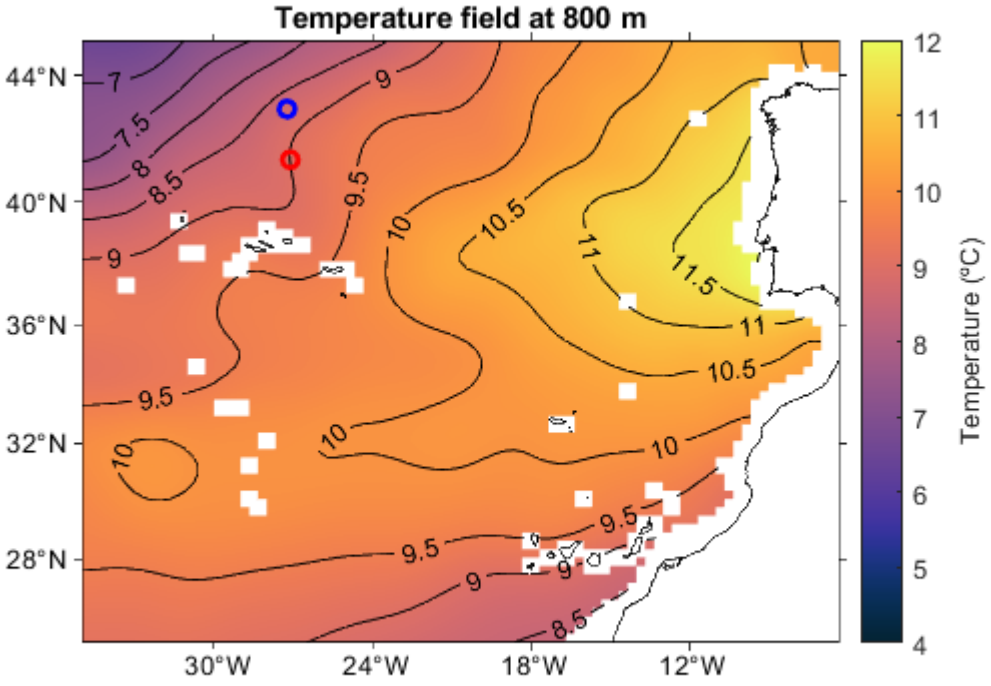

Appendix V – MEDTRANS temperature (º C) fields for 700 m, 800 m, 900 m, 1000 m, 1100 m, 1200 m, and 1300 m depth. Dataset obtained from https://www.mare-centre.pt/en/research/data-library/medtrans-data (Bashmachnikov *et al*., 2015b). (cont.)

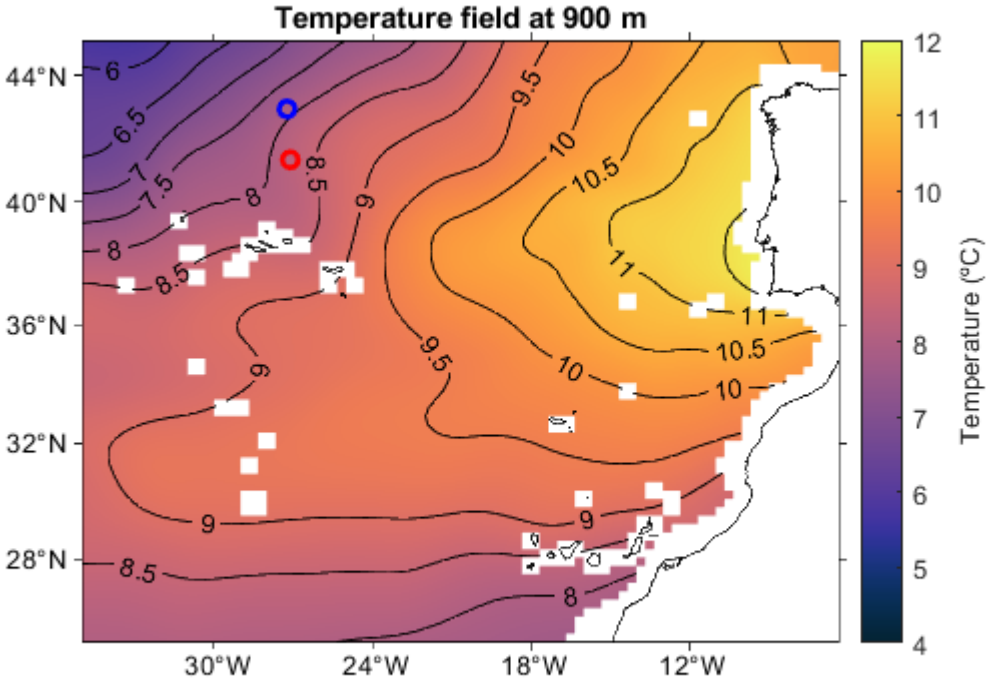

Appendix V – MEDTRANS temperature (º C) fields for 700 m, 800 m, 900 m, 1000 m, 1100 m, 1200 m, and 1300 m depth. Dataset obtained from https://www.mare-centre.pt/en/research/data-library/medtrans-data (Bashmachnikov *et al*., 2015b). (cont.)

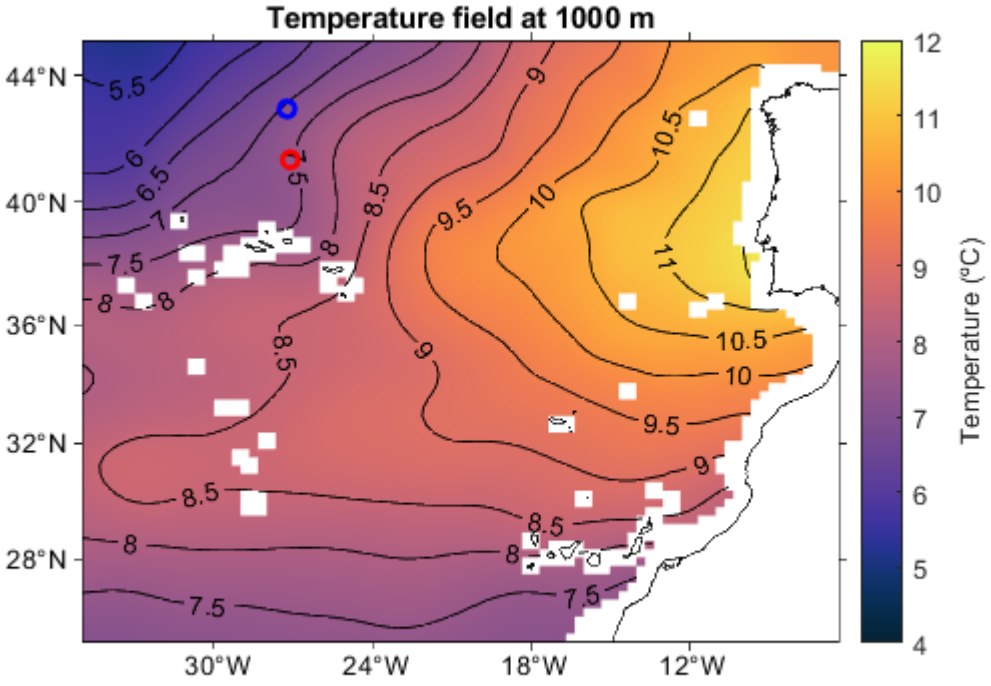

Appendix V – MEDTRANS temperature (º C) fields for 700 m, 800 m, 900 m, 1000 m, 1100 m, 1200 m, and 1300 m depth. Dataset obtained from https://www.mare-centre.pt/en/research/data-library/medtrans-data (Bashmachnikov *et al*., 2015b). (cont.)

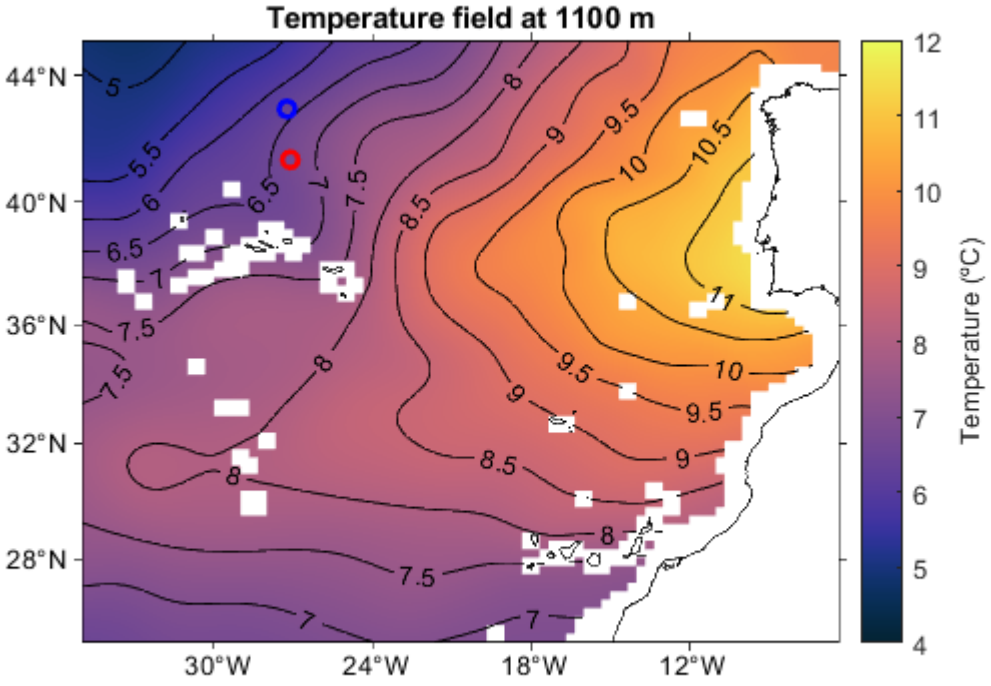

Appendix V – MEDTRANS temperature (º C) fields for 700 m, 800 m, 900 m, 1000 m, 1100 m, 1200 m, and 1300 m depth. Dataset obtained from https://www.mare-centre.pt/en/research/data-library/medtrans-data (Bashmachnikov *et al*., 2015b). (cont.)

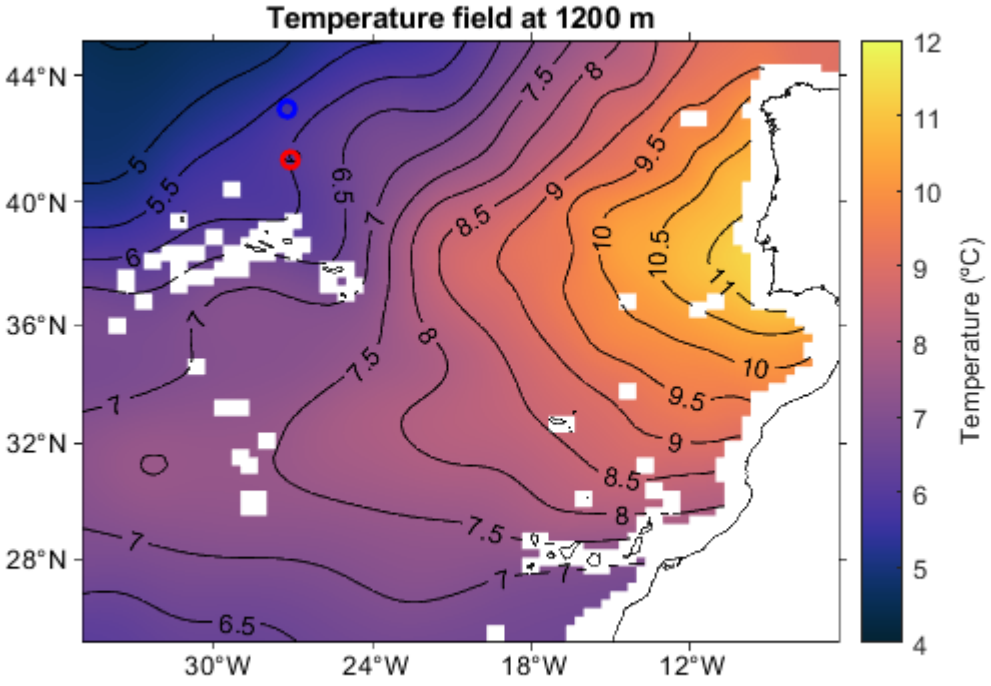

Appendix V – MEDTRANS temperature (º C) fields for 700 m, 800 m, 900 m, 1000 m, 1100 m, 1200 m, and 1300 m depth. Dataset obtained from https://www.mare-centre.pt/en/research/data-library/medtrans-data (Bashmachnikov *et al*., 2015b). (cont.)

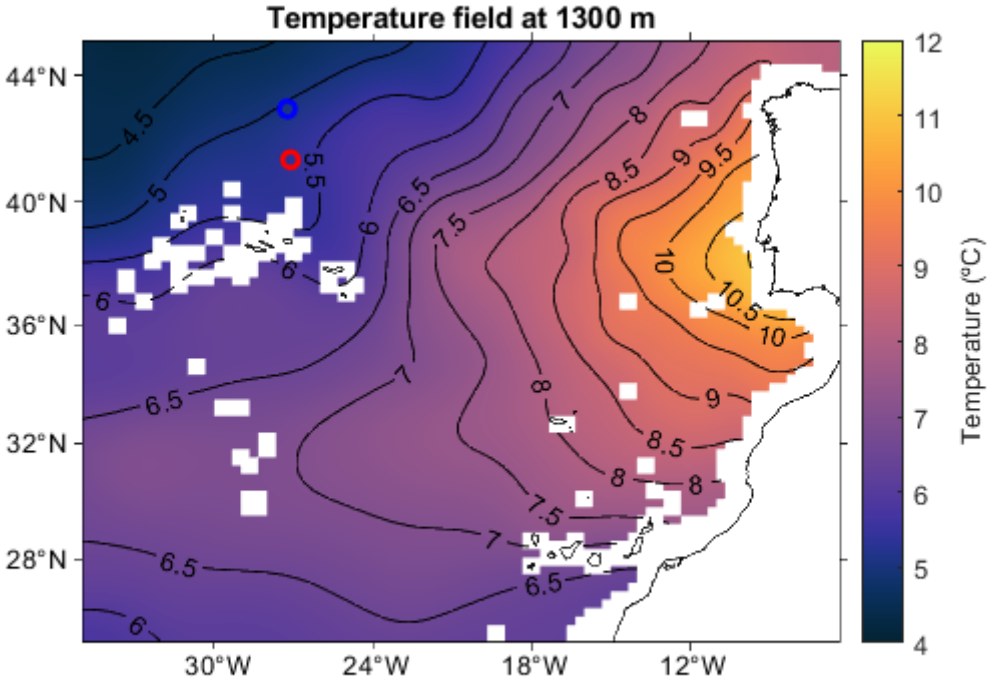

Appendix VI – Current velocity measurements obtained aboard the R/V Knorr (cruise KN207-03) from the hull-mounted ADCP along time. The "U" component is positive towards the East and negative towards the West and the "V" component is positive towards the North and negative towards the South.

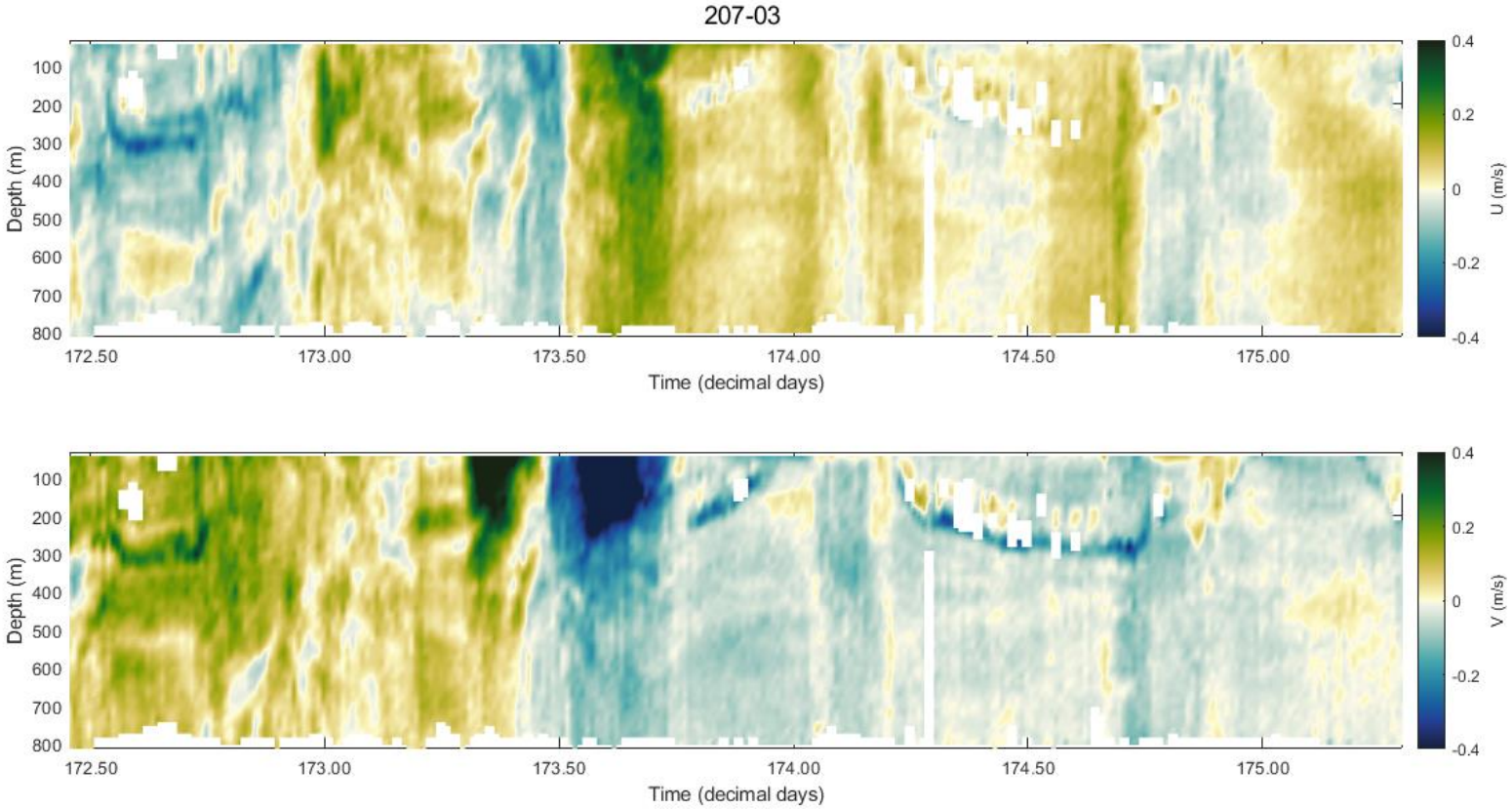

Appendix VI– Current velocity measurements obtained aboard the R/V Knorr (cruise KN207-03) from the hull-mounted ADCP along time. The "U" component is positive towards the East and negative towards the West and the "V" component is positive towards the North and negative towards the South. (cont.)

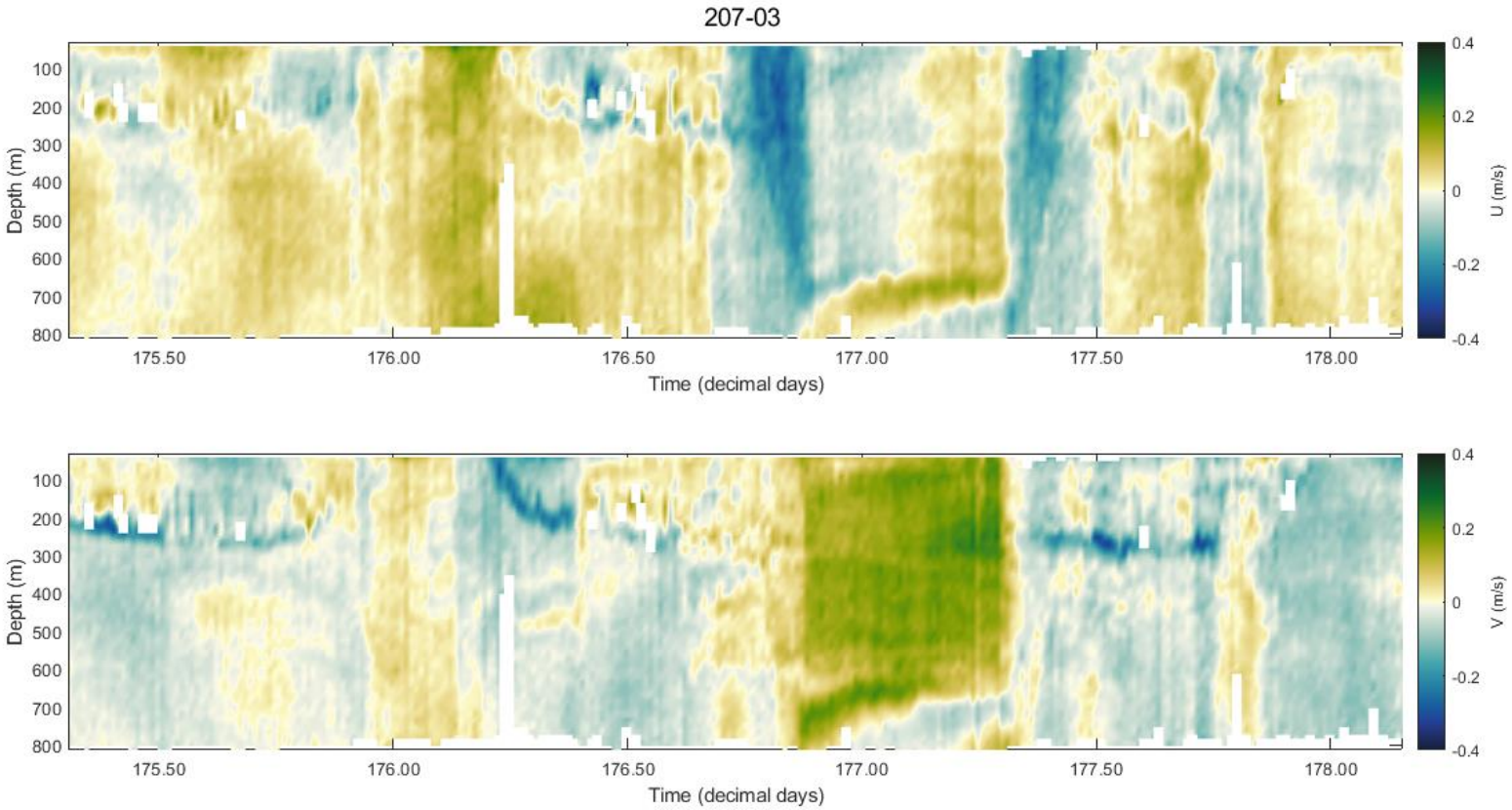

Appendix VI – Current velocity measurements obtained aboard the R/V Knorr (cruise KN207-03) from the hull-mounted ADCP along time. The "U" component is positive towards the East and negative towards the West and the "V" component is positive towards the North and negative towards the South. (cont.)

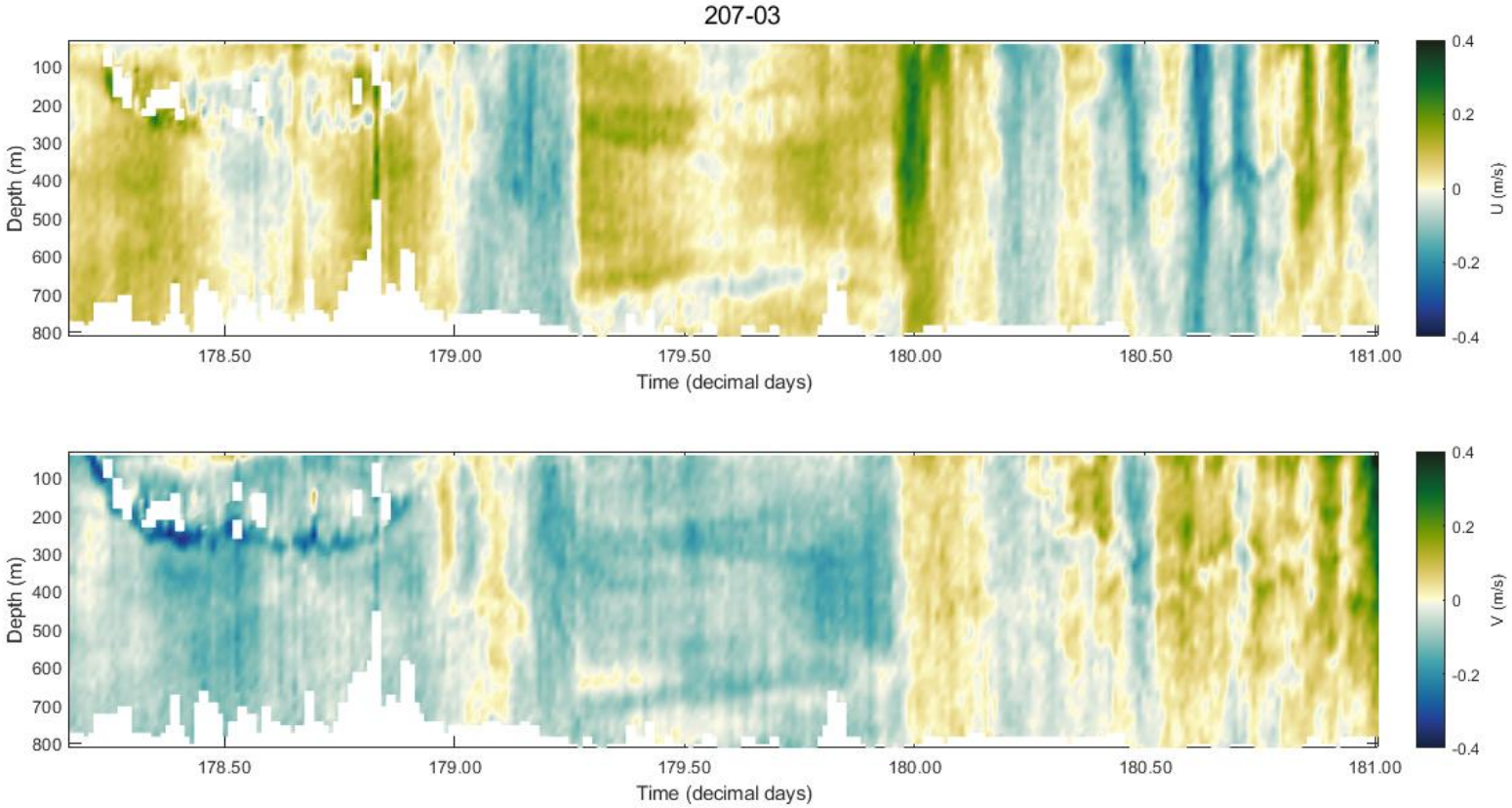

Appendix VI – Current velocity measurements obtained aboard the R/V Knorr (cruise KN207-03) from the hull-mounted ADCP along time. The "U" component is positive towards the East and negative towards the West and the "V" component is positive towards the North and negative towards the South. (cont.)

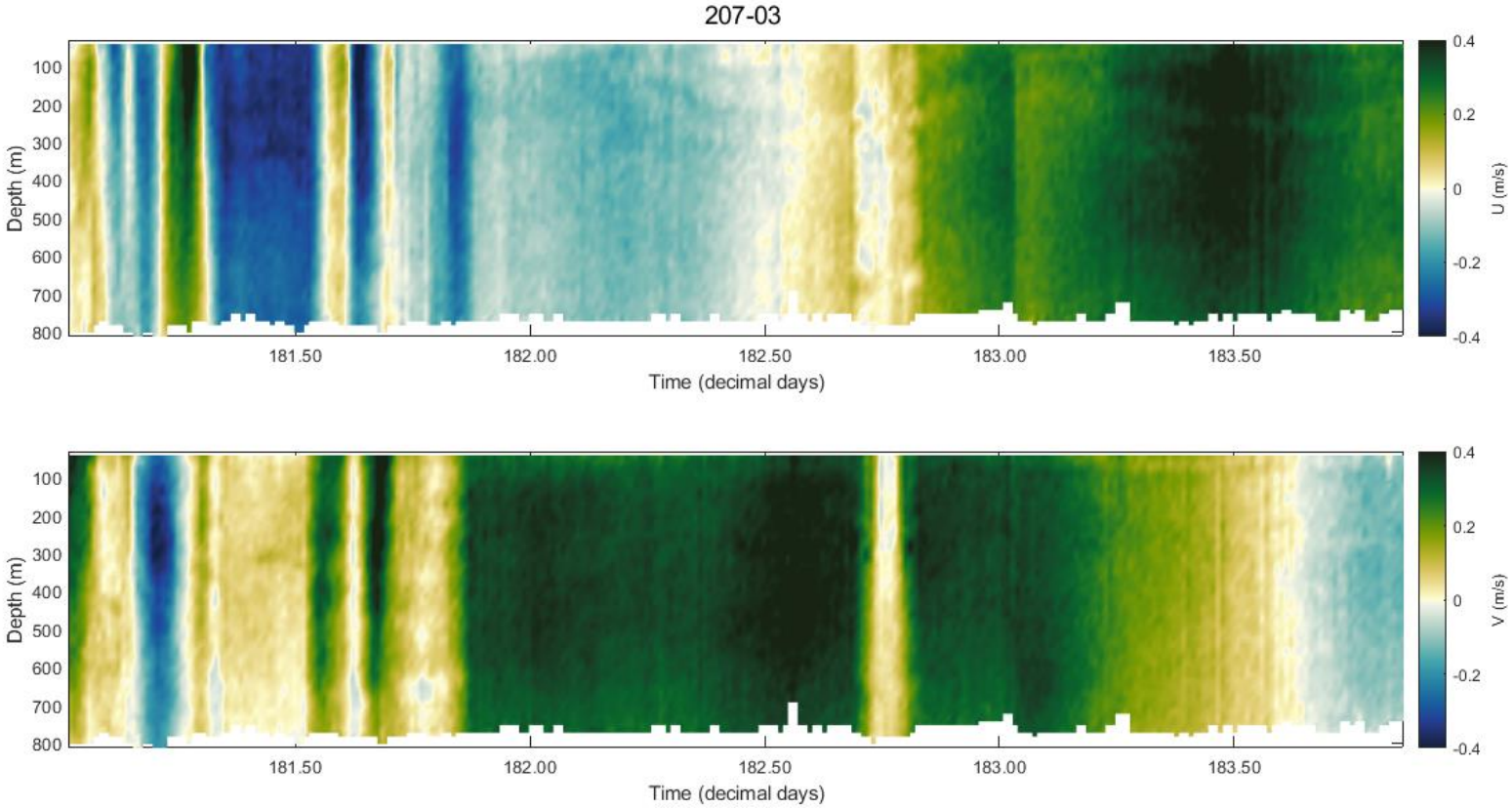

Appendix VI – Current velocity measurements obtained aboard the R/V Knorr (cruise KN207-03) from the hull-mounted ADCP along time. The "U" component is positive towards the East and negative towards the West and the "V" component is positive towards the North and negative towards the South. (cont.)

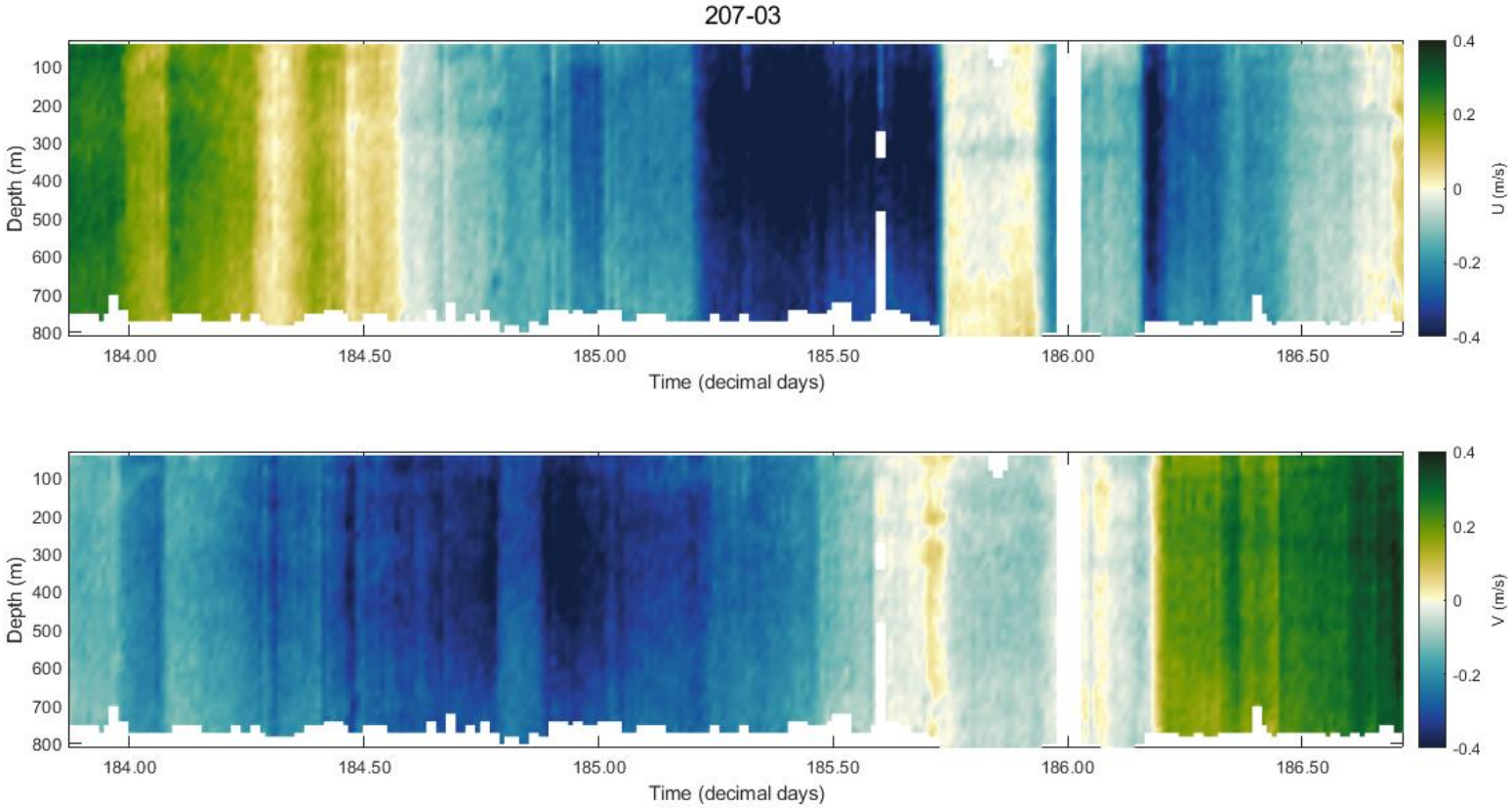

Appendix VI – Current velocity measurements obtained aboard the R/V Knorr (cruise KN207-03) from the hull-mounted ADCP along time. The "U" component is positive towards the East and negative towards the West and the "V" component is positive towards the North and negative towards the South. (cont.)

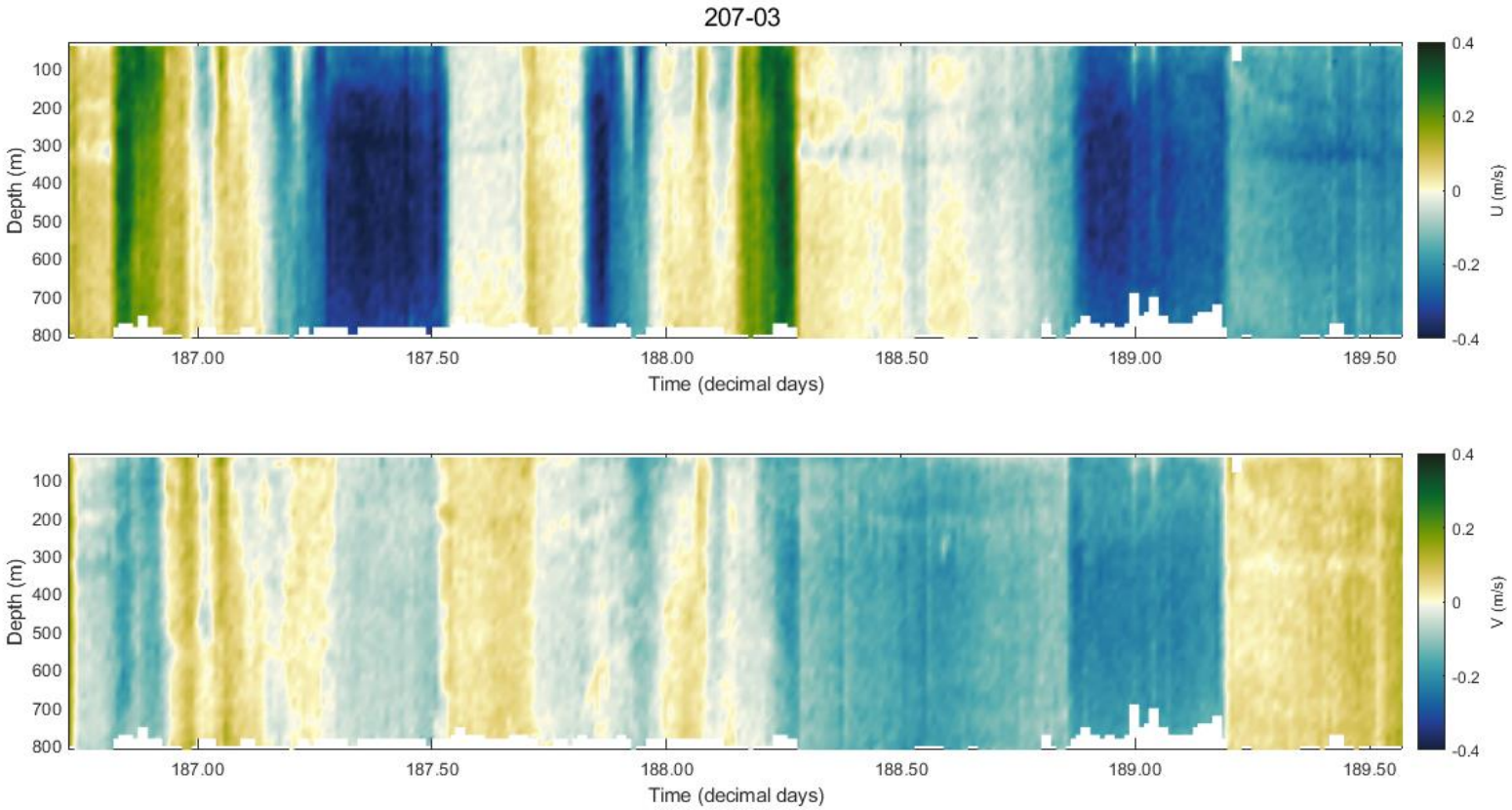

Appendix VI – Current velocity measurements obtained aboard the R/V Knorr (cruise KN207-03) from the hull-mounted ADCP along time. The "U" component is positive towards the East and negative towards the West and the "V" component is positive towards the North and negative towards the South. (cont.)

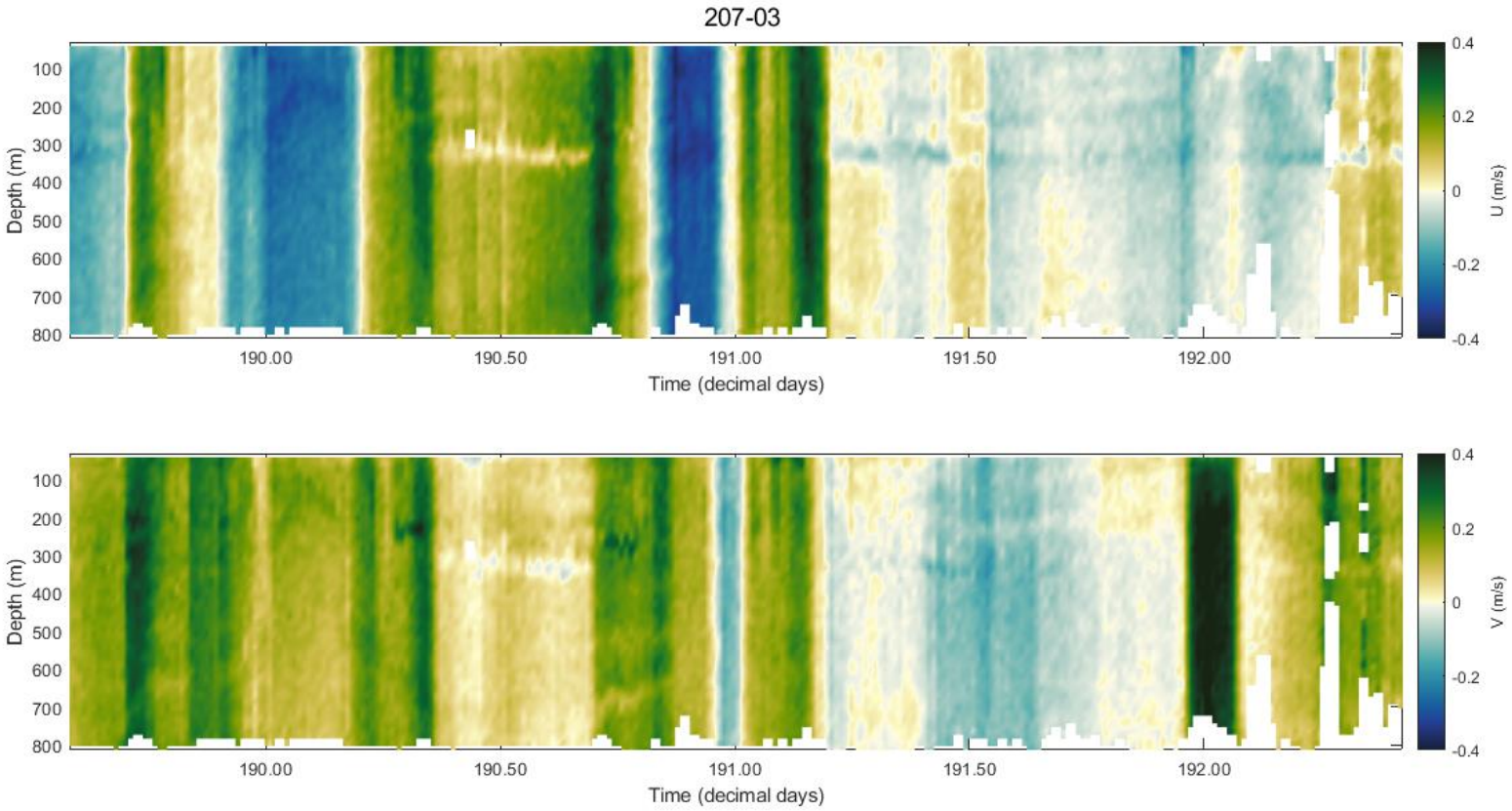

Appendix VI – Current velocity measurements obtained aboard the R/V Knorr (cruise KN207-03) from the hull-mounted ADCP along time. The "U" component is positive towards the East and negative towards the West and the "V" component is positive towards the North and negative towards the South. (cont.)

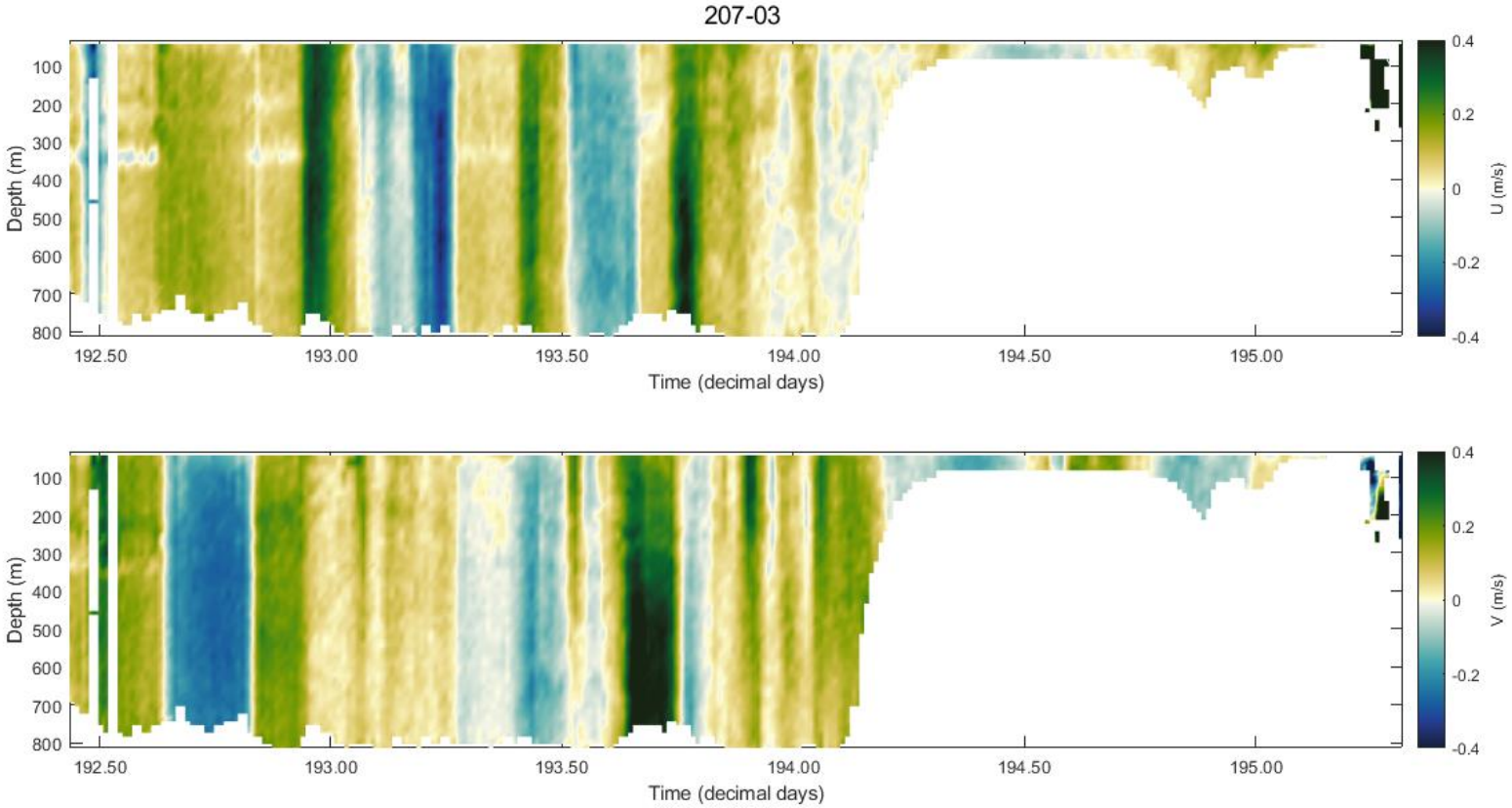

Appendix VI – Current velocity measurements obtained aboard the R/V Knorr (cruise KN207-03) from the hull-mounted ADCP along time. The "U" component is positive towards the East and negative towards the West and the "V" component is positive towards the North and negative towards the South. (cont.)